Equivalent Fluid Modelling of a Honeycomb Acoustic Liner using the Acoustic Porous Medium Formulation

Siddhant Khurana

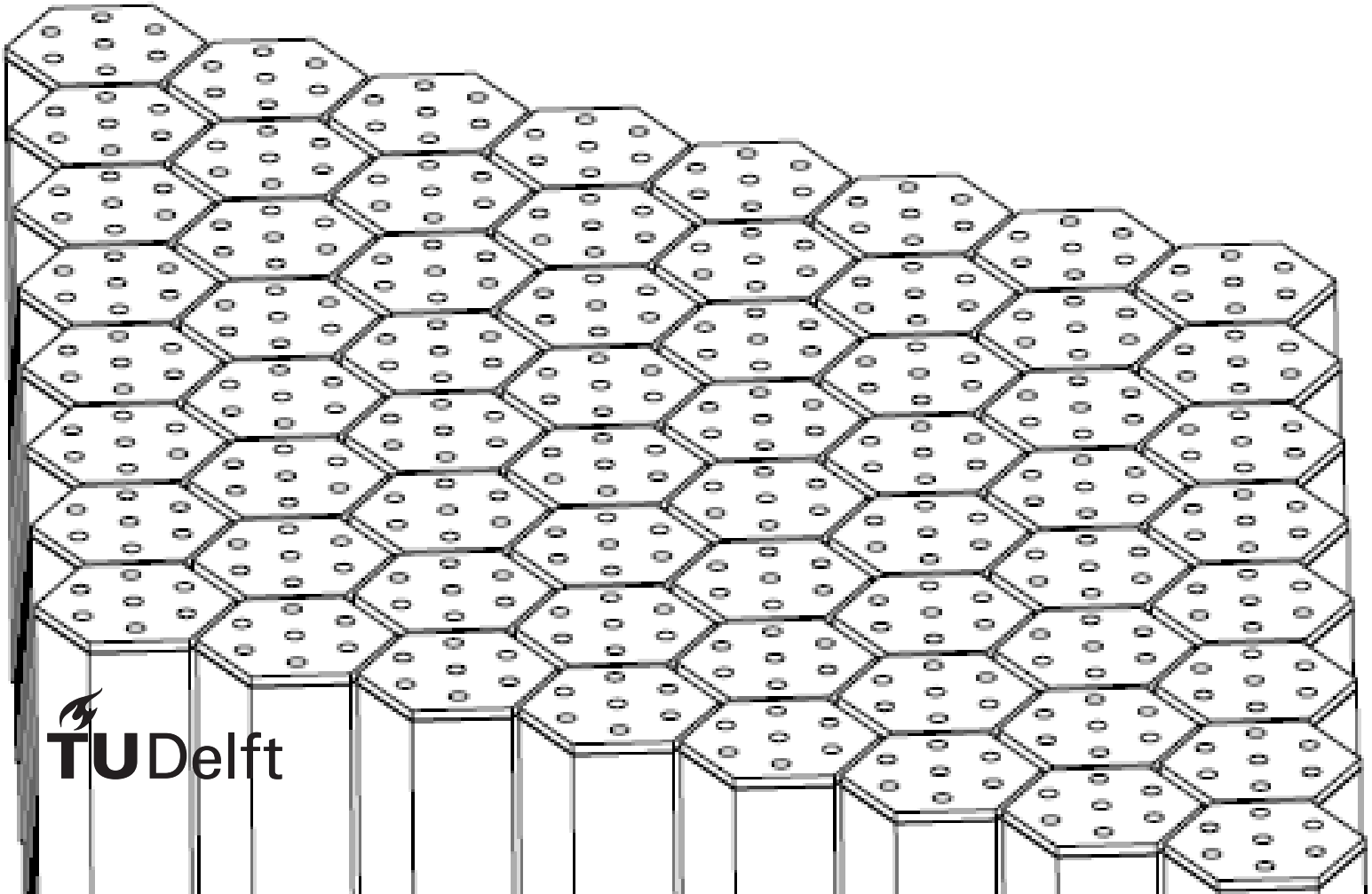

TU Delft

Equivalent Fluid Modelling of a Honeycomb Acoustic Liner using the Acoustic Porous Medium Formulation

by

Siddhant Khurana

to obtain the degree of Master of Science
at the Delft University of Technology,
to be defended publicly on Thursday October 8, 2020 at 09:30 AM.

Student number:	4693299	
Thesis committee:	Prof. dr. ir. D (Damiano). Casalino,	TU Delft, Chairperson
	Dr. F (Francesco). Avallone,	TU Delft, Supervisor
	Dr. M (Marios). Kotsonis,	TU Delft

Abstract

Acoustic liners are used extensively in aircraft engines, typically turbofan, to achieve relevant noise absorption. Over the past decades, numerous methods have been used to study acoustic liners through their impedance, of which numerical methods are of particular interest. Despite their advantages, numerical methods are bounded by certain drawbacks. One such drawback stems from the need to accurately discretize the liner geometry, which can lead to large simulation wall-clock time. Another limitation is caused by the absence of a stable and robust impedance boundary condition to account for the liner effects. With such limitations, there is a need to develop new methodologies which can effectively mimic the effects of an acoustic liner. A possible approach could be to model them as equivalent fluids. Thus, the primary objective of this project is to investigate the efficacy of the equivalent fluid approach to reproduce the liner effects. To satisfy this objective, the Acoustic Porous Medium (APM), which is an equivalent fluid formulation available in the flow-solver PowerFLOW® is employed in the current thesis.

The first part of the project focuses on verifying the use of the numerical setup with a honeycomb liner geometry and subsequently with an APM. Firstly, the honeycomb liner geometry is simulated and the results are analysed against experimental data and the theoretical models. This activity shows some discrepancies between the simulation and reference results. Through thorough diagnostic analysis, it has been found that these discrepancies are essentially caused because of the difference in the nature of input signals. While the reference results are computed with a tonal input, the current simulations are run with a broadband signal. It is shown that for the liner used in this study, flow non-linearities can exist for certain initial conditions, and thus, broadband and tonal signals cannot be used interchangeably. Next, from the simulations with the APM geometry the acoustic effects of the benchmark CT73 ceramic tubular liner are successfully reproduced, which verifies the use of the APM formulation. Now, the use of APM can be extended to mimic the effects of the reference honeycomb liner.

For reproducing the honeycomb liner effects with an APM, two different methodologies are explored. In the first approach, the APM model parameters are derived through an inverse algorithm present in PowerFLOW®. This algorithm uses a *priori* known impedance as an input and gives the corresponding model parameters as an output. In the second approach, the APM parameters are derived through the pressure drop values, measured across the liner facesheet under a steady laminar flow. With both these approaches, APM faces some limitations when compared with the reference impedance results. The shortcoming is primarily cause by the inability of the APM formulation to correctly account for the mass reactance effects of the reference liner. Moreover, the impedance results have also raised doubts over the use of the APM formulation for low input porosity values.

In the end, it is concluded that some improvements are required in the current implementation of APM to improve its efficacy for reproducing the acoustic effects of the honeycomb liner. This being said, APM in its' current implementation might still be able to model the acoustic effects of other honeycomb liners, however further investigation is required to ascertain this claim.

Preface

This thesis represents the last step of my journey as a TU Delft student. As I reach this milestone, I would like to use this page to thank a series of people who have supported me through my masters journey.

First of all, I would like to thank my thesis supervisor Francesco Avallone, not only for his guidance and patience, but also for his valuable feedback, even more importantly, for the trust he showed in me. Without your continuous support and motivation, I might not have been where I am today. I am also thankful to Prof.dr. Damiano Casalino for giving me the opportunity to work on this project. Working with you, especially during the end of the project, was an enriching and fun experience. I would also like to extend my sincere thanks to Alejandro Rubio Carpio and Christopher Teruna for helping me through the crucial stages of my project.

Secondly, I would also like to thank Jule Schranke, Jan Tukker, and Rink Hallmann from MARIN, for giving me the chance to work in a top engineering environment. Working in the basement, with lasers and waves is a memory I will always remember. Also my friends from the hen house - Kevin, Damadori, Lucas, Jean, Margot, Mariana, Katarina and Jarmo. You guys are wonderful individuals full of positivity.

Looking back, I am extremely thankful to my friends from Delft. Starting from the Eco-Runner Bad Boys Joel and Coertje. Thank you for all the amazing times over the past three years. My journey is definitely incomplete without the Delft library boys, Tomas, Umbi, Sven and Rober. Working all weekend, seeing all those books became a lot more fun with you guys. I must also thank my other friends from my masters. Prayash, Roger, Reinier and Sören thank you all for all the fun times in Rotterdam. My room mates, Seba and Matte - your care, support and coffee breaks kept me positive during stressful periods. And thank you my brothers back in India. Shanu Bhai, Morning, Gopan, Charas, Kunna, Deepak, Himalaya and Ritesh. You guys are my strength.

Finally and most importantly, I want to thank my family and especially my parents. I cannot express in words what your love and support means to me. Because of you I have had the best 25 years I could have hoped for. Thank you Bua, Micha, Max and Marc for always being there for me. Thank you dada and dadi. You have been a constant source of inspiration for me throughout my life. Lastly, thank you Papa and Mumma. It was your support and love that made this project successful.

Siddhant Khurana
Delft, October 2020

Contents

List of Figures

List of Tables

List of Acronyms

APM Acoustic Porous Medium.

CFD Computational Fluid Dynamics.

CHE Convected Helmholtz Equation.

DDOF Double Degree of Freedom.

DNIT Digital Normal Impedance Tube.

DNS Direct Numerical Simulation.

EHR Extended Helmholtz Resonator.

FEV Fine Equivalent Voxels.

GIT Grazing Impedance Tube.

IBC Impedance Boundary Condition.

IMBC Ingard-Meyers Boundary Condition.

LB Lattice Boltzmann.

LBM Lattice Boltzmann Method.

LES Large Eddy Simulation.

LNSE Linearized Navier Stokes Equation.

MSD Mass Spring Damper.

NIT Normal Impedance Tube.

NS Navier Stokes.

OASPL Overall Sound Pressure Level.

ROI Region of Interest.

SDOF Single Degree of Freedom.

SEM Scanning Electron Microscope.

SPL Sound Pressure Level.

TMM Two Microphone Method.

VLES Very Large Eddy Simulation.

I

Background

1

Introduction

For several years now, people have been protesting against the high level of noise associated with the ever growing aircraft operations. This is primarily motivated by the annoyance and irritation caused by the aircraft-related noise [53]. Thus, aviation governing bodies such as the European Aviation Safety Agency (EASA) have imposed stringent regulations for aircraft noise reduction [1]. In addition to this, aircraft companies have to also comply with the noise regulations of individual airports, which in many cases might be more rigorous. For example, in the London Heathrow airport, the aircrafts have to abide with their score-system for low noise requirements [41]. In such case, it is likely that the commercial operations of aircraft companies are threatened by strict noise regulations.

Figure 1.1: Aircraft engine nacelle installed with acoustic liners (in black) [2]

In the current scenario, the aircraft engine remains the biggest source of aircraft-related noise. This noise can be associated with the engine-core, where the combustion process takes place, or with the engine-nacelle which houses the compressor blades [33]. Traditionally, the engine-related noise is damped by using acoustic liners, which are installed at the inner walls of the aircraft engine [5]. Figure 1.1 shows the acoustic liners installed on an engine nacelle. Prompted by the ever increasing demands of the noise regulations, recent research has been focused on developing improved liner designs. Over the past decades, numerous methods have been used to study acoustic liners, of which numerical methods are of particular interest. Despite its advantages, the extent of use of numerical methods is limited, as its application is computationally expensive [73]. Another limitation stems from the absence of a stable and robust impedance boundary condition to account for the effects of an acoustic liner [9]. This has motivated the current research to investigate a new innovative method to mimic the acoustic effects of these liners.

The current introduction presents some of the basic concepts which are essential to understand the work done in the current thesis. Finally, the motivation behind the current project is given followed by the structure of the thesis report.

1.1. Acoustic Liners of Interest

The most commonly used acoustic liner, as far the aero-engine related application is concerned, is the Single Degree of Freedom (SDOF) liner such as that shown in figure 1.2(a). It consists of a perforated facesheet backed by a cavity and a solid backplate. In such liners, the major source of sound attenuation is the dissipation that occurs at the orifice of the facesheets [27], while the backing cavity essentially decides the frequency at which maximum acoustic attenuation will occur [45]. For most aircraft applications, the cross sectional shape of the cavity is that of a honeycomb, and thus the SDOF liners are also referred to as honeycomb liners. The SDOF/ honeycomb liners are usually preferred when absorption is required over a narrow-band frequency range [32]. A variant of the SDOF liner is the Double Degree of Freedom (DDOF) liner as shown in figure 1.2(b). Unlike the SDOF liners, DDOF liners have two sets of cavity, that are usually divided using a porous mesh or a perforated facesheet. With the presence of two cavities, DDOF liners are able to provide maximum sound attenuation at two different frequencies [44]. Porous Medium Liners such as the metallic foam shown in figure 1.3 are another type of acoustic liners. These liners are designed to provide acoustic absorption over a broadband range of frequency. However, their use especially in aircraft-related applications is limited due to manufacturing and durability concerns. Moreover, they continue to be heavier and expensive than the SDOF liners which has thwarted its widespread use. It should be noted that for the purpose of this thesis, the honeycomb liners are of particular interest.

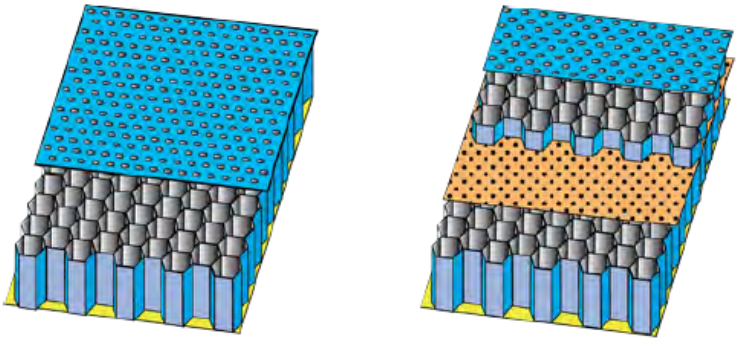

(a) SDOF Liner (b) DDOF Liner

Figure 1.2: Single Degree (SDOF) and Double Degree (DDOF) of Freedom Honeycomb Liners [32]

Figure 1.3: Metallic Foam Liner [51]

1.2. Locally Reacting and Extended Reacting Assumptions

Depending on their structure, acoustic liners can be classified as locally reacting or extended/ non-locally reacting. One of the most common version of locally reacting structure are the cavity-backed perforated facesheets such as that shown in figure 1.4. Such liners usually provide spatially concentrated acoustic absorption, mainly at the location of the liner orifice. Consequently, most locally reacting

liners are efficient absorbers over a narrow frequency bandwidth. The assumption of being locally reacting implies that the interaction of the liner with the sound wave occurs only in the normal direction. Thus, the flow physics within the domain of a single cavity is independent of the neighbouring cavities as there is no acoustic interaction parallel to the liner facesheet. Although the efficacy of this assumption is a topic of widespread research, it is justified for multiple liner applications.

Conversely, extended-reacting liners usually consist of a porous medium without any impervious partitions. Without any partitions, such liners are able to provide spatially distributed resistance to the incoming sound waves. Extended-reacting liners have proved to be an ideal choice for delivering sound absorption over a broadband frequency range. The porous material shown in figure 1.3 can be considered as an extended reacting liner.

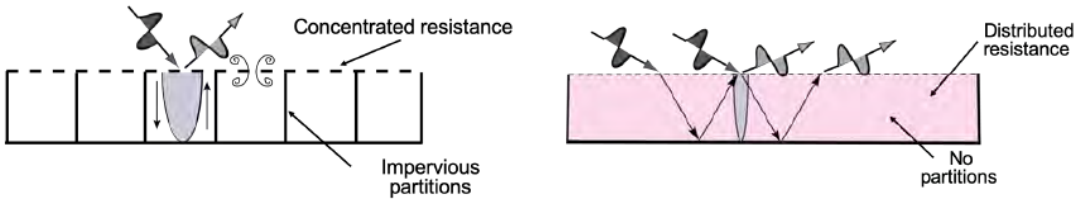

(a) Locally-Reacting Liners (b) Extended-Reacting Liners

Figure 1.4: Liners based on their structure [32]

1.3. Acoustic Impedance

Locally reacting acoustic liners are characterised through a macroscopic quantity called the acoustic impedance. Acoustic impedance (Z) is defined as the ratio of the complex acoustic pressure ($\hat{p}$) and the complex acoustic velocity ($\hat{v}$) normal to the surface S. In most acoustic applications, impedance (Z) is normalised with the characteristic impedance of air i.e., ρc_∞ and is represented as,

$$\frac{Z}{\rho c_\infty} = \frac{\hat{p}}{\rho c_\infty (\hat{v} \cdot n_s)} = R + \iota\chi \tag{1.1}$$

where ρ density while c_∞ represents the speed of sound. The above equation shows that the acoustic impedance is a complex variable, i.e. it is defined in the frequency domain. The real part R represents the acoustic resistance while the imaginary part χ is the acoustic reactance. Physically speaking, the acoustic resistance is related to the absorption mechanisms such as the viscous losses at the orifice walls [63], the vortex shedding from the edge of the orifices [27] etc, while the reactance is related to the inertia of the medium. The acoustic reactance is essentially composed of two components, namely i) the reactance due to the backing cavity and that due to ii) the mass-inertia associated with the liner orifice [45]. Acoustic impedance (Z) is an intrinsic property of the liner, which implies that it should be independent of the installation geometry [32]. Thus, impedance derived in a controlled environment, such as in the Kundt's tube, can be directly used to study the sound absorption performance of liners installed in nacelles of aircraft engine. This is indeed an advantage of using impedance for characterising acoustic liners. Thus, the current research in the field of acoustic liners is focused on the eduction of the acoustic impedance.

1.4. Problem Statement

It is clear from the discussion presented above that acoustic impedance is an important parameter to assess the performance of honeycomb liners. Impedance can be educed either through theoretical methods, through experimental methods, or by employing computational methods based on either the Navier-Stokes (NS) equations or the Lattice Boltzmann (LB) equations. However, each of these methods is bounded by certain drawbacks. For example,

- A common challenge for the theoretical methods is to accurately account for the non-linear flow phenomenons [62], such as shedding of vortices from the edge of liner orifice. Moreover, per-

formance of these models relies largely on the availability of empirical data, which is not always known as a *priori*.

- Experimental methods often have cumbersome installation requirements which limits its use to simple installation geometries [19].
- The effort to accurately discretize the liner geometry in numerical simulations can lead to large wall-clock times which is major limitation of this method [43]. Moreover, the use of an impedance boundary condition with numerical simulations is bounded by instability issues [9].

The limitation associated with the impedance eduction methods mentioned above, with the numerical methods in particular, reflects on the need to develop alternative methodologies to educe liner impedance. A possible yet comparatively unexplored approach is to model honeycomb liners as equivalent fluid regions. Equivalent fluid regions can be directly coupled with numerical schemes such as LBM to generate the same absorption characteristics as an acoustic liner. Although some research has been been done to model porous materials as equivalent fluid regions [65], hardly any work has been done to do the same for honeycomb liners. Thus, this thesis aims to implement and validate the use of the equivalent fluid approach to model the effects of a honeycomb acoustic liner. The equivalent fluid model used in the current study is based on the Acoustic Porous Medium (APM) formulation available in the Lattice-Boltzmann based flow-solver, PowerFLOW®.

1.5. Thesis Outline

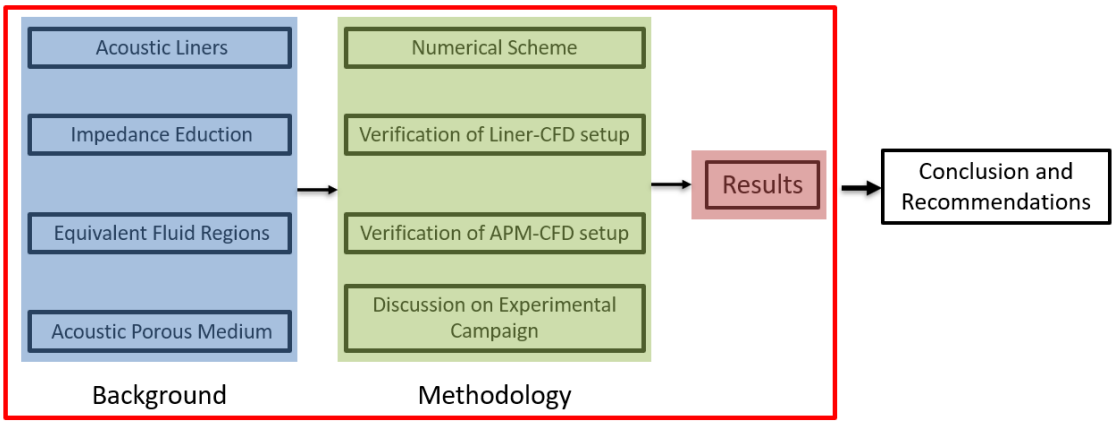

Figure 1.5: Schematic showcasing the report structure

This report is essentially divided in four parts. In Part I of the current thesis, necessary background knowledge which is required to achieve the research objective is presented. This introductory chapter along with chapter 2 and chapter 3 are included in part I. In chapter 2 essential background information on honeycomb liners is provided along with a brief review of the existing impedance eduction methods. This chapter should establish the motivation behind the need to explore alternate methodologies for educing liner impedance. Chapter 3 introduces the concept of equivalent fluid regions and attempts to justify the use of the APM model to mimic the acoustic effects of the honeycomb liner.

In part II, an elaborate discussion is presented on the methodology employed in the current thesis. This part includes information on the numerical scheme employed within PowerFLOW® in chapter 4, followed by a verification study of the honeycomb liner and APM-CFD setups in chapter 5 and chapter 6 respectively. Chapter 7 presents the procedure to derive the APM model parameters from a pressure drop experiment.

Next, in part III the important results from the APM simulations are given. Finally, the knowledge gained from the aforementioned parts is used to conclude the thesis and give recommendations for the future work in part IV.

2

Acoustic Liners

Acoustic Liners are one of the most commonly used techniques for achieving relevant noise absorption. They find applications in variegated fields ranging from an aircraft engine to the walls in a room [20]. Liners can be of various types, but for the current thesis, the conventional cavity-backed perforated facesheets are of particular interest. Thus, in the current chapter, the working of the liner is introduced through a physical description of a Helmholtz resonator in section 2.1. Following this, various impedance prediction methods, ranging from theoretical to numerical methods, are discussed in section 2.2, with a meticulous discussion of the associated limitations. Familiarisation with the drawbacks of the existing impedance eduction methods will justify the need to look towards alternate methods, such as the equivalent fluid modeling.

2.1. The Helmholtz Resonator

Commonly used acoustic liners, especially those used in aircraft-engine related applications, consists of a perforated facesheet backed with a cavity and a solid back-plate, making the liners Helmholtz-resonator type [72]. Helmholtz resonators are resonance-type absorbers, which means that the maximum sound absorption is driven by the resonance frequency of the Helmholtz resonator. A typical Helmholtz resonator consists of a closed volume (V), which interacts with the external medium through a cavity/ neck opening as shown in figure 2.1. The resonators' neck represents the perforated facesheet of an acoustic liner, while the backing cavity enclosed by the solid back-plate is represented by the closed volume V. In figure 2.1, a and A are the radius of the neck and cavity respectively. S ad L represent cross sectional area and length, while subscript n and b are used for neck and body respectively.

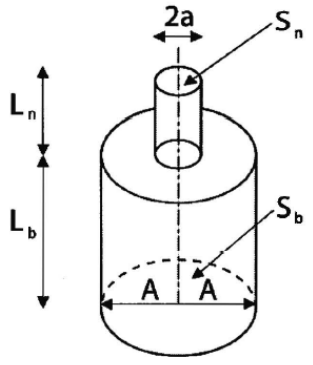

Figure 2.1: Helmholtz Resonator [20]

Under the action of an external acoustic excitation, the mass of air enclosed inside the resonator neck is driven into the solid volume (V), thus compressing the air inside the volume and consequently, increasing the pressure. When the pressure inside the volume becomes greater than the incoming pressure

from the acoustic wave, the mass of air in the neck is pushed back to its original position. Under the assumption that no new external force is applied to the system, the air-mass in the neck will oscillate due to the ”springiness” of the air trapped inside the volume V. These oscillations and subsequently the acoustic energy attenuates due to thermal and viscous dissipation at the walls of the resonators' neck, of which viscous dissipation is of particular interest. Viscous dissipation is a result of the no-slip boundary condition at the resonators wall, which induces a viscous boundary layer.

Quantitatively speaking, a more intuitive description of the sound attenuation process can be given by characterising the Helmholtz resonator using the lumped-element analysis. This method is valid under the assumption that the wavelength of the incident acoustic wave is large compared to the characteristic dimensions of the resonator. Under this assumption, the Helmholtz resonator is analogous to a mass-spring-damper (MSD) system. A fixed base MSD configuration with the spring and damper in parallel are shown in figure 2.2.

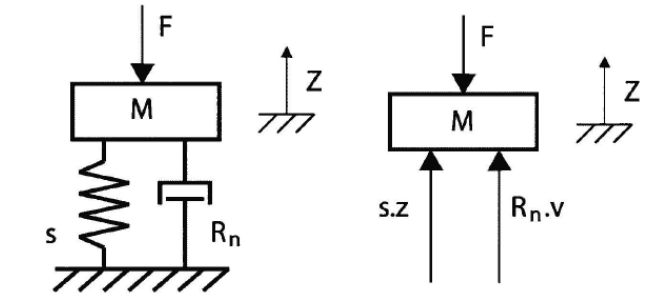

(a) Mass Spring Damper (MSD) System (b) Free body diagram of MSD

Figure 2.2: Lumped Analogy of a single Helmholtz resonator [20]

The mass (M) shown in figure 2.2 represents the mass of the air inside the cavity neck, and is thus defined by the volume of the neck and the density of the fluid (in this case air):

$$M = S_n \rho L_n \tag{2.1}$$

As explained earlier, the ”springiness” of the air enclosed in the volume V causes the mass of air in the neck to oscillate. This ”springiness” is defined by the spring constant (s), which is derived using the Hooke's law as [39],

$$s = \frac{\rho c_\infty^2 S_n^2}{V} \tag{2.2}$$

where c_∞ is the speed of sound. The viscous dissipation, on the other hand, is accounted by the damper in the MSD system (see figure 2.2(a)). The expression for this dissipation is given by Ingard [27] as,

$$R_n = \frac{L_n}{a}\frac{\sqrt{2\mu\rho\omega}}{\pi a^2} + 2\frac{\sqrt{2\mu\rho\omega}}{\pi a^2} \tag{2.3}$$

where μ is the dynamic viscosity and ω is the angular frequency. The first right hand term in equation 2.3 represents the viscous losses in the walls of the neck, while the second right hand term accounts for the viscous losses at the ends of the neck [27]. Furthermore, the resonance frequency (ω_0) of a Helmholtz resonator is derived using the natural frequency of a MSD system, i.e. $\omega_0 = \sqrt{s/M_n}$ [58]. The maximum attenuation of acoustic energy is achieved at the resonance frequency which is defined as,

$$\omega_0^2 = \frac{S_n c_\infty^2}{V L_n} \tag{2.4}$$

In the lumped-element representation, the contribution of the mass, spring and damper to the dissipation of acoustic energy can be represented by a single macroscopic quantity, called the acoustic impedance (Z). Impedance (Z) under the locally reacting assumption (section 1.2), can be defined as the ratio of complex acoustic pressure ($\hat{p}$) and complex acoustic velocity ($\hat{v}$) normal to the surface S.

$$Z = \frac{\hat{p}}{\hat{v} \cdot n_s} \tag{2.5}$$

Finally, the acoustic impedance of a Helmholtz resonator can be derived by substituting the external force F (derived using the force balance in figure 2.2(b)) in the equation 2.5.

$$Z = \frac{\iota\omega M + R_n + \frac{\iota s}{\omega}}{S_n} = R + \iota\chi \tag{2.6}$$

where R_n is a measure of resistive forces that dissipates the acoustic energy. Equation 2.6 shows that the acoustic impedance is indeed a complex valued function. The real part (R) is the resistance term, while the imaginary part (χ) is the reactance term. The complete derivation of the impedance given in the above equation can be found in Appendix A.

The discussion presented above gives a quantitative understanding of sound attenuation by an acoustic liner, without diving into complex flow dynamics. It is important to note that the lumped-element analogy presented above assumes a linear framework i.e. no grazing flow and a particle displacement smaller than the characteristic dimensions of the resonator [58]. However, it is well established that sound intensities upto a level of practical interest often lead to a non-linear liner behaviour (such as shedding of secondary vortices from the liner orifice) [63]. This implies that the liners under most actual installation conditions cannot be represented by the impedance derived in equation 2.6. Thus, the prediction of liner impedance is rather complex and is discussed in detail in the next section.

2.2. Characterisation of Acoustic Liners

The discussion presented in previous sections establishes that the acoustic liners are characterised through their impedance (Z). The total acoustic impedance of a liner can be defined as the sum of several effects, i.e. the viscous impedance (Z_V), backing impedance (Z_B), radiation impedance (Z_R) and the non linear effects (Z_{NL}). The viscous impedance (Z_V) is the result of viscous dissipation of acoustic energy at the walls of the liner orifice, while the radiation impedance (Z_R) is caused by the mass-inertia and the distortion of the acoustic flow at the surface of the perforated facesheet. The backing impedance (Z_B), on the other hand, represents the contribution of the backing cavity and the non-linear effects (Z_{NL}) usually occur under grazing flow conditions, under high sound pressure level (SPL) and at the resonance frequency of the acoustic liner.

$$Z = Z_V + Z_B + Z_R + Z_{NL} \tag{2.7}$$

The current section, summarizes some of the most important theoretical, experimental, and numerical methods that are commonly used for characterising acoustic liners.

2.2.1. Prediction of Liner Impedance using Analytical & Semi-Empirical Methods

All analytical approaches seek to model the effects mentioned in equation 2.7 based on physically inspired modeling assumptions. Early analytical studies for predicting impedance, such as that given by Sivian [63], assumes a mass of fluid confined in the orifice. This fluid oscillates under the action of an external acoustic excitation on one side and cavity pressure on the other side. Sivian [63] used a simple viscous model at the orifice walls along with orifice end corrections to represent the viscous dissipation and the radiation effects respectively. A common challenge for such theoretical models has been to accurately account for the flow non-linearities which are usually dominant under grazing flow and high SPL input. Analytical attempts to determine non-linear impedance, close to the liner resonance frequency without grazing flow, has been made by Singh & Rienstra [62]. They performed an asymptotic analysis on a single Helmholtz resonator that provided higher order corrections for the pressure inside the liner cavity, to account for the non-linear effects near the resonance frequency. Rienstra & Singh [59] have also presented a higher fidelity version of their previous model [62]. They attributed the improved fidelity to the use of a numerically superior asymptotic expression for the pressure inside the liner cavity. With this analysis, they extended the use of their model to predict non-linear behaviour at higher SPL values.

For all semi-empirical methods, the usual procedure is to derive the viscous effects Z_V, backing impedance Z_B and radiation effects Z_R analytically and model the non-linear effects (Z_{NL}) based on experimental

results. Melling [45] derived a semi-empirical model to predict acoustic impedance in both linear and non-linear regime for an acoustically excited flow. He based the linear viscous dissipation on Crandall's theory of linear impedance [17] and included the end corrections based on the work of Ingard [27]. The impedance of the perforated facesheet as derived by Melling [45] is given as,

$$\frac{Z_{perforate}}{\rho c_\infty} = \frac{i\omega}{c_\infty \phi C_D}\left[\frac{t_f}{F\,(k_s' r)} + \frac{8 d_o \Psi(\zeta)}{3\pi F\,(k_s r)}\right] + \frac{1.2}{2c_\infty}\frac{1-\phi^2}{(\phi C_D)^2} v_{rms} \tag{2.8}$$

where d_o represents the orifice diameter, ρ is the density, ϕ is the porosity of the facesheet, t_f is the facesheet thickness, c_∞ is the speed of sound, C_D is the orifice discharge coefficient, v_{rms} is the rms of the acoustic velocity at the centre of the orifice and k_s and k_s' are the Stokes wave number defined by,

$$k_s = \sqrt{-\frac{i\omega}{\nu}} \quad \text{and} \quad k_s' = \sqrt{-\frac{i\omega}{\nu'}} \tag{2.9}$$

where ν' is the effective kinematic viscosity which takes into account the losses due to thermal conductivity, such that ν' = 2.179·ν. Furthermore, the acoustic interactions between neighbouring orifices are included using the Fok function $\Psi(\zeta)$ which is given by,

$$\Psi(\zeta) = \sum_{n=0}^{n=8} a_n \zeta^n \tag{2.10}$$

a_n are empirically derived constants given as, a_1 = -1.4092, a_2 = 0, a_3 = 0.33818, a_4 = 0, a_5 = 0.06793, a_6 = -0.02287, a_7 = 0.03015, a_8 = -0.01641 and $\zeta = \sqrt{\phi}$.

$$F\,(k_s' r) = 1 - \left[\frac{2J_1\,(k_s' r)}{k_s' r J_0\,(k_s' r)}\right] \tag{2.11}$$

where J_0 and J_1 are the Bessel function of the first kind. It should be noted that equation 2.8 gives only the impedance of the perforated facesheet. The reactance associated with the cavity depth is included by the term shown below,

$$\chi_{cavity} = -\rho c_\infty cot(k \cdot L) \tag{2.12}$$

Thus, the final impedance of a cavity backed perforated liner is given by,

$$\frac{Z_{perforate}}{\rho c_\infty} = \frac{i\omega}{c_\infty \phi C_D}\left[\underbrace{\frac{t_f}{F\,(k_s' r)}}_{\text{Linear}} + \underbrace{\frac{8 d_o \Psi(\zeta)}{3\pi F\,(k_s r)}}_{\text{Inertial}}\right] + \underbrace{\frac{1.2}{2c_\infty}\frac{1-\phi^2}{(\phi C_D)^2} v_{rms}}_{\text{Non-Linear}} + \underbrace{\iota\chi_{cavity}}_{\text{Cavity-Depth}} \tag{2.13}$$

In equation 2.13, the first and the second term represents the linear and inertial effects, i.e the viscous dissipation and mass-inertia respectively. The third term represents the non-linear resistance which essentially depends on the fluctuating acoustic velocity in the orifice (v_{rms}). This velocity can be derived either through experimental results or through numerical simulations. The last term on the right hand side gives the effect of the cavity depth. Moreover, the orifice discharge coefficient C_D, represents the contraction of the flow as it enters the liner orifice. The contraction sets up a minimum flow area, called the *vena contracta*, where the streamlines are parallel to each other. This area is smaller than the orifice cross-section and thus, signifies the acceleration of the flow as it enters the liner-orifice.

Another commonly used semi-empirical model is given by Motsinger & Kraft [46]. Unlike the model given by Melling [45], the use of this model can be extended to grazing flow conditions. In this model, the resistive part of the impedance is given by,

$$\frac{R}{\rho c_\infty} = \underbrace{\frac{32\mu t_f}{c_\infty \phi C_D d_o^2}}_{\text{viscous}} + \underbrace{\frac{|u_o|}{2\phi^2 c_\infty C_D^2}}_{\text{grazing flow + high SPL}} \tag{2.14}$$

where μ represents the dynamic viscosity and the term u_o includes empirical correction to account for the grazing flow. Spillere et al. [64] have been critical of using the expression of viscous resistance in equation 2.14. They state that the expression is valid only when $|k_s d/2| < 1$, which is not valid for most practical liner operating conditions. Here d represents the liner orifice diameter. The reactance of the liner, on the other hand, is influenced by the cavity depth and the mass reactance. The mass reactance further includes viscous components and component due to the radiation effects at the surface of the facesheet. Thus, the reactance term becomes,

$$\frac{\chi}{\rho c_\infty} = \underbrace{\frac{\omega t_f}{\phi c_\infty}}_{\text{viscous}} + \underbrace{\frac{\omega \epsilon}{\phi c_\infty}}_{\text{radiation}} - \underbrace{\cot(k \cdot L)}_{\text{cavity depth}} \tag{2.15}$$

where ϵ is the correction length which accounts for the radiation effect at the liner orifice and is given as $\epsilon = 0.85(1 - 0.7\sqrt{\phi})$. The combination of equation 2.14 and equation 2.15 gives the impedance (Z) as shown in equation 2.16.

$$\frac{Z}{\rho c_\infty} = \frac{R}{\rho c_\infty} + \iota \frac{X}{\rho c_\infty} \tag{2.16}$$

The models of Melling [45] and Motsinger [46] are important for the current thesis as they are used in the verification study presented in chapter 5.A challenge faced by the semi-empirical models presented above is the accurate prediction of the discharge coefficient C_D. The discharge coefficient is used to model the change in momentum flux through the orifice-wall boundary layer. Motsinger et al. [46], based on experimental data, suggested an average discharge coefficient ($\bar{C_D}$) of 0.76 for an acoustically excited orifice. This average value for C_D can be used when an analytical formulation is not possible (due to non-linearities). However, Zhang and Bodony [74] have shown that C_D is not constant but rather dependent on the phase of the incident acoustic excitation. For an acoustically excited flow, Zhang and Bodony [74] decided to model the orifice boundary layer profile ($V(r)$) rather than directly modeling C_D. The expression to model $V(r)$ is given as,

$$V(r) = \frac{1}{\tanh(a/\delta^*)} \tanh\left(\frac{a - r}{\delta^*}\right) \tag{2.17}$$

where r is the orifice radius and δ^* is the in-orifice boundary layer thickness which was obtained using the direct numerical simulation (DNS) data. The discharge coefficient C_D can be deduced from the expression of $V(r)$ given in equation 2.17.

However, unlike for the acoustically excited case discussed above, Zhang and Bodony [73] were unable to find a fully theoretical model for the in-orifice boundary layer under grazing flow conditions. This was attributed to the flow complexities introduced by the grazing flow, such as the blocking of the acoustic wave by the grazing flow boundary layer. Thus, Zhang and Bodony [73] modeled the discharge coefficient (C_D) separately for the inflow and outflow cycle based on a power law relation as shown in equation 2.18 and equation 2.19 respectively. Here the inflow and outflow cycle signifies the oscillatory motion of the acoustic wave through the liner orifice.

$$C_{D_i} = \beta_1 \tanh\left[\alpha_1 \left(\frac{v_i}{U_\infty}\right)^{\gamma_1}\right] \tag{2.18}$$

$$C_{D_o} = \beta_2 \tanh\left[\alpha_2 \left(\frac{v_o}{U_\infty}\right)^{\gamma_2}\right] \tag{2.19}$$

where v_i and v_o are the inflow and outflow velocity at the orifice centre respectively. The constants β_1, β_2, α_1 and α_2 are obtained using the least square fitting of the DNS data.

This section summarizes few of the most relevant analytical and semi-empirical models for the current study. From this discussion it can be concluded that the accurate prediction of non-linear effects is a bottleneck for the theoretical models. It is clear that although non-linear effects can be accounted by using empirical inputs, the success of the theoretical models is highly sensitive to the availability of quality experimental data.

2.2.2. Prediction of Liner Impedance using Experimental Methods

The current section presents a brief introduction of different experimental methods used for characterising acoustic liners at various levels of precision.

One of the more basic methods to characterise a liner is to evaluate the ”DC” flow resistance of the liner facesheet [32]. Here, the name ”DC” stems from the fact that the facesheet is analysed under a steady laminar flow, as opposed to the oscillatory motion of an acoustic wave. A common setup to measure the DC flow resistance is shown in figure 2.3. The test sample, which is the liner facesheet, is kept under a laminar flow input, and the pressure drop is measured using the static pressure probes on either side of the facesheet. The DC flow resistance, R_f, is then given as,

$$R_f = \frac{\Delta P_s}{U} \tag{2.20}$$

where P_S represents the static pressure and U is the velocity of the laminar flow. Normalising the resistance obtained in equation 2.20 with the characteristic impedance of air ($\rho_\infty c_\infty$) gives a good approximation of the acoustic resistance [32]. It has been shown that the current representation holds reasonably well for acoustic wavelength much larger than the facesheet thickness, i.e. $\lambda \gg t_f$, and for frequencies away from the resonance and anti-resonance frequency of the liner [29]. However, the fact that the effect of frequency, input sound pressure level (SPL), and the input source type (tonal or broadband) on the liner impedance (Z) cannot be evaluated by the current method, is one of its clear disadvantages. Anyways, this method is used in the current thesis to obtain the DC flow resistance and consequently the APM model parameters corresponding to the reference liner (see chapter 5) in chapter 7.

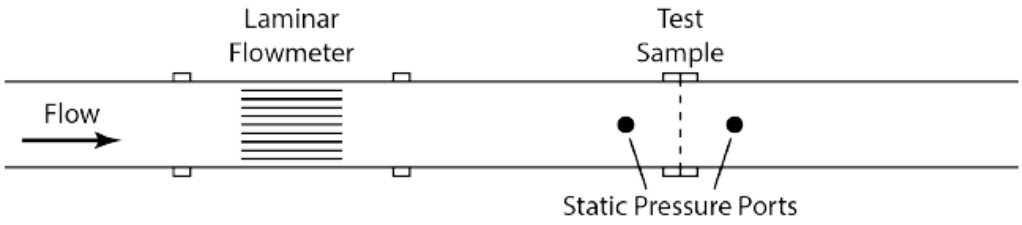

Figure 2.3: Pressure drop measurement setup [32]

An extensively used method to determine liner impedance under an acoustic input is the *in situ* technique such as that formulated by Dean [19]. Dean [19] formulated a two-microphone impedance eduction method for locally reacting acoustic liners. This method involves capturing the absolute value of the acoustic pressures at two different microphone locations; one at the liner facesheet (P_{fs}) and the other at the cavity backplate (P_{bp}) as shown in figure 2.4(a). The impedance with this method can be then computed as,

$$Z = \frac{P_{fs}}{\rho_\infty c_\infty u_{fs}} = \frac{-ie^{i\phi}}{\sin(kh)} \frac{P_{fs}}{P_{bp}} \tag{2.21}$$

where ϕ is the phase difference between the pressure at the liner facesheet and that at the cavity backplate, k is the wavenumber and h represents the depth of the liner. The two microphone method can give accurate impedance predictions under no flow conditions. When grazed by mean flow, the accuracy of this method is limited as the assumption of locally reacting liner maybe violated [72]. Dean [19] also pointed out two limitations of the method, i) the microphone situated at the liner surface should be outside the hydrodynamic influence so only the acoustic disturbances are captured; however, ii) if the distance of the mic from liner surface is comparable to the boundary layer thickness then the impedance prediction would be incorrect. Anyways, this method is widely used for impedance eduction not only in experiments but also in numerical simulations ([74],[73], [43]).

In situ methods such as that explained above are intrusive and thus require cumbersome installation.

An alternative to the *in situ* method is to acquire the desired readings at a distance away from the liner surface. One such method is the two microphone method (TMM) developed by Jones & Stiede [36]. The acoustic pressure is measured by the flush-mounted microphones on the wall of the impedance tube as shown in figure 2.4(b). This method assumes that only plane wave exists inside the wave guide, which means that the wavefronts are planes perpendicular to the direction of propagation of the wave. Thus, the complex acoustic pressure can be given by,

$$\hat{p_j} = \left[p_i e^{-ikx_j} + p_r e^{ikx_j}\right] e^{i\omega t} \tag{2.22}$$

where p_i and p_r are the acoustic pressure of the incident and reflected waves at the microphone location j respectively. In equation 2.22 the only unknowns are p_i and p_r. With pressure readings at two microphone locations, the above problem becomes deterministic in nature. In such a case, the impedance (Z) is given as,

$$Z = \frac{1 + R_e}{1 - R_e} \tag{2.23}$$

where R_e is the reflection coefficient and is given as $R_e = p_r/p_i$. Although, this method provides easier installation as compared to the *in situ* methods, it introduces other issues. For frequencies where the half-wavelength, and subsequently the acoustic node, is close to distance between the two microphones, the results are subjected to uncertainties. This is because near the nodes, the microphone would sense small amplitudes of the same order of magnitude as that of the experimental error [34]. Moreover, the TMM measures a weighted average of the acoustic pressure over the entire liner surface. This averaging might cause a slight loss of accuracy [32]. Nevertheless, TMM method remains a popular choice for educing acoustic impedance especially for liners under normal acoustic excitation [32].

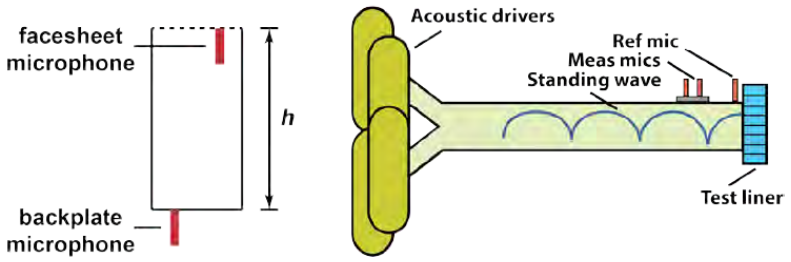

(a) Dean's Setup (b) Two Microphone Method Setup

Figure 2.4: Common impedance eduction setups under no-flow conditions [32]

The addition of grazing flow along with the acoustic wave increases the complexity to educe acoustic impedance. Commonly used method to educe acoustic impedance, when the liner is grazed by a uniform flow, combines the microphone measurements with a duct propagation code, such as those based on Convected Helmholtz Equation (CHE) [37]. In this method, the acoustic field inside the waveduct (shown in figure 2.5) satisfies the CHE which is given by,

$$\left(1 - M^2\right)\frac{\partial^2 p(x,y)}{\partial x^2} + \frac{\partial^2 p(x,y)}{\partial y^2} - 2ikM\frac{\partial p(x,y)}{\partial x} + k^2 p(x,y) = 0 \tag{2.24}$$

where M denotes the Mach number of the input grazing flow. The liner surface is represented by an impedance boundary, which uses the Ingard-Myers boundary condition (see equation 2.26). Equation 2.24 and equation 2.26 are coupled with a cost minimisation problem (equation 2.25) to search for the impedance (Z) which would generate the same pressure field as that recorded by the microphones.

$$F(Z) = \sum_{j=1}^{N_{mic}} \left\| p\left(x_j, 0\right)_{CHE} - p\left(x_j, 0\right)_{meas} \right\| \tag{2.25}$$

where N_{mic} represents the number of microphones at the bottom wall of the waveguide, $p(x_j, 0)_{CHE}$ is the pressure calculated through CHE, and $p(x_j, 0)_{meas}$ is the pressured measured by the microphones.

In other methods, the duct propagation code is based on Linearised Euler Equation (LEE) [71], however, the basic principle of solving for minimising the error remains the same.

A limitation of educing impedance through experimental methods, under grazing flow conditions, has been identified by Renou and Aurégan [54]. This stems from their observation of differences in the impedance spectra, when the direction of the grazing flow relative to that of an acoustic wave is changed. This phenomenon violates the locally reacting assumption for an acoustic liner, according to which the impedance should be independent of the structure of the flow field above the liner [72]. Watson et al. [70] have suggested that this discrepancy indicates the need to include the shear flow effects, which are not considered with the Ingard-Myers boundary condition (discussed in section 2.2.3). Currently, the efficacy of the Ingard-Myers boundary condition to educe liner impedance under grazing flow remains a contentious topic in liner research [15]. Moreover, under grazing flow conditions, some authors such as Dai & Aurégan [18] have even questioned the locally reacting definition of acoustic impedance (see equation 1.1).

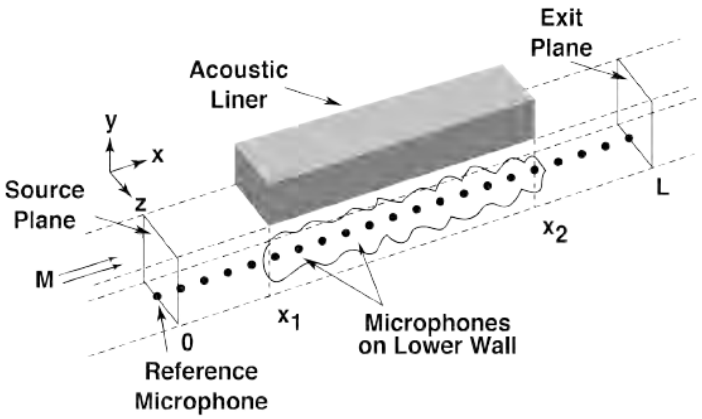

Figure 2.5: Grazing Impedance Tube Setup at NASA Langley [32]

2.2.3. Prediction of Liner Impedance using Numerical Methods

From the discussion presented in the previous sections, it is clear that eduction of acoustic impedance, especially in the non-linear regime, is a rather complicated process. The limitations associated with non-linear flows stems from a limited physical understanding of the near and in-orifice flowfield. With the recent advances in the computational aeroacousitc methods, numerical schemes such as DNS and LBM have become useful tools which can be used to mimic the effects of acoustic liners and therefore, improve our understanding of the flowfield in the vicinity of the liners. The discussion in this section is given in two parts. In the first part, the results from numerical simulations conducted with the actual liner geometry is presented, followed by a discussion on the use of the Impedance Boundary Condition (IBC) with the numerical schemes in the second part.

Numerical Simulations with Liner Geometry

One of the first impedance study, through numerical means, was conducted by Tam & Kurbatskii [67] who studied slit liners (figure 2.6(a)) under a normal acoustic excitation for a wide range of frequencies and incident sound pressure levels, using DNS. Tam & Kurbatskii [67] observed vortex shedding from the slit at the resonance frequency of the slit liner ($\approx$ 1 kHz), which is in accordance with the work of Ingard et al. [27]. They attributed the dissipation of acoustic energy to the viscous dissipation at the walls of the slit and to the vortex shedding. The comparison of experimental and numerical results at an input SPL of 130 dB is shown in figure 2.6(b). It is seen that the numerical results show a reasonable match with the experimental ones except at a frequency of 2 kHz. Tam & Kurbatskii [67] suggested a possible vortex shedding at f = 2 kHz which is not captured by their numerical simulations might cause this discrepancy. However, this suggestion could not be confirmed in their study.

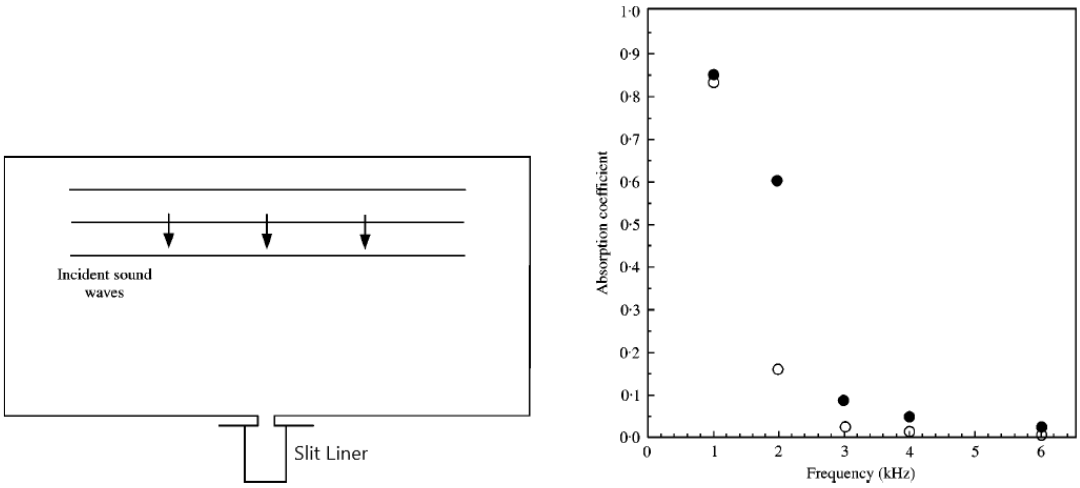

(a) Computational Setup with Slit Liner

(b) Absorption Coefficient at SPL = 130 dB, Legend: (●)Simulation, (○)Experiment

Figure 2.6: Description of numerical study of Tam et al. [67]

Zhang & Bodony [74], on the other hand, conducted a DNS campaign to mimic the effects of a 3-dimensional honeycomb liner, under acoustically excited conditions. Their simulations established that the in-orifice flow is dependent on the phase of the incident acoustic excitation, where substantial flow through the orifice can exist at certain phases and flow separation at the edge of the orifice walls can exist at others. The evolution of orifice flow and thus the acoustic dissipation mechanism at different sound amplitudes was also analysed using the λ_2 criterion as shown in figure 2.7. Lower flow penetration into the cavity at SPL = 130 dB reflects on the fact that the main noise dissipation mechanism is the orifice-wall friction, while at SPL values $\geq$ 150 dB the dissipation is mainly due the vorticity shed into the cavity. These observations are in-line with Sivian [63]. Finally, Zhang & Bodony [74] used the Dean's method (see section 2.2.2) to educe liner impedance and found a reasonable comparison with the experimental results, except a discrepancy in the normalised resistance at f = 3 kHz. Similar trends were observed with the normalised reactance curves.

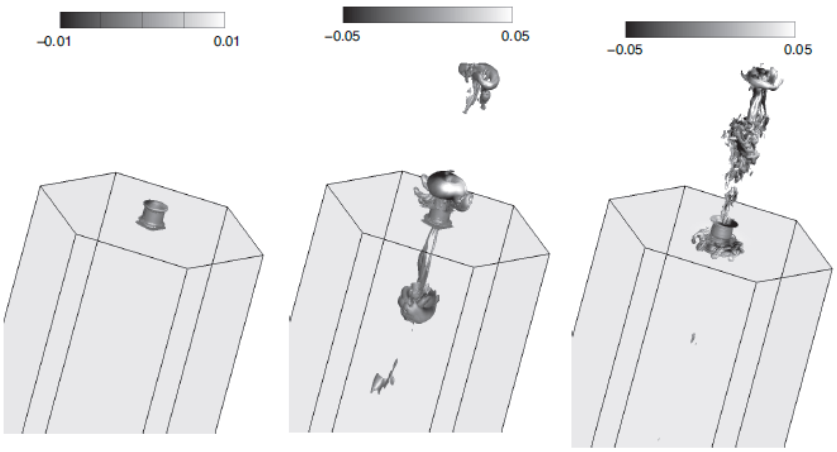

(a) SPL = 130 dB (b) SPL = 150 dB (c) SPL = 160 dB

Figure 2.7: λ_2 criterion plotted at f = 3 kHz [74]

Zhang & Bodony [73] further extended their DNS study to mimic the effects of 3-dimensional acoustic liner under grazing flow conditions. They observed that the vorticity penetration into the honeycomb cavity is a stronger function of acoustic sound amplitude than of the turbulence in the grazing flow. However, the turbulent grazing flow increased the peak orifice velocity by a factor of two, which increased the dissipation due to orifice-wall friction. This was reflected by the fact that the liner resistance at low

sound levels, where the acoustic dissipation is mainly caused by the viscous dissipation at the orifice walls, was higher for the grazing flow case. This is shown in the porosity normalized resistance curve in figure 2.8. On the other hand, introduction of grazing flow has hardly any effect on the normalised reactance values.

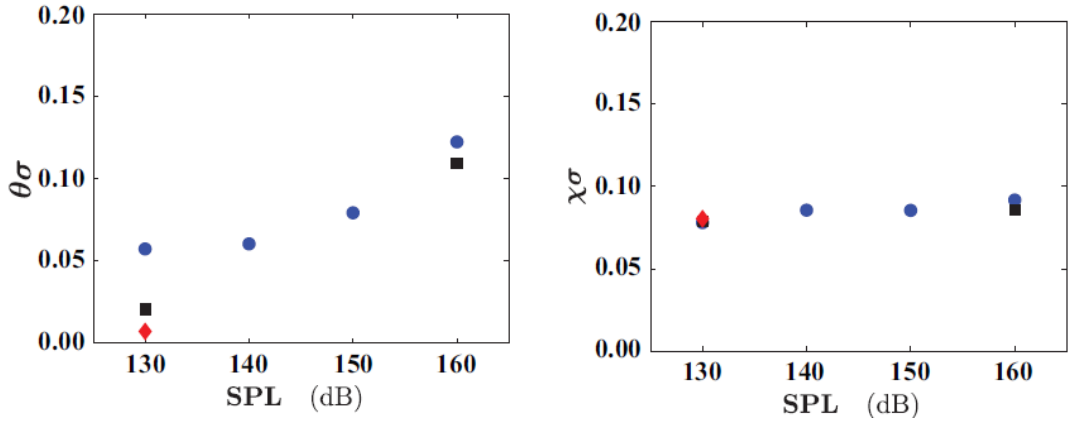

(a) Porosity Normalised Resistance (b) Porosity Normalised Reactance

Figure 2.8: Normalized impedance at different SPL for grazing flow condition, Legend: (◆)no flow, (■)Laminar boundary layer, (●)Turbulent boundary layer [73]

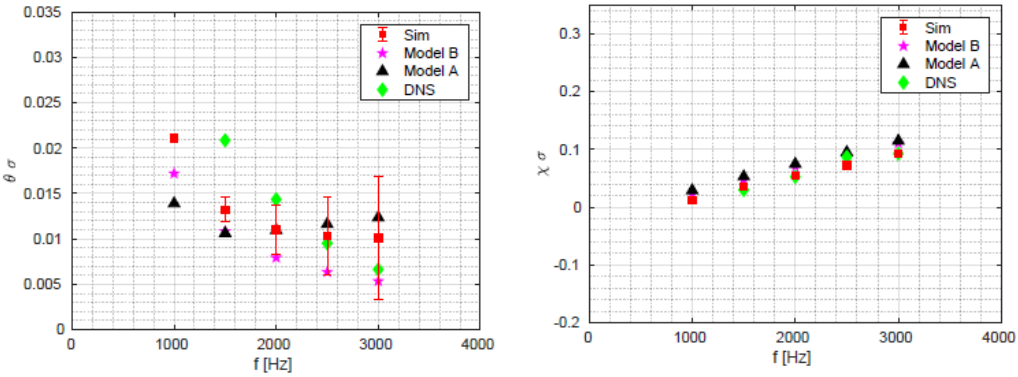

(a) Porosity Normalised Resistance (b) Porosity Normalised Reactance

Figure 2.9: Normalized impedance at different SPL for grazing flow condition, Legend: Model A - Melling's Model, Model B - Motsinger's Model [43]

The discussion of numerical studies given above proves that the Direct Numerical Simulations (DNS) are a useful tool to not only educe impedance but also give a physical interpretation of the result. However, the use of DNS is limited due to a large requirement of the computational resources. With such limitations, LBM provides an innovative alternative to DNS. Manjunath et al. [43] conducted a numerical study on honeycomb liners under acoustically excited flow, using LBM-VLES and validated the impedance results against the DNS results in [74] as shown in figure 2.9 . In the figure, model A and model B represent Melling (equation 2.13) and Motsinger models (equation 2.14 & 2.15) respectively. It is seen that the the porosity-normal reactance of the LBM simulation is in quantitative agreement with DNS and semi-empirical models. On the other hand the resistance values exhibit correct trends but show quantitative difference especially at frequency close to the liners resonant frequency ($\approx$1.1 kHz). These deviations could arise due to the fundamental difference between the two numerical schemes (DNS and LBM) as well as from the difference in the computational setup.

The numerical simulations discussed in this section, with DNS and LBM schemes, are extremely time intensive, mainly because of the effort to resolve in-orifice flow structures and the boundary layer (applicable only for grazing flow conditions). For instance the case ran by Manjunath et al. [43] consumed

a total of 466.93 CPU-hours on a Xenon E5-2697 2.6 GHz. Such long CPU-hours are a burden on the available resources.

Numerical Simulations with Impedance Boundary Condition

An alternative method to model the effects of the acoustic liner is to use an IBC in combination with a numerical scheme such as DNS or LBM. In this method, the need to resolve the in-orifice flow structures can be bypassed as the impedance is directly prescribed at the wall. The standard formulation of the IBC with a mean flow, assumes a thin zero velocity fluid layer near the wall which is separated from the mean flow by a vortex sheet as shown in figure 2.10. In the figure 2.10, the position of the thin vortex sheet is given by $y = \delta_b$. It is generally admitted that the acoustic normal displacement and the acoustic pressure are continuous across the boundary layer, which leads to the well-known Ingard-Myers boundary condition as given below [47],

$$u_n(i\omega) = \frac{p(i\omega)}{Z(i\omega)} \underbrace{+ U_\infty \cdot \nabla\left(\frac{p(i\omega)}{i\omega Z(i\omega)}\right)}_{\text{convective term}} \underbrace{- \frac{p(i\omega)}{i\omega Z(i\omega)} n \cdot (n \cdot \nabla U_\infty)}_{\text{curvature term}} \tag{2.26}$$

where n is the normal vector pointing outwards from the wall, U_∞ is the freestream velocity, and u_n and p are complex acoustic velocity and complex acoustic pressure above the lined surface respectively. In the above equation, the convective term shows the effects of the convection with the mean flow while the effect of the curvature of the impedance surface is accounted by the curvature term. It should be noted that the equation 2.26 is only valid under a limit of vanishing fluid layer thickness ($\delta_b \to 0$) and an infinitely small vortex sheet deflection ($\eta \to 0$), i.e. $0 < \eta \ll \delta_b < 1$. Tester [69] has found that the boundary condition mentioned in equation 2.26 leads to an unstable solution, due to a Kelvin-Helmholtz type instability arising from the vortex sheet interface. This instability renders the boundary value problem ill-posed in time domain [66], which is of particular interest as most liner analysis involves time domain simulations. Rienstra [57] has stated that the instabilities occur due to the time domain representation of impedance which is originally defined in the frequency domain. He stresses that all conversions from frequency domain to time domain are not possible and they must satisfy certain constraints [57]. However, this is not always possible and thus time-domain instabilities persists.

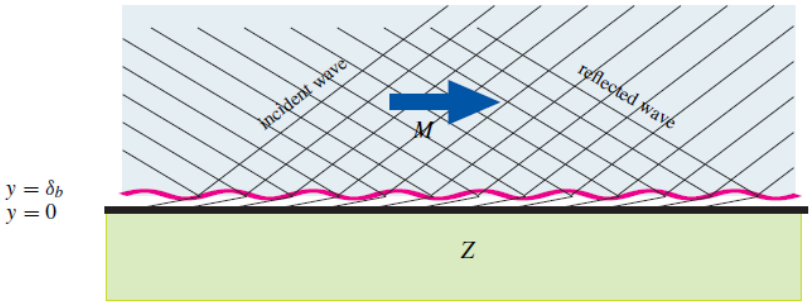

Figure 2.10: Geometrical representation of the Ingard-Myers boundary condition [57]

Studies such as that conducted by Tam & Auirault [66] have pointed that this instability is non-physical in nature, and the assumption of a thin-vortex layer is futile as in reality no such vortex sheet exists in the flow. They stressed on including the effect of the mean flow on acoustic impedance directly without introducing a vortex-sheet discontinuity. Numerically stable implementations of the Ingard-Myers boundary condition might be achieved by selective filtering of the unstable modes and coarsening of the grid. Filtering and coarsening adds additional dissipation which can prevent the instability from growing. This option has been explored by Richter et al. [56]. They further simulated the NASA - Grazing Impedance Tube (GIT) (similar to setup shown in figure 2.5), to model the effects of a ceramic tubular liner using two different time domain implementations of equation 2.26, namely, the 3-parameter MSD model [66] and the extended Helmholtz resonator model [57]. Richter et al. [56] observed a good match with the experimental results at all operating conditions, except at low frequencies of 0.5 kHz

and 1 kHz, results of which are shown in figure 2.11. The discrepancy at 0.5 kHz is attributed to a standing wave pattern that exists in the entire computational domain, while that at 1 kHz is attributed to a spatially growing Tollmein-Schlichting type instability. It should be noted that in the figure 2.11, EFI represents the MSD model while EHR is the extended Helmholtz resonator model.

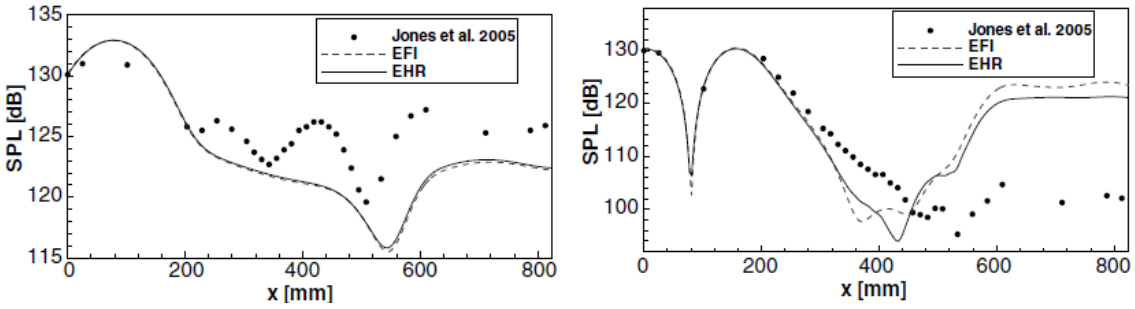

(a) f = 0.5 kHz (b) f = 1 kHz

Figure 2.11: Comparison of SPL recorded with different Time Domain Impedance Boundary Condition [56]

From the discussion presented above, it is clear that the instabilities arise because of the simplified modeling assumptions associated with the use of the Ingard-Meyers boundary condition (equation 2.26). Thus, a method to facilitate a stable IBC could be to resolve the boundary layer and use it in combination with a nominal impedance. Here, 'nominal impedance' means the impedance value in a stagnant medium (equation 1.1). With a resolved boundary layer, the Ingard-Meyers boundary condition (IMBC) becomes obsolete and thus, the instability issues arising due to the modeling assumptions of the IMBC can be tackled. However, it should be noted that resolving the boundary layer completely can increase the computational cost, which is against the whole purpose of using an impedance boundary. In this case, the question is what level of resolution of the boundary layer is required to efficiently capture the effect of mean flow on the lined wall.

Based on the above assumption, Richter & Thiele [55] used an 'artificial' boundary layer profile instead of a fully resolved boundary layer. However, they raised questions at the robustness of this method, as they observed that the results with an artificial boundary layer are highly sensitive to its' thickness. Burak et al. [10]. conducted simulations with Large Eddy Simulations (LES) and Linearized Navier Stokes Equation (LNSE) to model the effect of the ceramic tubular liner [50]. They resolved the boundary layer upto the log law region, and used the 3-parameter MSD model to account for the impedance boundary in time domain. Burak et al. [10] observed a good match with the experimental results conducted by Jones et al [50]. Moreover, they were able to capture the hydrodynamic instabilities at f = 1 kHz, which is in agreement with the experimental results. A limitation of this study stems from the fact that it decouples the acoustic and hydrodynamic fields and treats them separately. However, in reality the hydrodynamic and acoustic effects are extremely coupled.

The discussion presented in this section shows that the use of an IBC remains a bottleneck due to stability issues. The stability issues arise because of the simplified modeling assumption, which probably is due to our lack of knowledge regarding the physical interaction between the flow and liner cavities [48]. Numerical simulations with a liner geometry can help improving our understanding of the physical processes, however their widespread use is limited because of high computational requirements.

2.2.4. Important Takeaways

Some of the major limitations of the models in section 2.2 are summarised below,

- The use of theoretical models to characterise liner impedance is limited, due to their inability to accurately account for the non-linearities. This can be regarded to our limited understanding of the flow physics in the vicinity of the liner, especially in the non-linear regime.
- Characterising acoustic liners through experiments is a widely used method, however, they often have cumbersome installation requirements. Moreover educing liner impedance, especially un-

der grazing flow conditions, is a contentious topic in the field of liner research. This again stems from our limited knowledge of the interaction between the flow and the acoustic field in the vicinity of the liner.

- Numerical simulations with a liner geometry can improve our understanding of the acoustic-flow interactions, however they require large computational resources.
- Combining numerical simulations with an IBC can reduce the burden on the computational resources, but the stability issues associated with it remain a bottleneck.

The limitations associated with the impedance eduction methods discussed in the current chapter act as a motivation to investigate alternate modeling approaches. From the points mentioned above, it can be said that a new model should be stable in time domain and that it should not be based extensively on the near/ in-orifice flow physics. Moreover, it should alleviate the burden on the available computational resources. Thus, exploring the prospect of using the equivalent fluid modeling option for mimicking the acoustic effects of honeycomb liner is justified. The basic concepts of this type of modeling and the associated assumptions are discussed in chapter 3.

3

Equivalent Fluid Region

The previous chapter summarises some of the most common impedance eduction methods to characterise the SDOF liners. It has been concluded that the general understanding of the near and in-orifice flow physics is limited, especially in the non-linear flow regime. This limitation has consequently thwarted the development of theoretical models. Moreover, cumbersome installation requirements also restrict the use of empirical methods to understand the flow dynamics in the vicinity of the acoustic liner. In this scenario, numerical methods have proven to be successful, in not only offering a better understanding of the near orifice flow dynamics but also in providing reasonably accurate impedance values. However, the numerical simulation with an actual liner geometry is a burden on the computational resources. An alternative might be to replace the liner geometry in the numerical setup with an IBC, however, the use of this boundary condition is bounded by instability issues and ill-posed problems.

The following sections explore the plausibility of modeling the acoustic effects of SDOF liners using the equivalent fluid approach. Traditionally, this approach is used to mimic the acoustic effects of the extended-reacting type liners such as porous materials. Thus, before discussing the prospect of using the equivalent fluid modeling for SDOF liners, it is essential to familiarise oneself with the use of equivalent fluid models for porous materials. Hence, the concept of equivalent fluid regions for porous materials is introduced in section 3.1. Thereafter, a case is developed for the use of the APM formulation, which is an equivalent fluid model in PowerFLOW®, for mimicking the acoustic effects of honeycomb liners in section 3.2. Finally, the chapter concludes with the research objectives and the research questions of the current thesis in section 3.3.

3.1. Equivalent Fluid Modeling for Porous Materials

Porous materials are extended-reacting type liners that have proved to be an ideal choice for sound absorption over a broadband frequency range. Generally, porous materials such as felt/ foams consist of a complex microscopic topology. This is apparent from figure 3.1, where an open-cell and a closed-cell polyethylene foam are shown. The acoustic effects of such porous materials are strongly dependent on their complex internal-structures. For example, closed-cell foams are usually highly reflective and thus poor absorbers as the motion of the incoming acoustic wave is thwarted by the closed cells. Alternatively, open-cell foams are usually good sound absorbers.

At a microscopic scale, the porous materials are generally inhomogeneous and the sound attenuation mechanism is usually attributed to [42]: i) the visco-thermal dissipation due to fluid flowing through the pores, ii) mechanical damping due to the frame, iii) the Helmholtz-type resonance, and iv) shedding of vortices at edges (applicable only under non-linear regime such as high SPL of input acoustic wave). Clearly, developing pure analytical descriptions of the above mentioned mechanism is an arduous task. Thus, porous materials are usually analysed at a macroscopic scale. If, the microscopic characteristic length is given by l_c^*, the macroscopic length (L_c^*) is defined such that $\lambda > L_c^* \gg l_c^*$, where λ represents the acoustic wavelength. A description of different length scales in the acoustic problem is shown in

figure 3.2. At a macroscopic scale, along with a rigid frame approximation, a porous material can be replaced by an equivalent fluid region [40]. This region is characterised by the same bulk modulus (K) as the saturating air inside the porous material, and a complex density (ρ) which accounts for the visco-inertial interactions of the acoustic wave with the frame.

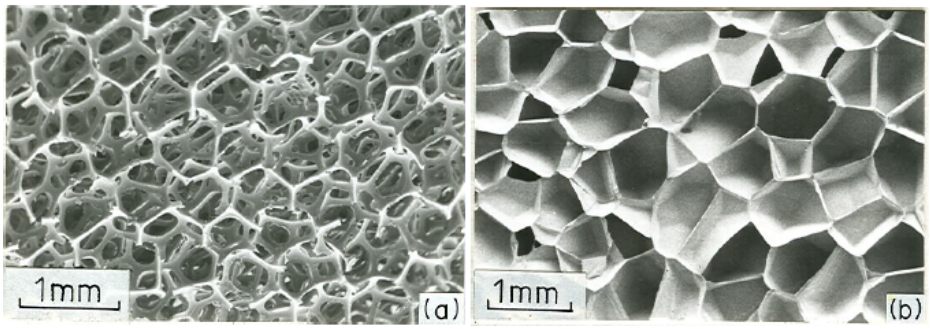

(a) Open-pore type (b) Closed-pore type

Figure 3.1: Scanning Electron Microscope (SEM) graph for different polyurethane foam [23]

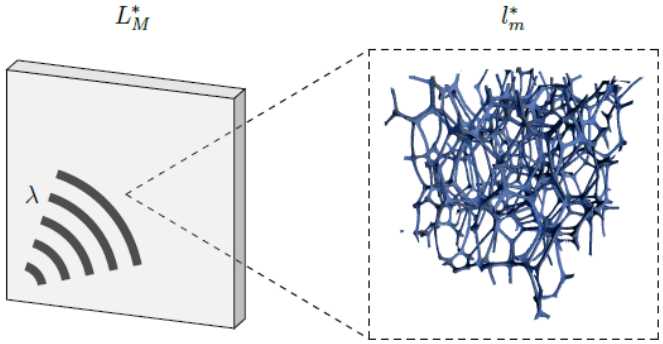

Figure 3.2: Different length scales of a porous material[22]

3.1.1. Relevant Equivalent Fluid Models

One of the most commonly used theoretical model based on the macroscopic description explained above was originally formulated by Johnson et al. [28], to which additions were made by Champoux & Allard [13]. This model is essentially called the Jonhson-Champoux-Allard (JCA) model. It uses five parameters to characterise a porous material, namely the acoustic porosity (ϕ), the tortuosity (α_∞), the static flow resistance (σ), and the viscous and thermal characteristic lengths are represented by Λ and Λ' respectively. According to the JCA model, the effective density ($\tilde{\rho}$) and effective bulk modulus of an equivalent fluid is given as,

$$\tilde{\rho}(\omega) = \frac{\alpha_\infty \rho_0}{\phi}\left(1 + \frac{\sigma\phi}{i\omega\rho_0\alpha_\infty}\sqrt{1 + \frac{4i\alpha_\infty^2\mu\rho_0\omega}{\sigma^2\Lambda^2\phi^2}}\right) \tag{3.1}$$

$$\tilde{K}(\omega) = \frac{\frac{\gamma P_0}{\phi}}{\gamma - (\gamma-1)/\left(1 + \frac{8\mu}{i\Lambda'^2 Pr\omega\rho_0}\sqrt{1 + \frac{i\rho_0\omega Pr\Lambda'^2}{16\eta}}\right)} \tag{3.2}$$

where ω is the angular frequency, μ represents the dynamic viscosity, Pr is the Prandtl number (0.71 for air), γ is the specific heat ratio and P_o is the atmospheric pressure. The complex effective density ($\tilde{\rho}$) is the density experienced by the acoustic wave travelling through the equivalent fluid, while the complex effective bulk modulus ($\tilde{K}$) is the ratio of pressure applied to the equivalent fluid to the fractional change

in its volume. Equation 3.1 and equation 3.2 can be further used to calculate characteristic impedance Z_c, which essentially gives the normal surface impedance of the equivalent fluid (Z).

$$Z_c = \sqrt{\tilde{K}(\omega) \cdot \tilde{\rho}(\omega)} \tag{3.3}$$

$$Z = -iZ_c \cot(kd) \tag{3.4}$$

where d is the length of the equivalent fluid region and k is the wavenumber. Another relevant equivalent fluid model is the APM formulation implemented in the LB based solver, PowerFLOW®. The APM model provides a comparatively easier implementation than the JCA model as it requires the knowledge of only two equivalent fluid parameters, i.e. the flow resistance (σ) and the material porosity (ϕ), compared to five parameters in the latter case. For a detailed discussion on the numerical implementation of this model, the reader is referred to chapter 4.

The current discussion shows that the equivalent fluid models are characterised through macroscopic parameters such as the static flow resistance (σ), porosity (ϕ), tortuosity (α_∞), etc. Thus, with the knowledge of these parameters the impedance offered by a porous material to an incident acoustic wave can be determined. These characterising parameters can be either obtained through analytical models [6], or empirically through experiments [61].

3.1.2. Numerical Simulations with Equivalent Fluid Model

Pérot et al. [51] modelled the sound absorption property of a porous material using an equivalent fluid model in PowerFLOW®. The current study used a high porosity assumption ($\phi \approx 1$) and thus only the resistance to characterize the material under investigation. Pérot et al. [51] simulated the equivalent fluid model in a Digital Normal Impedance Tube (DNIT) setup, illustration of which is shown in figure 3.3. In the setup the sample thickness and air layer thickness is represented by d and e respectively, while σ_x represents the flow resistance in x-direction.

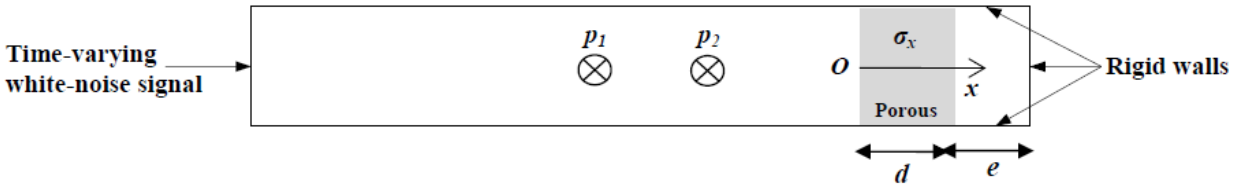

Figure 3.3: 2D representation of Computational Impedance Tube Setup [51]

Figure 3.4 shows the absorption coefficients educed with different methods in the numerical study of Pérot et al [51]. Although the simulation results exhibit correct trends, they underestimate the experimental value within a maximum error range of 20-30%. With only one macroscopic parameter characterizing the porous material, the accuracy of impedance prediction is bound to be affected. However, when an air layer (e) is introduced, the estimation of absorption coefficient are in better agreement and the shape of the plot is well captured as shown in figure 3.4. This trend is related to the fact that for a APM-air layer combination, the absorption characteristic is less sensitive to accurate modelling of the only the APM [51]. Another interesting observation from figure 3.4(b) is the increased absorption at low frequencies compared to the configuration used in figure 3.4(a). However, Pérot et al [51] have not mentioned the physical reasons that might have caused this trend. In the current simulations the absorption coefficient was not a *priori* known and the simulation parameters such as the resistance, sample thickness and air layer thickness were derived empirically.

Alternatively, with the *priori* knowledge of the absorption coefficient, the simulation parameters can be characterised using an inverse analysis. Pérot et al. [51] conducted simulations with the modified regression parameters and found improved predictions of the absorption coefficient. This can be seen in figure 3.5 where the estimation has greatly improved, especially in the case where e = 0. Deriving the equivalent fluid parameters through inverse formulation is also an integral part of the current thesis and is discussed in-depth in chapter 8.

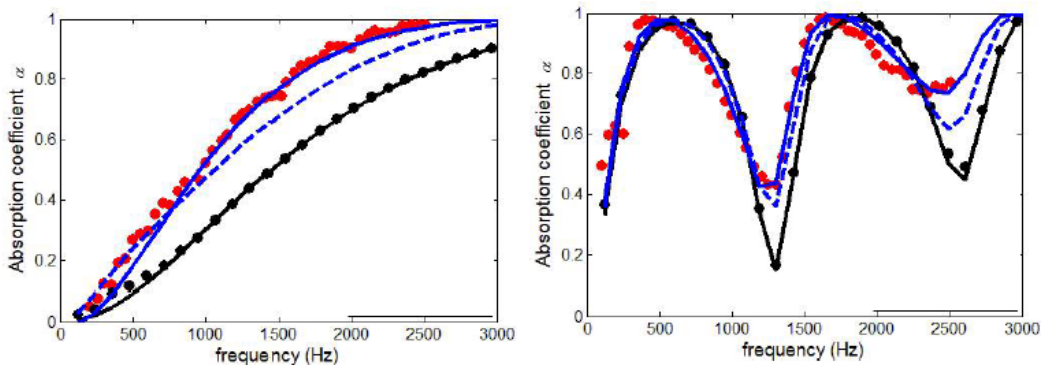

(a) e = 0 mm (b) e = 120 mm

Figure 3.4: Absorption coefficient as a function of frequency, Legend: (●)Simulation, Legend: (●)Experiment, (-)Analytical [51]

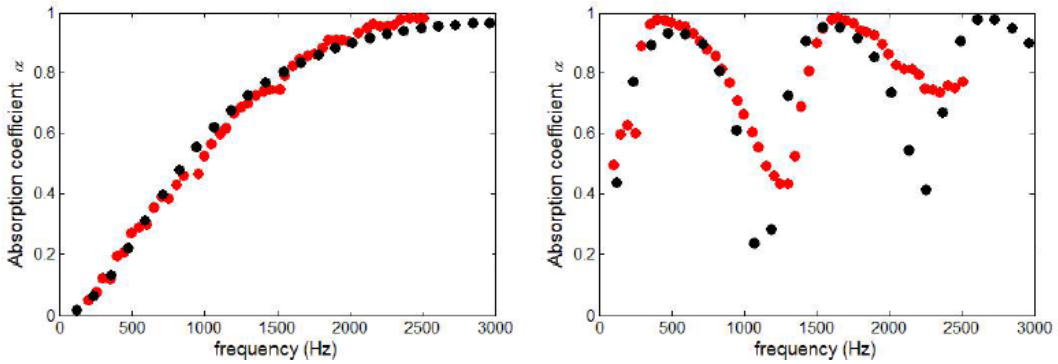

(a) e = 0 mm (b) e = 142 mm

Figure 3.5: Absorption coefficient calculated with regression parameters , Legend: (●)Simulation, (●)Experiment [51]

A numerical study to model a ceramic liner (shown in figure 3.6) as an APM was conducted by Sun et al. [65], who conducted simulations under no-flow and grazing flow conditions. In this effort, Sun et al. [65] characterised the porous material using both the flow resistance (σ) and material porosity porosity (ϕ). The equivalent fluid parameters, i.e. σ and ϕ were obtained from the experimental results of Jones et al. [50]. Under no-flow conditions, Sun et al. [65] were able to obtain a good overall comparison between the experiments and LBM simulations, especially at low frequencies as seen in figure 3.7. However at $f \approx 2000$ Hz which is close to the anti-resonance frequency of the porous material, the simulations underpredict the experimentally obtained absorption values. This discrepancy might be caused by the inability of the simulation to accurately model the near-antiresonance behaviour of the ceramic liner, possibly due to the fact that the model neglects thermal and structural effects which might dominate at $f \approx 2000$ Hz. The results from the simulations under no-flow conditions are important for the current thesis as they are used in the verification of the APM-CFD numerical setup in chapter 6.

Under grazing flow conditions, Sun et al. [65] simulated a Grazing Flow Impedance Tube, similar to that shown in figure 2.5. The acoustic performance was studied by analysing the Sound Pressure Level (SPL) values at different inflow Mach number (M=0, 0.1, 0.3). Figure 3.8 shows the SPL plots at M=0.1. From the figure, it is evident that the implemented model is in good agreement with the experimental data, proving the ability of the APM model to correctly predict the sound absorption in presence of grazing flow. Moreover, Sun et al. [65] concluded that the APM model naturally avoids the instability issues such as that associated with the implementation of IBC. This is because APM directly solves the equations in time domain, hence, it bypasses the issues associated with the conversion of impedance from frequency domain to time domain as discussed in section 2.2.3. These stability issues are a bottleneck for conventional IBC applications, as discussed in chapter 2.The fact that the APM formulation under grazing flow condition is devoid of such concerns is a major advantage.

The discussion presented in this section presents some of the relevant numerical studies conducted with the APM formulation. Sun et al. [65] have reported that the APM model characterised using two macroscopic properties σ and ϕ can accurately model the acoustic effects of a rigid frame porous material not only under no-flow conditions but also under grazing flow conditions. Now, the challenge is to extend the use of the equivalent fluid models, the APM formulation in particular, for mimicking the acoustic effects of honeycomb liners.

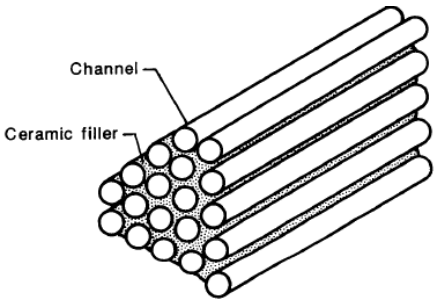

Figure 3.6: Schematic of a ceramic liner [50]

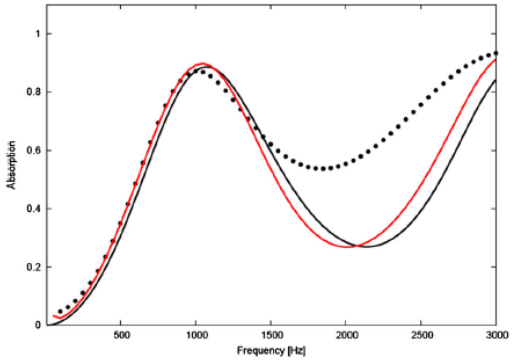

Figure 3.7: Absorption Coefficient (no-flow case), Legend - (●)Experiment, (-)Analytical, (-)Simulation [65]

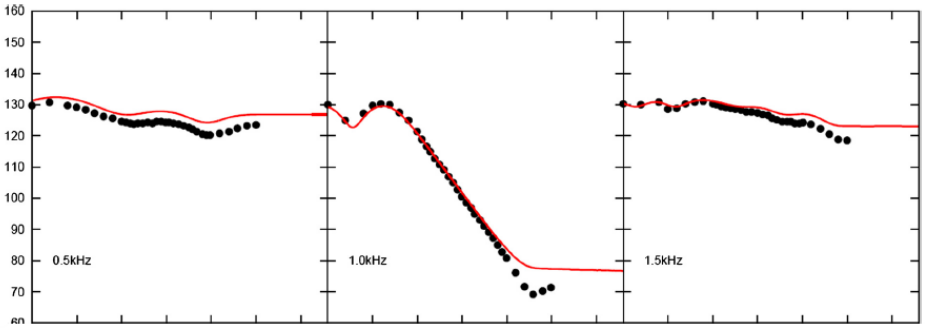

Figure 3.8: SPL recorded for M = 0.1, Legend - (●)Experiment, (-)Simulation [65]

3.2. Equivalent Fluid Modeling for Honeycomb liners

From the discussion given in chapter 2, it is seen that the acoustic effects of the honeycomb liner are essentially dependent on the liner geometry and the nature of the input signal (i.e. its SPL and frequency). Moreover, the acoustic absorption is attributed to the physical processes within the vicinity of the liner orifice, such as the viscous losses at the orifice wall and the vortex shedding from the edge of the orifice as shown in figure 2.7. Conventional methods for mimicking the acoustic effects of the honeycomb liner seek to model such near/ in-orifice flow phenomenons [64]. Conversely, the equivalent fluid models are based on the macroscopic representation of porous materials, which exhibit completely different flow dynamics than honeycomb liners. Therefore, it can be said that equivalent fluid modeling for honeycomb liners is an effort to represent its' acoustic effects through the equations that govern the acoustic absorption inside a porous medium.

Thus, with the knowledge of appropriate model parameters, the equivalent fluid models should ideally be able to reproduce the acoustic effects of the reference liner. However, obtaining these parameters for a honeycomb liner is not straightforward. While the honeycomb liners are characterised through their impedance (Z), the equivalent fluids are characterised through parameters such as the static flow resistance (σ), fluid porosity (ϕ), etc. Hence, there is no direct correspondence between the parameters that define a honeycomb liner and those that define an equivalent fluid. Moreover, there is a

major underlying assumption in the use of the equivalent fluid approach for honeycomb liners. This assumption stems from the fact that the honeycomb liners are locally-reacting type liners, while the porous materials are extended-reacting type. Modeling a locally-reacting liner as an extended-reacting liner is not entirely physical and might not even be feasible.

Nevertheless, in the current thesis, the APM model available in the flow solver, PowerFLOW® is used to mimic the honeycomb liner effects. The possible advantages of using this formulation are summarized in section 3.2.2. However, first a discussion is presented on the equivalent fluid implementation of Atalla & Sgards [6] in section 3.2.1. This implementation seeks to model the honeycomb liners based on the JCA model as given in section 3.1.1.

3.2.1. Jonhson-Champoux-Allard Model for Honeycomb liners

Atalla & Sgards [6] attempted to extend the use of the JCA model (see section 3.1.1) for the cavity backed perforated facesheets such as that shown in figure 1.2(a). As defined earlier, the JCA model is characterise by five parameters, namely the porosity (ϕ), tortuosity (α_∞), viscous characteristic length (Λ) thermal characteristic lengths (Λ') and the flow resistance (σ). Atalla & Sgards [6] have said that perforated plate with straight cylindrical holes, ϕ is equal to the plate porosity and Λ and Λ' is equal to the orifice radius r. Thus, three of the five parameters can be directly related to the geometry of the perforated facesheet

On the other hand, Atalla & Sgards [6] derive the equivalent tortuosity α_∞ as a function of the characteristic length (ϵ_o) of the perforated facesheet. This is indeed an interesting correlation between the properties of a porous material and the that of a perforated facesheet. While the correction length (ϵ_o) represents the increased length of the oscillating mass in the liner cavity (see section 2.2.1), the tortuosity α_∞ represents the extended distance that the flow has to travel due to curvatures within the structure of porous material. For a configuration of a perforated facesheet backed by a honeycomb cavity the equivalent tortuosity can be defined as,

$$\alpha_\infty = 1 + \frac{2\epsilon_o}{t_f} \tag{3.5}$$

where t_f is the thickness of the facesheet. The correction length ϵ_o is usually given through empirical relations such as that shown in equation 2.15. The only remaining unknown in the JCA model is the static flow resistance (σ). Rather than using the static flow resistance, Atalla & Sgard [2] used the expression for the dynamic flow resistance as follows,

$$\sigma_{\text{dynamic}} = \left(\frac{2d_o}{r} + 4\frac{\varepsilon_o}{r}\right)\frac{R_s}{\phi} \tag{3.6}$$

where R_s is the surface resistance which is given by $0.5\sqrt{2\mu\rho\omega}$. Here the term 'dynamic' shows that that the flow resistance is dependent on the frequency of the input acoustic signal. Thus, starting from equation 3.1 and equation 3.2, and using the assumptions explained in the current section, the JCA model for a perforated facesheet backed with a cavity can be derived as,

$$Z = \underbrace{\left(\frac{2t_f}{r} + 4\frac{\varepsilon_o}{r}\right)\frac{R_s}{\phi}}_{\text{I}} + \underbrace{\frac{1}{\phi}\left(2\varepsilon_o + t_f\right)\mathrm{j}\omega\rho_0}_{\text{II}} - \underbrace{\mathrm{j}\rho_0 c_\infty \cot(kL)}_{\text{III}} \tag{3.7}$$

where the correction length ϵ_o is given by $0.85r(1 - 1.14\sqrt{\phi})$. Equation 3.7 as Atalla & Sgards [6] were able to formulate an equivalence between the equivalent fluid model for a porous medium and a cavity backed liner. Term I in equation 3.7 represents the resistance due to viscous effects and due to the end corrections. Term II represents the mass reactance which is associated with the orifice mass-inertia, while term III is the cavity reactance. Moreover, it should be noted that term I and term II are applicable under the high frequency limit which is in accordance with Crandall [17].

A clear disadvantage of this equivalent fluid model is its dependence on the discharge coefficient C_D,

as its accurate prediction remains a bottleneck even for the traditional theoretical models discussed in section 2.2.1. Anyways, the efficacy of this model to mimic the acoustic effects of liners is compared with that of the APM in chapter 9.

3.2.2. Acoustic Porous Medium for Honeycomb liners

The use of extending the equivalent fluid approach, the APM formulation in particular to mimic the acoustic effects of a honeycomb liner is supported by certain possible advantages that are summarized below,

- As discussed earlier the implementation of an IBC might lead to a stability issues and eventually an ill-posed problem in time domain. Rienstra [57] has suggested that this occurs due to the time domain representation of impedance (Z), a value which is originally defined in the frequency domain. The use of an APM, on the other hand, can bypass the stability issue as it solves the equations, that naturally damps the acoustic waves, directly in time domain.
- A probable disadvantage of using an IBC to mimic the acoustic effects of a honeycomb liner stems from the fact that the acoustic and flow fields are often decoupled. Whereas, it is well known that the acoustic and flow fields in the vicinity of the liner are strongly coupled. An APM, on the other hand, is not a boundary condition but a region with modified properties with respect to air, such that the the sound waves can travel through it. Thus, it is possible that the acoustic and flow effects can be coupled with the use of APM.
- As mentioned earlier, modelling assumptions based on the flow physics in the vicinity of the honeycomb liner might be flawed/ too simplistic due to a limited knowledge of the fluid dynamics in the vicinity of the liner. However, this is not a concern for the APM model, as it is a macroscopic representation of the porous medium based on Darcy's law [16] and not based on the near/ in-orifice fluid dynamics.
- With the APM model, the need to resolve the near/ in-orifice flow field can be bypassed and consequently, the burden on the computational resources can be alleviated.

With such possible advantages of the APM approach, it makes sense to access its capability to mimic the acoustic effects of a SDOF Honeycomb liner.

3.3. Research Objective and Questions

The discussion presented in chapter 2 gives a clear motivation to analyse alternate methods to mimic the acoustic effects of honeycomb liner. Following this, the equivalent fluid approach is discussed in chapter 3 and strong arguments are given in support of using the APM formulation. Thus, based on the knowledge gained in the previous chapters, the thesis objective is to:

Determine a methodology to model the effects of a honeycomb acoustic liner by implementing and validating the Acoustic Porous Medium formulation available in PowerFLOW®

Following the research objective, the major research questions for the current thesis can be formulated. The first research question focuses on finding simulation parameters which will aid in accurate modeling of the liner effects. This research question can be answered in parts through sub-questions

1. **What kind of resources are required to accurately simulate the effects of a honeycomb liner with an APM?**
    - What simulation parameters are required to accurately simulate the honeycomb liner and the APM?
    - What is the required grid resolution to accurately discretize the acoustic and the flow field?

The next question focuses on the desire to validate the use of the APM formulation for acoustically excited flows. A challenge associated with equivalent fluid modeling is to derive the model parameters

that correspond to the acoustic effects of the reference honeycomb liner. This is tackled through the sub-questions which seek to investigate two different methods to derive the characterising parameters of the APM.

2. **Can the effects of an honeycomb acoustic liner, for an acoustically excited flow, be predicted by the Acoustic Porous Medium formulation available in PowerFLOW®?**
    - Can the APM be characterised through the inverse formulation present in PowerCASE®?
    - Can the APM be characterised through the pressure drop experiment?
    - What are the possible sources of discrepancies between the simulation and reference results? If any.

II

Methodology

4

Numerical Scheme

In the current chapter, a discussion is presented on the implementation of the numerical scheme which is employed within the flow solver PowerFLOW®. Unlike most conventional CFD flow solvers which are based on the discretization of the macroscopic continuum equations, i.e. the NS equations, PowerFLOW® uses the LBM which is based on the mesoscopic kinetic equations. Thus, within this chapter the fundamentals of LBM along with its main equations are given in section 4.1. Thereafter, the numerical implementation of the APM, which is an equivalent fluid formulation employed in PowerFLOW® is presented. For a detailed discussion on LBM and its implementation within PowerFLOW®, the reader is referred to [52] and [14] respectively.

4.1. Fundamentals of the Lattice Boltzmann Method

4.1.1. Boltzmann Transport Equation

LBM is based on Ludwig Boltzmann's kinetic theory of gases [3]. Unlike the NS equations that assumes a macroscopic continuum, the kinetic theory treats the fluids/ gases as a collection of substantial amount of discrete particles with a random motion. The interaction between the particles and the subsequent exchange of momentum and energy is achieved through particle streaming and collision [7]. The streaming and collision process can be modelled through the Boltzmann transport equation which is a PDE given by:

$$\frac{\partial f}{\partial t} + e \cdot \frac{\partial f}{\partial x} + F \cdot \frac{\partial f}{\partial e} = \Omega \tag{4.1}$$

where the particle distribution function $f(x,e,t)$ gives the probability of finding a particular molecule with a given position and momentum, while e is the continuous microscopic velocity. In the above equation, the time (t) and space (x) evolution of the particle distribution function is controlled by the collision operator Ω, whereas the influence of the external forces is modelled through the external force vector F.

LBM can be considered as a simplification to Boltzmann's kinetic theory of gases which is achieved by reducing the number of particles and confining them to the lattice node [7]. Besides this, LBM introduces an intermediate scale, i.e. the mesoscopic scale, which offers a mesoscopic description of the flow field alternately to the microscopic treatment in the kinetic theory and the macroscopic treatment of the NS equations. Moreover, LBM restricts the motion of the particle to certain finite grid positions called as the lattice nodes. In such a treatment, the continuous distribution function $f = f(x,e,t)$ is replaced with $f_i = f_i(x_i,e_i,t)$, which is the probability of finding a particle streaming along the direction i with a discrete microscopic velocity e_i.

4.1.2. Lattice Models

Lattices are an integral element in LBM as the permitted streaming directions and positions are defined on it. Besides this, the lattices also encompass the entire simulation volume. Various lattice models

can be incorporated within LBM such as those shown in figure 4.1. For a 2 dimensional setup, the LBM allows 9 streaming directions, while for its 3 dimensional counterpart, 19 streaming directions are allowed. These models are known as the $D2Q9$ and the $D3Q19$ respectively. The use of such models along with their associated streaming directions has proved to be sufficient for low speed cases, i.e. for $M < 0.4$, where the compressibility effects are negligible [52]. In the low supersonic and transonic regimes, i.e. for $M < 2$, complex models with higher number of streaming directions such as the $D3Q27$ might be required to properly capture the flow physics.

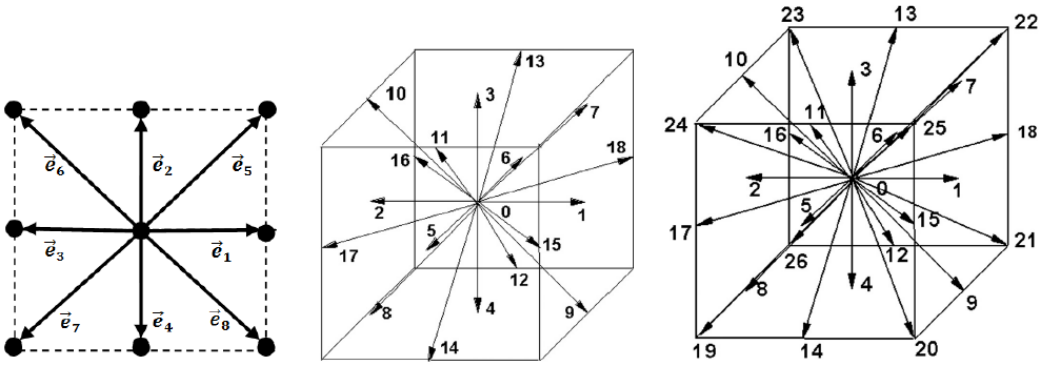

(a) D2Q9 [7] (b) D3Q19 [52] (c) D3Q27 [52]

Figure 4.1: Different lattice models used with LBM

4.1.3. Lattice Boltzmann Equations

With the knowledge of the discrete particle probability function $f_i(x,e_i,t)$ along with the assumption of no external forces F, the finite difference approximation of equation 4.1 leads to the main equation of LBM which is given as:

$$f_i(x + e_i\Delta t, t + \Delta t) - f_i(x,t) = \Omega_i \tag{4.2}$$

This equation is a time-explicit advection equation where the left hand term represents the streaming process and the right hand term represents the collision process. The discrete collision operator Ω_i is modelled using the Bhatnagar-Gross-Krook (BGK) approximation [8] as,

$$\Omega_i \approx -\frac{|f_i(x,t) - f_i^{eq}(x,t)|}{\tau} \tag{4.3}$$

In the above equations, f_i^{eq} represents the equilibrium distribution function and can be approximated using the Hermite expansion upto the 3rd order as mentioned by Sun et al. [65]. The single relaxation time τ is a function of the fluid viscosity (ν) and the temperature (T) and is given by the expression,

$$\tau = \frac{\nu}{T} + \frac{\Delta t}{2} \tag{4.4}$$

where Δt is the local time step. As discussed in section 4.1.4, the relaxation time is integral for turbulence modelling with the LBM. More importantly, the discrete function f_i can be linked to the macroscopic hydrodynamic quantities such as the macroscopic density and velocity by taking its zeroth and first-order moments,

$$\rho(x,t) = \sum_{i=0}^{N} f_i(x,t); \quad u(x,t) = \frac{1}{\rho(x,t)} \sum_{i=0}^{N} f_i e_i \tag{4.5}$$

where N is the number of points in the chosen lattice model and u represents the particle velocity.

4.1.4. Turbulence Modelling

For low Reynolds number flows, the current implementation of PowerFLOW® is equivalent to DNS, i.e. it resolves all the flow scales. However, as the Reynolds number increases, the size of the turbulence

scales decreases and hence, resolving all the flow scales becomes impractical. Thus, for high Reynold number flows, PowerFLOW® can employ turbulence modelling which is based on the two equation RNG $\kappa-\epsilon$ model, such that the effects of the unresolved smallest scales on the resolved larger ones can be modelled [68]. This method is called the Very-Large Eddy Simulation (V-LES), where the turbulence model provides the value of the dissipation rate (ϵ) and the turbulent kinetic energy (κ). The value of κ and ϵ is further used to calculate the turbulent relaxation time as shown below,

$$\tau_{turb} \approx C_{\mu} \frac{k^2/\epsilon}{T\,(1+(k|S|/\epsilon)^2)^{\frac{1}{2}}} \tag{4.6}$$

where $|S|$ is the local strain and C_{μ} = 0.09. In this formulation, the total effective relaxation time τ_e is the sum of the turbulent relaxation time (τ_{turb}), which represents the collisions due to turbulent interactions, and the relaxation time τ_o which accounts for the collisions due to molecular diffusion. Finally, the total relaxation time can be incorporated with the BGK approximation of the collision operator as shown below,

$$\tau_{eff} = \tau_{turb} + \tau_0; \quad \Omega_i \approx -\frac{1}{\tau_{eff}}\left(f_i - f_i^{eq}\right) \tag{4.7}$$

4.2. Numerical Implementation of the Acoustic Porous Medium

Following the discussion in section 4.1, the current section presents the numerical implementation of APM, which is an equivalent fluid formulation implemented in PowerFLOW®. This formulation is based on Darcy's law, which states that the pressure loss (∇p) is proportional to the transpiration velocity u through the fluid as shown below,

$$\nabla p = -\rho\sigma \cdot u \tag{4.8}$$

The above equation is known as Darcy's force term. The flow resistance (σ) is formed of two parts, namely the inertial resistance (σ_I) and the viscous resistance (σ_V). The viscous resistance is inversely proportional to the permeability K, while the inertial resistance is equal to the form coefficient (C).

$$\sigma = \sigma_u + \sigma_I u \tag{4.9}$$

$$\sigma_V = \frac{\mu}{\rho K} \quad , \quad \sigma_I = C \tag{4.10}$$

By using the Chapman-Enskog expansion, Chen et al. [14] have shown that the LB implementation shown in equation 4.2 is equivalent to the NS equation. Thus, the equivalent NS form of the LB equation for the APM is given by:

$$\frac{\partial \rho}{\partial t} + \nabla \cdot (\rho u) = 0 \tag{4.11}$$

$$\frac{\partial \rho u}{\partial t} + \nabla \cdot (\rho u u) = -\nabla p - \rho\sigma \cdot u \tag{4.12}$$

Equation 4.12 is the momentum equation for fluid flow, except for the fact that the regular viscous term is substituted by the Darcy's force term. However, outside the equivalent fluid region, Darcy's term vanishes and the viscous term reappears, showing that the equivalent fluid is a region with modified properties with respect to air. In this way, the current formulation can incorporate an equivalent fluid into the governing equations.

In PowerFLOW® the APM model uses the flow resistance (σ) and the material porosity (ϕ) to characterise the equivalent fluid region. The material porosity is given by:

$$\phi = 1 - \frac{\rho_p}{\rho_s} \tag{4.13}$$

where ρ_p and ρ_s is the overall density of the porous medium and the skeletal respectively. Furthermore, the APM considers a physical interface between the regular fluid region (for e.g. air) and the equivalent

fluid region. The material porosity (ϕ) is applied only at this interface, such that the mass-flux through the interface is conserved. The mass-flux conservation is given by:

$$|\rho u \cdot n|_{\infty} = \phi |\rho u \cdot n|_{\mathrm{APM}} \tag{4.14}$$

where the subscript ∞ and APM represent the real fluid and acoustic porous medium respectively. Another feature of the fluid-APM interface is the interface resistance due to the presence of the solid structure, which is a function of the material porosity and the flow velocity [65]. Furthermore, it should be noted that porous material properties such as surface roughness and thermal dissipation are neglected in the APM model. This simplification is reasonable only for low Mach number flows such that the assumption of an isothermal flows is valid.

5

Honeycomb Liner-CFD Setup Verification

The first part of the thesis has been devoted to verify the use of the Honeycomb Liner-CFD setup in PowerFLOW®, by evaluating the accuracy of the tool in mimicking the acoustic effects of the reference liner. The results from this chapter will be later used to find the APM parameters and asses its capability to mimic the liner effects in chapter 8. The general methodology applied in the verification process of the CFD setup is illustrated in figure 5.1. The simulations with the honeycomb liner as the reference geometry, uses a broadband acoustic signal as an input and gives the acoustic impedance (Z) for the liner as an output. The results from the simulations are then compared against that from the experiments and the analytical models. The reference experimental data used in the verification process are taken from the experiments conducted by Jones et al. [31], while the analytical models used for comparison in this chapter are based on the work of Melling [45] and Motsinger [46] (explained in detail in chapter 2).

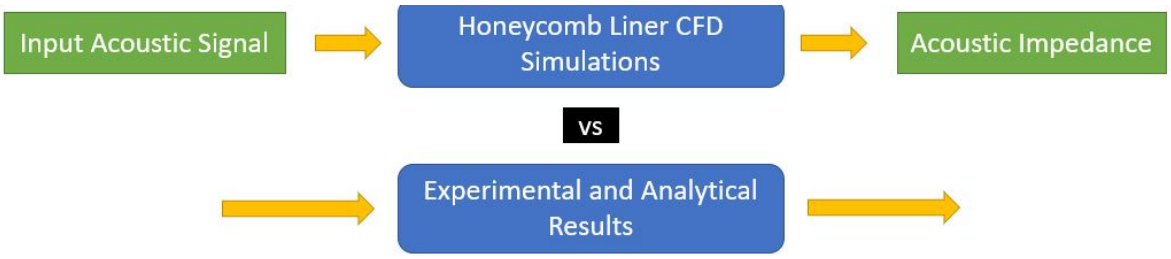

Figure 5.1: Illustration of the methodology employed in Liner-CFD verification

The current chapter starts with a detailed description of the numerical setup in section 6.2, followed by a description of the impedance eduction procedure in section 5.2. Thereafter, the input conditions for the simulations are stated in section 5.3. The grid convergence study is given in section 5.4, followed by a comparison of the current simulation results with those present in the state of the art in section 5.5. Finally, in section 5.6, the current chapter concludes with a verification study which seeks to explain the trends of the simulation results.

5.1. Description of the Numerical Set-up

The computational set-up for the case being discussed in the current chapter is based on the set-up provided with the OptydB toolkit [12], with modifications essentially in the nature of the input signal and in the different resolution regions. The current section gives a complete overview of the simulation parameters used to verify the liner-CFD setup. It should be noted that most simulation settings discussed in the subsequent subsections are also valid for the verification study of Acoustic Porous Medium-CFD setup. Further information on the latter case can be found in chapter 6.

Impedance Tube Set-up

The numerical setup used in the current thesis is the Digital Normal Impedance Tube (DNIT) which is similar to the NIT shown in figure 2.4(b). The DNIT essentially consists of two parts, namely a cylindrical waveguide and the geometry of the honeycomb liner. The input acoustic signal propagates in the positive x-direction and interacts with the honeycomb liner which is located at the extreme right of the tube. The waveguide and the honeycomb liner are encompassed by the cuboidal simulation volume as seen from the schematic given in the figure 5.2.

The length of the waveguide depends on the simulation time and is kept sufficiently long to avoid undesired reflections from the downstream extremity of the DNIT. A short impedance tube might lead to reflections and thus a spurious impedance spectra. The tube diameter on the other hand, depends on the maximum frequency of the input signal. In this setup, the diameter is based on the following relation:

$$D_{duct} = \frac{c_\infty}{1.71 f_{max}} \tag{5.1}$$

where D_{duct} is the diameter of the duct and f_{max} is the maximum input frequency. If the duct diameter is smaller than that suggested by equation 5.1, higher order modes might exist close to the surface of the waveguide effecting the planar character of the input signal. This can have strong implications on the educed impedance spectra (see chapter 2 and section 5.2).

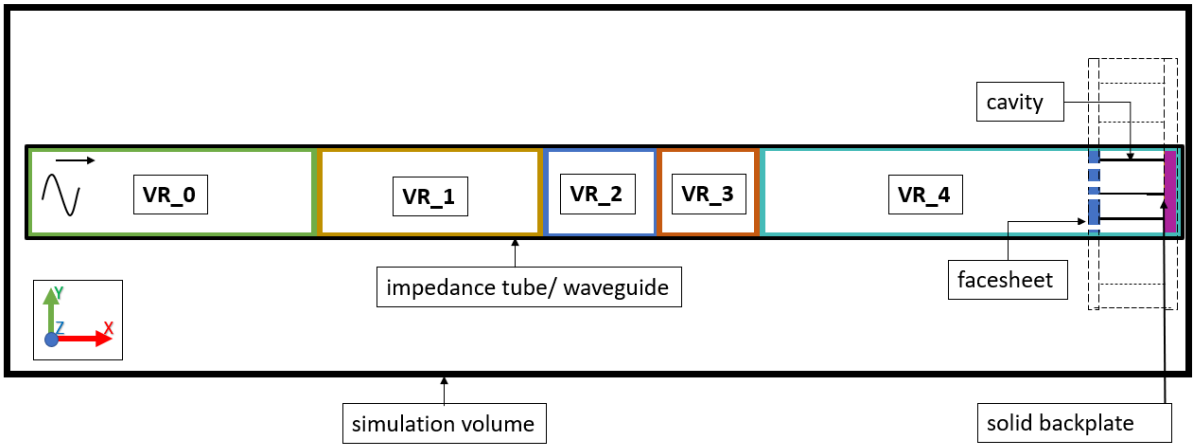

Figure 5.2: 2D schematic of the Digital Normal Impedance Tube setup

Honeycomb Liner Geometry

In the current chapter, the geometry of the honeycomb liner corresponds to the 6.4% porosity (facesheet porosity) liner as used by Jones et al. [31]. This liner consists of a hollow honeycomb shaped cavity, backed by a solid plate at one end and a perforated facesheet at the other end as seen from the deconstructed view of the 6.4% porosity liner in figure 5.3. This liner cavity has a depth of 38.1 mm with each side equal to 5.69 mm. The facesheet on the other hand, has a thickness of 0.64 mm with the perforation diameter equal to 0.99 mm. Furthermore, the distance between two consecutive orifices is 3.29 mm as shown in figure 5.4. For the purpose of numerical simulations, numerous 6.4% porosity liner shown in figure 5.3 are arranged in a 3D array pattern, such that multiple liners lie within the bounds of the impedance tube.as seen in the 2D schematic in figure 5.2.

Variable Resolution (VR) Strategy

Having a VR strategy means to tactically choose the grid resolution within the computational domain such that the domain is neither over nor under discretized. This strategy not only helps in appropriate discretization of the flow-field but it also prevents over-discretization, thus saving on the simulation

time. For the simulations in the current chapter, nine different cylindrical VR regions are chosen, with VR_8 being the region with smallest voxels size and VR_0 being the region with the largest one. These regions are defined such that the voxel size increases linearly by a factor of two from one resolution scale to the next. For e.g. voxel size in VR_7 is twice of that in VR_8 and so on.

Figure 5.5 shows that the VR regions VR_5 to VR_8 are located in the vicinity of the liner facesheet. The liner orifice is a region of high flow gradient and thus, having high resolution VR regions in its vicinity is justified. For other regions, specifically for VR_4, the grid size should be small enough to accurately capture the incoming acoustic signal. Furthermore, VR_4 is kept long enough to fit the longest wavelength of the input signal. Other VR regions, i.e. from VR_0 to VR_3 cover the rest of the waveguide as seen in figure 5.2. Moreover, it should be noted that each VR region has an offset distance corresponding to 6 voxels assigned to it such that the transition from one resolution scale to another is smooth.

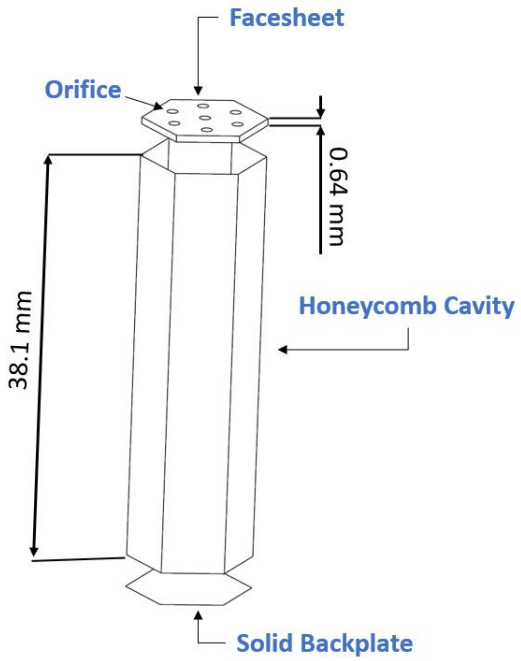

Figure 5.3: Deconstructed view of a single 6.4% porosity liner

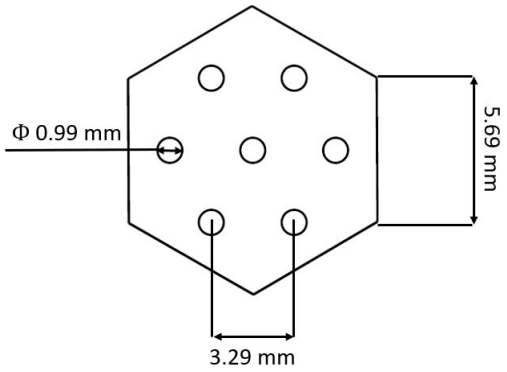

Figure 5.4: Dimensions of the perforated facesheet

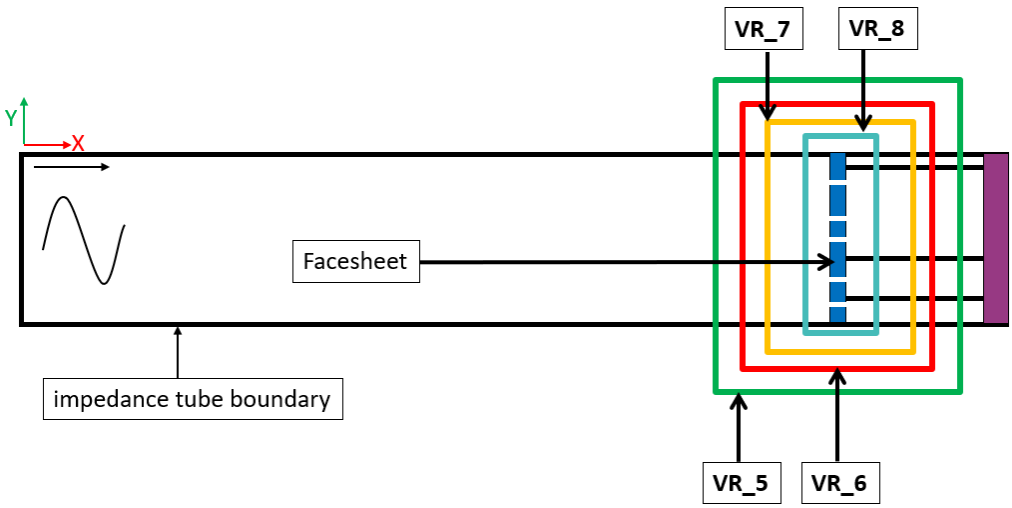

Figure 5.5: Near-facesheet Variable Resolution regions

Fluid/ Solid region

Defining fluid/ solid region enables the discretizer to identify the regions where the fluid voxels and where the surfels have to be created. While discretizing, the solver first fills the entire domain with voxels from the coarsest VR region, i.e. VR_0 in the current case. Subsequently, the finer VR regions are created and the voxels within the user defined solid regions are replaced with surfels over the solid surfaces. In this chapter, the waveguide boundary, the liner facesheet, cavity walls and the backplate have been chosen as *solids*. The simulation volume on the other hand (see figure 5.2) has been defined as a *fluid* region.

Boundary Condition

For the simulations in the current chapter, two different wall boundary conditions are used, namely the *standard wall boundary* and the *frictionless wall boundary* condition. The *standard wall boundary* condition simulates a regular passive wall with a no-slip boundary such that a boundary layer develops naturally over it. The surface roughness of the standard wall is kept as 0. Alternatively, the *frictionless boundary condition* simulates an ”ideal” wall where the fluid particles slip past the wall boundary. It should also be noted that an adiabatic wall condition is enforced with both the boundary conditions to ensure that no heat is transferred through the walls. In the current numerical setup, the entire liner geometry including the liner facesheet, cavity walls and the solid backplate have been defined as *standard walls*. On the other hand, the duct/waveguide has been defined as a *frictionless wall*. Having a boundary layer on the walls of the waveguide might effect the planarity of the acoustic signal along with leading to undesired dissipation of the energy of the input acoustic signal. Thus, the use of a frictionless wall boundary condition for the waveguide is justified.

Simulation Time

Like all CFD solvers, PowerFLOW® is also effected by the problem of initial transient, thus, it is all the more important to select an appropriate simulation duration. In the current verification study, the simulation duration is equal to the time period of the minimum input frequency (f_{min}). Thus, it should be ensured that the minimum frequency is much lower than the frequency range of interest (ROI) so that multiple cycles can be simulated within the ROI. For most cases in the current study, f_{min} is equal to 50 Hz which corresponds to a simulation time of 0.02 sec. This allows multiple cycles within the ROI of 1 kHz - 3 kHz which should be appropriate to overcome the initial transient.

5.2. Impedance Eduction

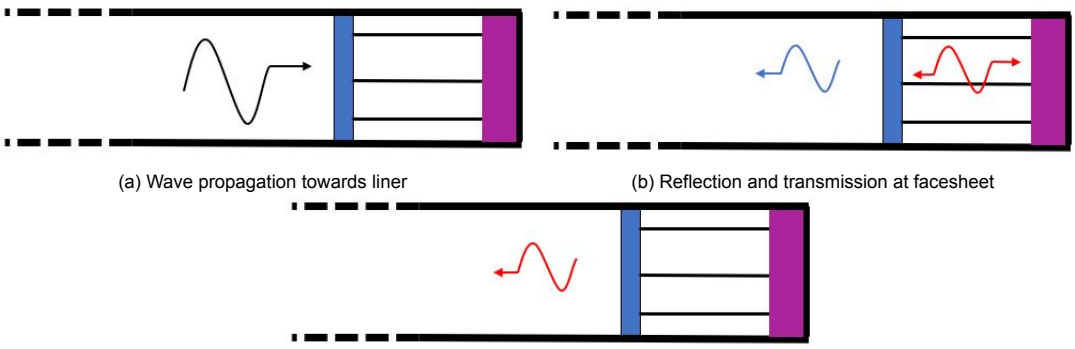

(a) Wave propagation towards liner

(b) Reflection and transmission at facesheet

(c) Complete reflection of the transmitted wave

Figure 5.6: Signal interaction with acoustic liner

The acoustic mechanism within the DNIT (figure 5.2) is rather simple and can be explained through a three-step procedure as shown in figure 5.6. Firstly the input wave propagates towards the liner where

it interacts with the liner facesheet. This interaction causes a part of the wave to be reflected and part to be attenuated as it is transmitted downstream of the facesheet as shown in figure 5.6(b). Inside the honeycomb cavity, the wave is periodically attenuated and transmitted as it moves upstream of the waveguide, after reflection from the backplate. Finally, the initial acoustic wave is completely reflected after being attenuated by the liner. This interaction can be recorded by placing probes at specific locations within the waveguide, and the recorded signal can be subsequently processed to educe the liner impedance.

In the current section, the procedure to educe the acoustic impedance is presented followed by a brief discussion on the selection of probe location.

5.2.1. Impedance Eduction Procedure

The impedance eduction approach employed in the present study is based on Habibi & Mongeau [24]. This method relies on obtaining pressure and velocity readings at several probe locations upstream of the liner. It is perhaps interesting to note that contrary to the definition of acoustic impedance (section 1.3), its calculation in the current method is not based on determining the complex acoustic pressure and complex acoustic velocity at the liner surface. Rather, it is calculated/ educed based on the parameters obtained at different probe locations within the waveguide. Thus, the term 'eduction' shows the manner in which impedance is derived.

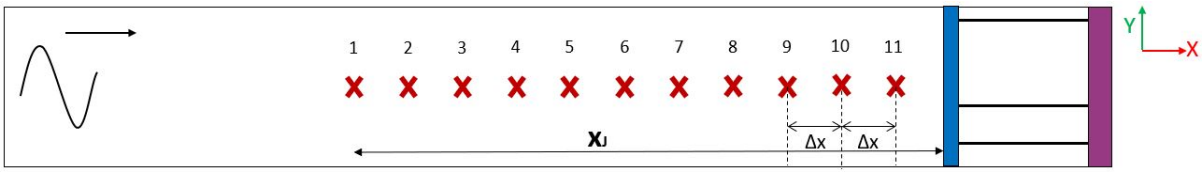

Figure 5.7: Schematic of the numerical waveguide with virtual probes (*not to scale*)

The impedance eduction process is initiated by extracting velocity and pressure variation from eleven virtual probes that are separated by a distance of Δx from each other, as indicated schematically in figure 5.7. Assuming that only plane waves propagates in the waveguide, the complex acoustic pressure ($\hat{p}^j$) at a microphone location j is expressed as follows,

$$\hat{p}^j = \hat{p}_i^j e^{-ikx_j} + \hat{p}_r^j e^{ikx_j} \tag{5.2}$$

where, k is the acoustic wavenumber, x_j is the probe location relative to the acoustic liner, and $\hat{p}_i^j$ and $\hat{p}_r^j$ are the complex acoustic pressures of the incident and reflected wave respectively (see figure 5.6). The complex acoustic velocity $\hat{v}_j$ at a microphone location j can be related to $\hat{p}_i^j$ and $\hat{p}_r^j$ based on the linearised Euler equation which is shown below,

$$\frac{\partial v}{\partial t} = -\frac{1}{\rho}\frac{\partial p}{\partial x} \tag{5.3}$$

Differentiating equation 5.2 and then integrating equation 5.3 leads to the expression of the complex acoustic velocity at microphone j.

$$\hat{v}^j = \frac{1}{\rho c}[\hat{p}_i^j e^{-ikx_j} - \hat{p}_r^j e^{ikx_j}] \tag{5.4}$$

where ρ and c are the density of the fluid and the speed of sound in that fluid respectively. The variables $\hat{p}^j$ and $\hat{v}^j$ can be obtained by the Fourier transform of the pressure and velocity time series data obtained at a virtual probe location j. Thus with two unknowns, i.e. $\hat{p}_i^j$ and $\hat{p}_r^j$, in equation 5.2 and equation 5.4 makes the problem deterministic. The values of $\hat{p}_i^j$ and $\hat{p}_r^j$ can be further used to calculate the reflection factor R_e^j, which is a measure of the acoustic wave reflection at the liner surface.

$$R_e^j = \frac{\hat{p}_i^j}{\hat{p}_r^j} = \frac{\hat{p}^j - \rho c \hat{v}^j}{\hat{p}^j + \rho c \hat{v}^j} \cdot e^{-2\imath k x_j} \tag{5.5}$$

Thus the normal acoustic impedance of the liner can be computed by:

$$Z = \frac{1 + R_e^j}{1 - R_e^j} = R + \iota\chi \tag{5.6}$$

5.2.2. Selection of Probe Location

In the verification study, the instantaneous pressure and velocity readings are taken by 11 virtual probes located at different locations within the waveguide as represented by **x** in figure 5.7. The probes are numbered from 1 to 11, with probe 11 being the closest to the liner and probe 1 being the farthest. While selecting the location of the probe closest to the liner, it should be ensured that it is at a considerable distance away the liner so that only the acoustic pressure is recorded and the reading is not effected by the near/ in-orifice hydrodynamics. The subsequent liners are placed at a uniform distance Δx from each other. Jones & Parrot [35] have suggest that uniform microphone spacing might lead to inaccurate results at certain frequencies. They state that at certain frequencies, the probes might be located near the acoustic nodes and thus, they would sense very small amplitudes of the same order as the numerical diffusion. However, this is not a concern for the current study as the chosen value of Δx is small enough to incorporate multiple probes, i.e more than 3 virtual probes, even within the smallest wavelength of the broadband input signal.

In the current study the probe location is given by the following relation:

$$x_n = x_{11} - \Delta x \cdot (n - 11) \quad [m] \tag{5.7}$$

where x_n represents the location of the nth probe and n ranges from 1 to 10. x_{11} is the location of 11^{th} probe from the liner facesheet and its value in the current study is -0.0228833 m. Furthermore, a value of 0.02595 m is assigned to Δx

5.3. Input Conditions

Variable	Value	Unit
Signal Type	Broadband	[-]
Minimum Frequency	50	[Hz]
Maximum Frequency	5000	[Hz]
OASPL	130	[dB]
Simulation Time	0.02	[sec]

Table 5.1: Input Conditions for PowerFLOW®

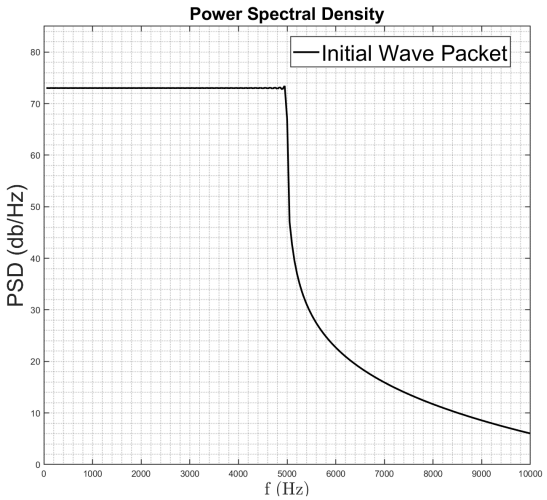

Figure 5.8: PSD of initial wave packet

The input conditions for the simulations conducted in the current chapter are summarized in table 5.2. The acoustic signal used for the simulations is of a broadband type, with a minimum input frequency of 50 Hz and a maximum frequency of 5000 Hz. The broadband signal is characterised by a flat spectrum upto the prescribed maximum frequency as seen from the PSD curve in figure 5.8. It is seen that the signal has a constant PSD value of 73 db/Hz over the range of 50-5000 Hz. After 5000 Hz, the PSD drops suddenly showing that the energy content of the acoustic wave is concentrated within the input bandwidth. Moreover, the Overall Sound Pressure Level (OASPL) of the input acoustic signal is chosen as 130 dB. While the SPL at an individual frequency would be lower than 130 dB, it

is wise to use the OASPL value to discriminate between the linear and the non-linear liner response [32]. Furthermore, the run-time of the simulations is kept at 0.02 sec, which is in accordance with the requirements mentioned in section 5.1.

5.4. Resolution Study

Before analysing the efficacy of the computational setup to reproduce the acoustic effects of the liner, a small resolution study is conducted. This study is necessary to ascertain the independence of the simulation results from the choice of the grid. Three different grids, referred as coarse, medium and fine with a resolution of N = 7, 14 and 27 voxels respectively have been analysed in the current section. Here N corresponds to the number of voxels across the orifice thickness (t_f). The corresponding grid size in terms of the Fine Equivalent Voxels (FEV), which is the weighted sum of voxels in the different VR region is 3.476754x10^6, 13.654833x10^6 and 54.262657x10^6 respectively. A summary of grids used in the resolution study is given in table 5.3. For all aforementioned grids the same VR strategy and input conditions have been used.

No.	Grid-Type	Smallest Voxel [mm]	Timestep [μsec]	N [voxels]	FEV [voxels]
1	Coarse	0.09375	0.13750	07	3,476,754
2	Medium	0.046875	0.06877	14	13,654,833
3	Fine	0.0234375	0.03566	27	54,262,657

Table 5.2: Summary of the grids used for the grid resolution study

The quality of the grids can be analysed by looking at the normalised acoustic resistance and the normalised acoustic reactance curves averaged over all the probe locations shown in figure 5.7. The impedance values have been normalised by the characteristic impedance of air i.e. ρc_∞. In the figure 5.9, the solid line represents the mean value, while the shaded region represents the scatter. The results indicate that as the grid resolution increases, the value of both resistance and reactance decreases. The decrease in acoustic resistance with the increase in resolution is also observed by Mann et al. [44], who attributed this trend to a higher numerical dissipation at lower values of N in the vicinity of the liner facesheet. Moreover, the results with the coarse grid exhibits a fluctuating trend at higher frequencies. This is probably caused by the nature of the windowing function used while post-processing the simulation data. However, this should not be of concern as these fluctuations are negligible for the results obtained with higher resolution.

From figure 5.9(a), it can be seen that the value of acoustic resistance decreases drastically from a coarse grid to a medium grid, with an average reduction of 30% over the entire range of frequency, while the decrease in acoustic reactance is about 10%. From a medium to fine grid however, the average decrease in the value of acoustic resistance is of about 12%. On the other hand, the value of acoustic reactance decreases by 5%. Clearly, the results with the coarse grid are not converged. Moreover, a change of 12% in acoustic resistance from medium to fine grid is still quite significant and thus, the simulation results are considered to be converged for the fine grid. Furthermore, it should be noted that the FEV for a fine grid is of the order of 10^{08} and any further increase in the resolution will increase the FEV and consequently the required computational resources considerably. Thus, the use of fine grid with N = 27 voxels is justified.

Previously Mann et al. [44] conducted a numerical study of a honeycomb liner using the LBM-VLES approach, and observed grid convergence for the smallest voxel size of 0.2 mm unlike in the current case, where the convergence is observed for 0.02343 mm. However, Mann et al. [44] used a facesheet of 3 mm thickness which is different from the 0.64 mm thick facesheet used in the current thesis which explains the difference in the smallest voxel size. Manjunath et al. [43] studied the same liner as in the current thesis, and observed convergence with a similar VR strategy and for a smallest voxel size of 0.023 mm. This result further justifies the use of 'fine grid' in the current thesis,

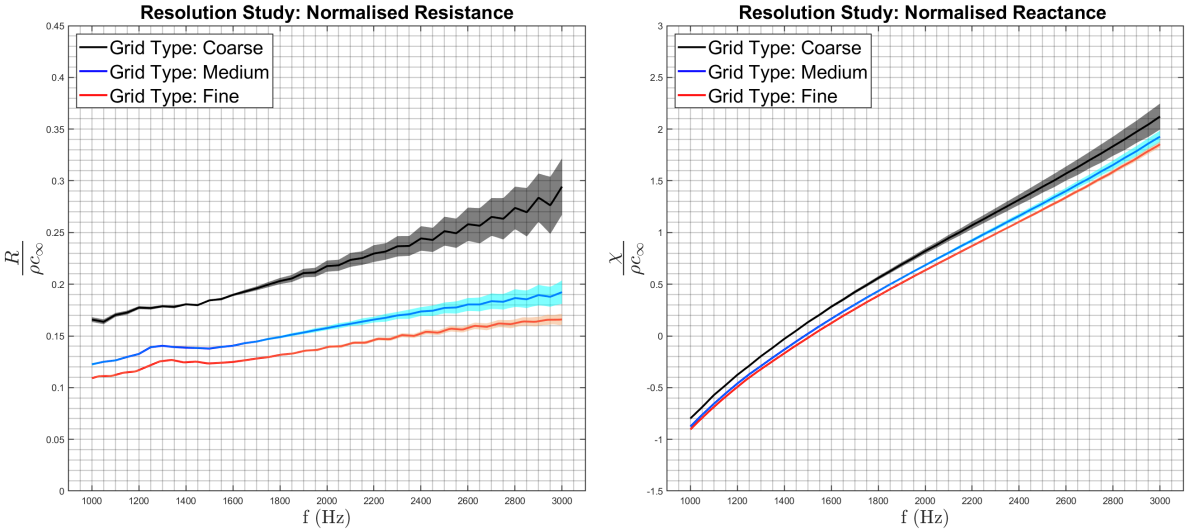

(a) Normalised Resistance

(b) Normalised Reactance

Figure 5.9: Impedance spectra from the grid resolution study

5.5. Comparison with Experimental and Analytical results

In the previous section, a convergence study has been conducted to establish the resolution for which the simulation results are independent of the input grid. The next step is to compare the simulation results with the experimental and analytical models.

In figure 5.10 and figure 5.11, the educed impedance from the simulations is compared with the reference experimental results. In the figures, NIT stands for Normal Impedance Tube setup. This setup is similar to the DNIT setup used in the current thesis. Moreover, 6.4% and 8.7% denotes the porosity of the liner used in the respective experimental study. On the other hand, GIT stands for Grazing Impedance Tube. The setup of the grazing impedance tube is similar to that shown in figure 2.5. In this setup, the acoustic signal grazes tangentially over the liner, unlike the normal acoustic incidence for the DNIT setup used in the current thesis. TB and $95M$ denotes that the two set of experimental results have been obtained using different impedance eduction techniques, namely the traversing bar and the fixed microphone respectively. For a detailed information of the experimental setups used for comparison in the current section, the reader is reffered to [31]. In all the aforementioned experimental studies, the geometric specifications of the liner is same as that mentioned in section 6.2, except for the NIT - 8.7% case, where the porosity of the facesheet is changed from 6.4% to 8.7%. Moreover, all the experiments have been conducted with a tonal input and not a broadband input like in the current section. For liner operating in a linear regime, this difference in the nature of the input signal should not be of concern [32].

Ideally, the simulation results should match with the NIT (6.4%) values as the liner geometries are identical and the setups are similar. However, as seen from figure 5.10(a), the acoustic resistance is underpredicted for the entire range of frequencies with respect to the NIT (6.4%) results, with a maximum difference of about $\approx$ 50% in the vicinity of the liners resonance frequency i.e. f $\approx$ 1.5 kHz (at resonance, χ = 0). Similar observations can be made on comparing the simulations results with that from the experiments conducted in the GIT. However, a clear difference between the GIT and NIT resistance values is observed at f = 1.5 kHz, which is close to the resonance frequency of the liner. The GIT-TB experiment predicts a resistance peak at this frequency, which is not seen for the NIT(6.4%) case. The simulation results shows a small peak at f $\approx$1.5 kHz which might be caused due to the resonance effect, however this trend is subtle when compared to the results from the GIT experiment. At f = 3 kHz, Jones et al. [31] mentioned about an increase in the experimental uncertainties in the GIT results, however it is not enough to account for the observed discrepancies. This statement is also confirmed by Zhang & Bodony [74].

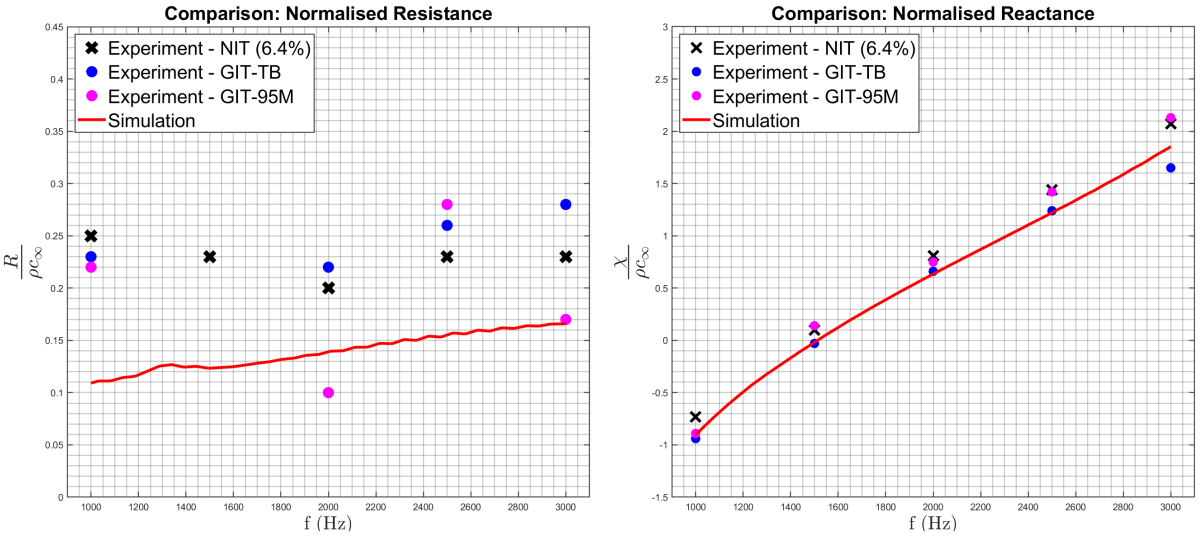

(a) Normalised Resistance (b) Normalised Reactance

Figure 5.10: Comparison of simulation result with the experimental results

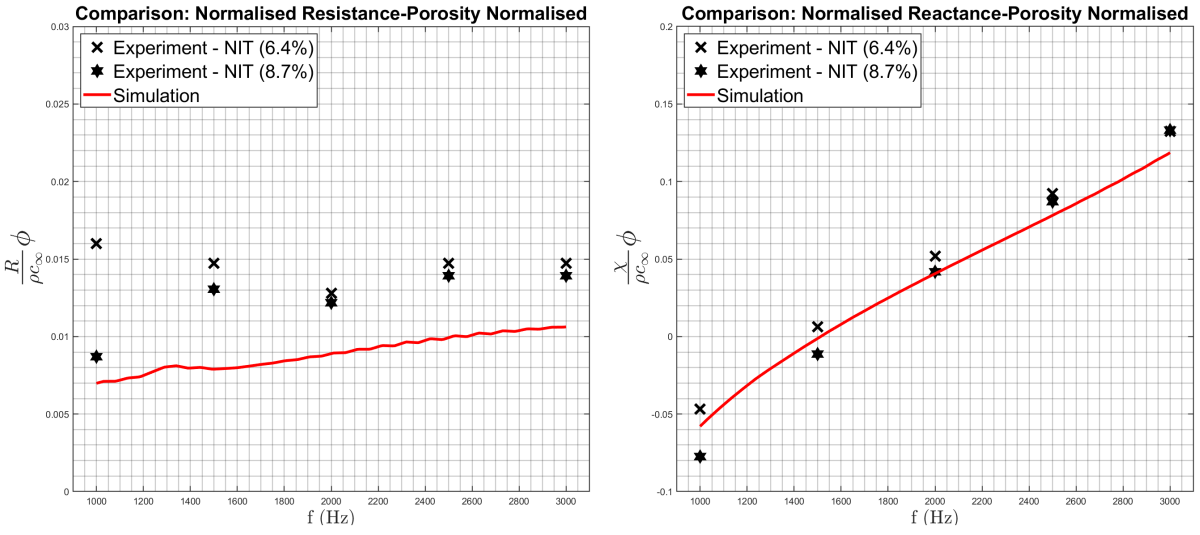

(a) Normalised Resistance (b) Normalised Reactance

Figure 5.11: Comparison of simulation result with the porosity normalised experimental results

Moreover, from the porosity normalised plots in figure 5.11 it can be seen that the current simulations underpredict the normalised resistance of the 8.7% liner porosity. According to Jones et al. [30], the acoustic resistance decreases with the increase in the liner porosity, primarily due to a decrease in the viscous and inertial effects in the vicinity of the liner orifice (see section 2.2). Considering the fact that the simulations also underpredict the NIT (8.7%) results, clearly suggests that the simulations are not able to capture the aforementioned effects properly.

Differences in reactance prediction w.r.t the NIT(6.4%) results are typically smaller than the resistance results as seen in figure 5.10(b). It is seen that the reactance from the simulation matches the GIT-TB results slightly better than the NIT(6.4%) for frequencies between 1 kHz $< f <$ 2.5 kHz. This is also supported by the fact that for the NIT(6.4%) results, the resonance (i.e. f at $\chi = 0$) is observed at f ≈1.5 kHz, while that for the simulation and GIT-TB is observed at f ≈1.6 KHz.

In figure 5.12, the simulations results are compared against the analytical models and few of the numerical results present in the state of the art. In the figure, model A represents the Melling's model while

model B represents the Motsinger's model. For a detailed information of these models, the reader is referred to section 2.2. Furthermore, the figure also includes the results from the DNS study of Zhang & Bodony [74] and the LBM-VLES study from Manjunath et al. [43]. The acoustic resistance educed from the simulations underestimate the values predicted by model A over the entire ROI. However, it can be seen that for f > 1.5 kHz the values from model A and the simulations tends to converge towards each other other. Results from model B also show similar trends at $f \leq$ 1.5 kHz, however at higher frequencies the values of acoustic resistance are even lower than that predicted by the simulations. Elnady & Boden [21] mention that the viscous term used in model B (see equation 2.14) is not applicable at higher frequencies such as those under investigation in the current study. This could explain the observed trends.

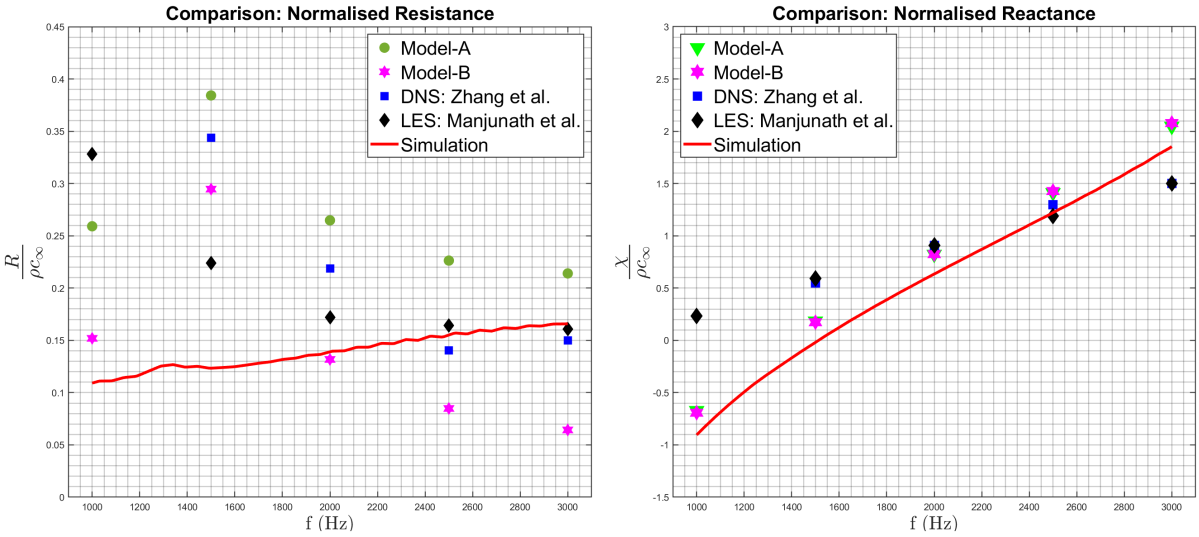

(a) Normalised Resistance (b) Normalised Reactance

Figure 5.12: Comparison of simulation result with the analytical results

Furthermore, at f = 2.5 and 3 kHz, the resistance value from the DNS and the LES study shows good agreement with the simulation results. However, the former exhibits completely different trend than the simulation results and thus the resistance trend observed at f > 2 kHz could be a mere coincidence. Anyways, it can be said that the underprediction (w.r.t experimental results) at f > 2 kHz is uniform across the different numerical studies mentioned here. Zhang & Bodony [74] were not able to offer an explanation to this underprediction and have left it as an open question. Moreover, contrary to the impedance eduction method used in the current thesis, both Zhang & Bodony [74] and Manjunath et al. [43] used the Dean's method (see section 2.2.2) for educing acoustic impedance. This difference might lead to some discrepancies in the results, however, not enough to account for the trends observed here.

5.6. Diagnosis of Discrepancy

The results presented in the previous section show that simulations conducted with the honeycomb liner geometry underpredict the value of acoustic impedance. The following sections seeks to investigate the reason for the aforementioned trends by analysing the influence of the user-defined input, such as the input OASPL, on the impedance results.

5.6.1. Simulations without Liner Geometry

In a case where the user-defined boundary conditions and the fluid/ solid regions are not defined properly, spurious phenomenon occurring within the computational setup can effect the educed impedance spectra. For e.g., if the *frictionless wall-boundary conditions* is not applied properly at the walls of the waveguide, then additional absorption of the input acoustic wave can occur due to viscous dissipation. Thus, to ensure that such spurious effects are absent in the current setup, numerical simulations are conducted without the geometry of the honeycomb liner, in the current section. Figure 5.13 shows the

narrow band spectrum plotted at a bandwidth of 100 Hz for the signals recorded at microphone location 2 and 11 (see figure 5.7). At mic 2 and mic 11, the computed OASPL values are 131.22 dB and 130.99 dB respectively, which is approximately equal to the input OASPL of 130 dB. The fact that the input OASPL is recovered from the simulation, indicates the absence of any spurious losses within the DNIT setup, confirming that the acoustic attenuation is caused solely by the honeycomb liner.

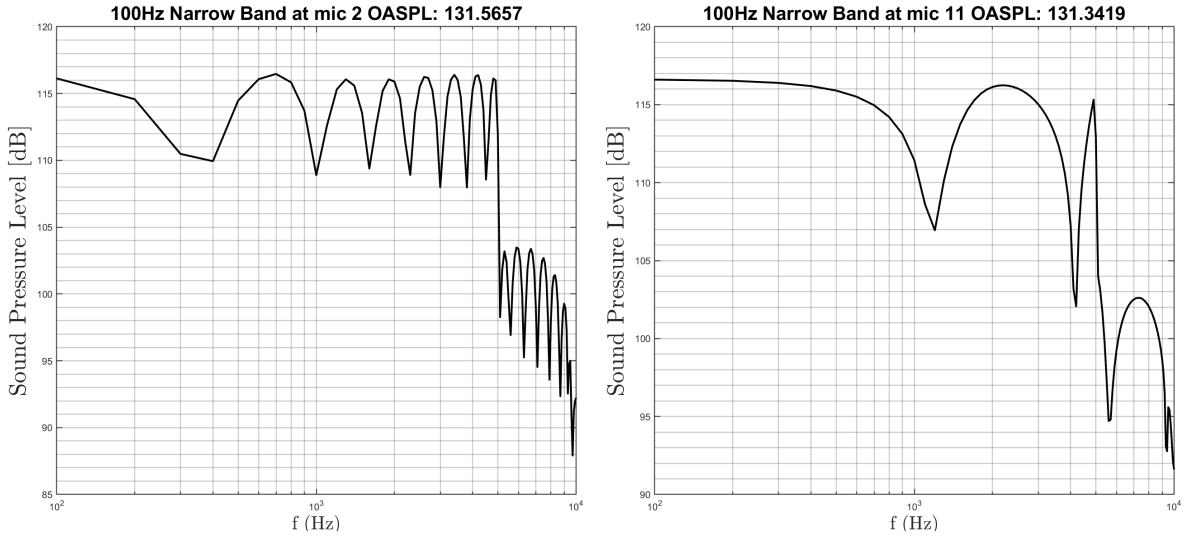

(a) Location: Microphone 2

(b) Location: Microphone 11

Figure 5.13: SPL recorded at different microphone locations

5.6.2. Effect of Waveguide Diameter

The impedance eduction method employed in the current study assumes that each orifice present within the waveguide attenuates the acoustic signal equally and thus, it naturally averages the acoustic impedance over the surface of the liner facesheet. Considering that the educed impedance is an average value, it is necessary to have adequate number of orifices within the waveguide. In the current section, it is hypothesized that increasing the waveguide diameter would increase the number of orifices within the waveguide, and thus, a more accurate ”average” impedance spectra can be educed. Thus, numerical simulations have been conducted with different duct/ waveguide diameters in the current section. Furthermore, it should be noted that the simulations in the current section are conducted with a medium grid. This decision was taken based on the available computational resources. Table 5.4 provides a summary of the cases evaluated in the current section.

No.	Grid-Type	Duct Diameter (m)
1	Medium	0.0468
2	Medium	0.0501
3	Medium	0.0573

Table 5.3: Summary of the cases evaluated in the current section

From figure 5.14, hardly any difference is observed in the reactance values with the change in duct diameter. For the normalised resistance however, an average increase of 13% is seen between duct diameters of 0.0468 m and 0.0573 m. This result suggests that for small duct diameters, the number of orifices within the waveguide might not be enough to provide accurate impedance values. However, the simulation result with the increased duct diameter still underpredict the reference experimental results. Thus, although the effect of duct diameter is important while evaluating the impedance results, they don’t explain the trends observed in section 5.5.

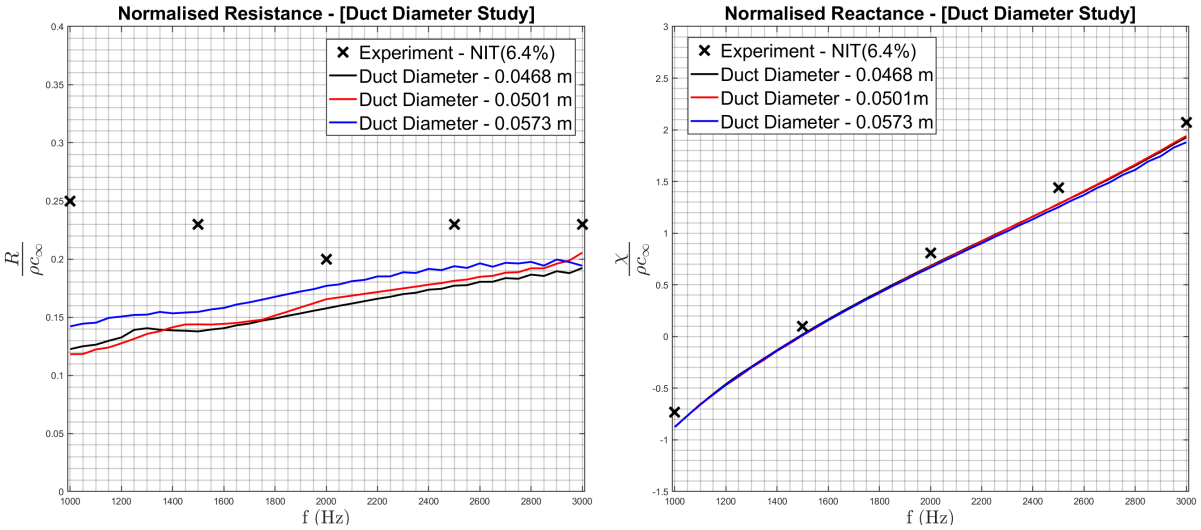

(a) Normalised Resistance (b) Normalised Reactance

Figure 5.14: Effect of duct diameter on acoustic impedance

5.6.3. Effect of Impedance Eduction Method

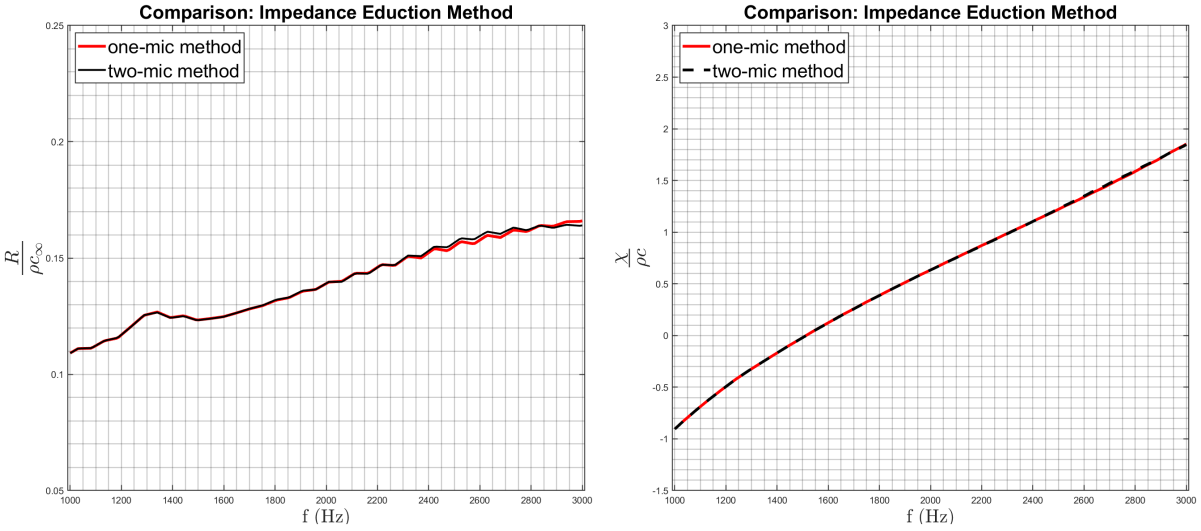

(a) Normalised Resistance (b) Normalised Reactance

Figure 5.15: Comparison of impedance eduction method

Experimental studies conducted by Jones et al. [31] and Watson et al. [29] have shown that the impedance results can be dependent on the way acoustic impedance is educed. This can be already seen through figure 5.10, where the GIT-TB and GIT-95M results are as different as 50% from each other at certain frequencies. Thus, to ascertain that the simulation results are independent of the choice of impedance eduction method, the impedance from the one-mic and two-mic method (see section 2.2.2) are compared in figure 5.15.

It can be seen that both the acoustic resistance and the acoustic reactance are identical for both methods at each frequency within the ROI. Thus, it is highly unlikely that the discrepancies observed in section 5.5 are caused by the choice of impedance eduction method.

5.6.4. Effect of Input Overall Sound Pressure Level

The discussion presented in section 2.2.3 shows that with an increase in the input OASPL the in-orifice velocity increases which can consequently increase the acoustic resistance. However, below a certain threshold value, the acoustic resistance is independent of any changes in the OASPL. This regime where any increase in the in-orifice velocity doesn't effect the resistance offered by the liner is said to be linear [74] and thus, the non-linear hydrodynamic phenomenon such as the orifice vortex shedding are absent. To ascertain that correct impedance trends are observed from the simulations conducted with the setup shown in figure 5.2, numerical simulations are conducted for different OASPL values in the current section.

Figure 5.16 shows the variation of normalised acoustic resistance and reactance with the change in input OASPL. From figure 5.16(a), a maximum change of 4% is observed between the acoustic resistance obtained for OASPL of 110 dB and 120 dB, compared to a 20% change in the resistance values when the OASPL is increased to 130 dB from 120 dB. This shows that for 110 and 120 dB, the resistance value is largely independent from the in-orifice velocity. On the other hand, the curve at 130 dB suggests a dependence on the in-orifice velocity and indicates that the liner might be operating in the non-linear regime. Conversely, the acoustic reactance is independent of the input OASPL values as seen in figure 5.16(b).

Manjunath et al. [43] has observed similar trends for the acoustic impedance with the change in input SPL through their numerical study. This confirms that the simulations conducted in the current thesis show correct trends with the change in input OASPL.

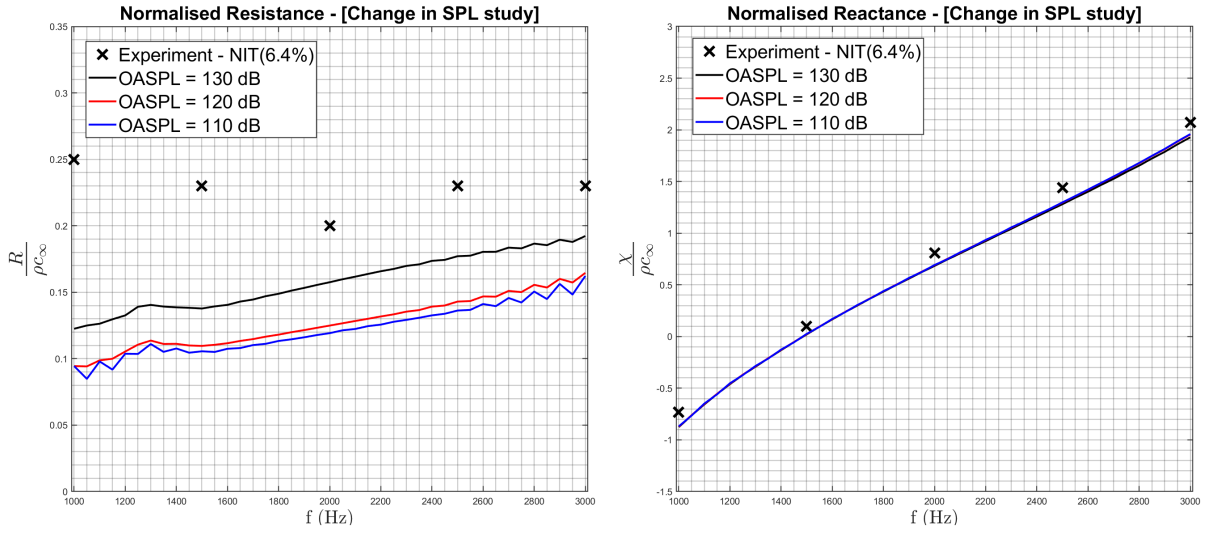

(a) Normalised Resistance

(b) Normalised Reactance

Figure 5.16: Effect of input SPL on acoustic impedance

5.6.5. Comparison between Broadband and Tonal Excitation

As mentioned earlier, one of the major differences between the simulations conducted in the current study and the reference experimental/ numerical results is in the source of the input signal. In the current study the acoustic liner is analysed for a broadband signal, while the reference studies uses a tonal source. Motsinger et al. [46] have mentioned that the acoustic resistance is a function of the r.m.s of the in-orifice velocity contrary to the velocity at a single frequency. With this assumption in mind, replacing the tonal source with a broadband one should be justified.

The study in the current section seeks to verify the efficacy of the above mentioned concept for the Jones 6.4% porosity liner. The performance of this liner is analysed under tonal and broadband excitation at an OASPL of 110 dB and 130 dB. In this section, the input signals are generated such that

the OASPL for both these excitation remains equal. The only difference then, is that the energy for the tonal input is concentrated at a single frequency as seen in figure 5.17, while that for the broadband input is distributed over the input bandwidth (see figure 5.8).

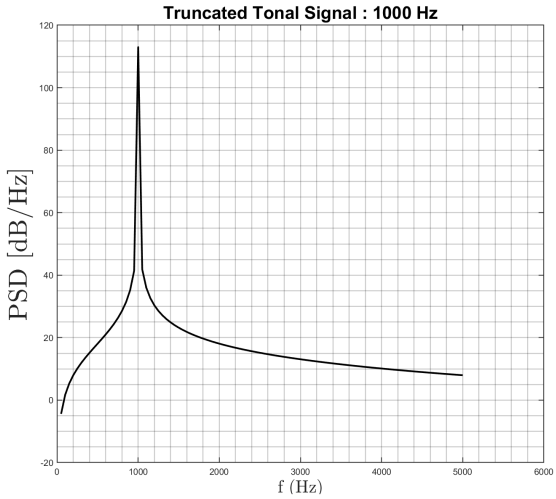

Figure 5.17: PSD of the truncated tone at f = 1 kHz

Comparison of near-orifice flow-field

Figure 5.18 and figure 5.19 compares the near-orifice flow-field for the tonal and the broadband input at an OASPL of 110 dB and 130 dB respectively, for a maximum inflow phase of $\theta = \pi/2$. At 110 dB, the flow-field for the two cases are quite similar, without any trace of flow non-linearities. Conversely, that at 130 dB are quite distinct from each other. For the tonal case, two distinct low pressure regions are observed downstream of the orifice as seen from figure 5.19. These low pressure regions represents the vorticity being shed from the edge of the liner orifice orifice. The presence of vortices shows that the liner is operating in the non-linear regime. On the other hand, such flow non-linearities are not observed for the broadband source as seen in figure 5.19(a).

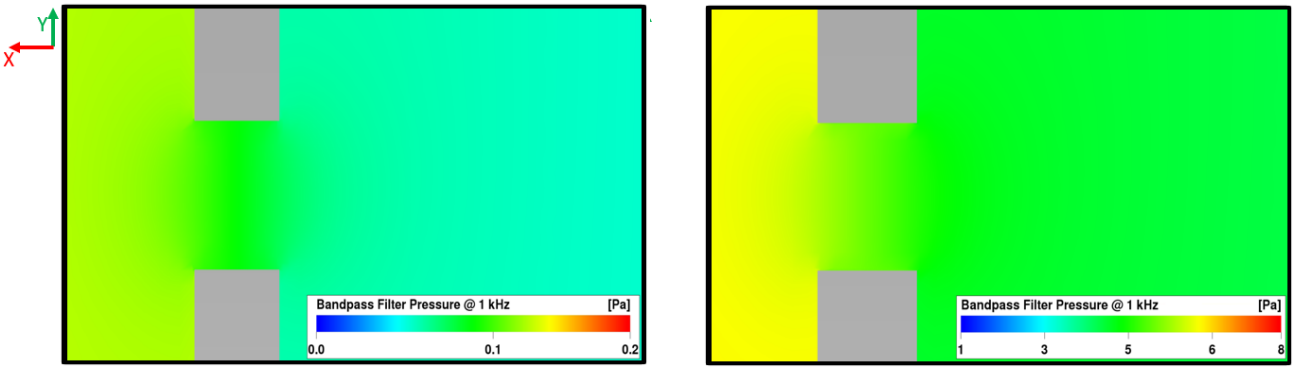

(a) Broadband excitation

(b) Tonal excitation

Figure 5.18: Near-orifice pressure field for f = 1 kHz and OASPL = 110dB (Phase (θ) = $\pi/2$)

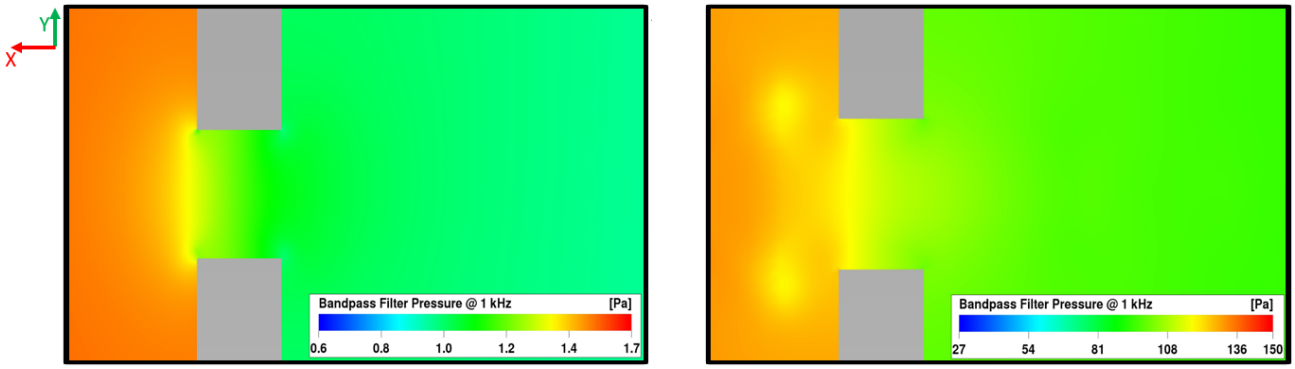

(a) Broadband excitation (b) Tonal excitation

Figure 5.19: Near-orifice pressure field for f = 1 kHz and OASPL = 130dB (Phase (θ) = π/2)

Comparison of impedance spectra

Figure 5.20 shows that the resistance spectra for the 110 dB tonal case compares favourably with the corresponding broadband signal, where the broadband values at f = 1 kHz and f = 2 kHz are only 6% and 9% different from the tonal ones respectively. This result shows that the acoustic resistance at 110 dB is independent of the in-orifice velocity and thus, the broadband and the tonal signal can be used interchangeably for the current liner. However, it should be noted that this statement stands true only at 1 kHz and 2 kHz as comparison at other frequencies were not made in the current study.

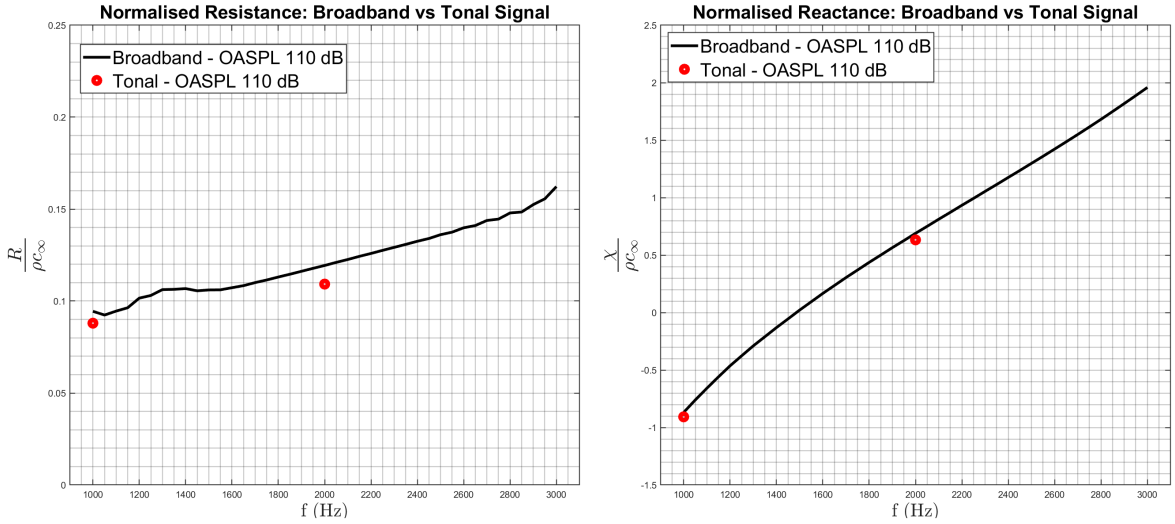

(a) Normalised Resistance (b) Normalised Reactance

Figure 5.20: Impedance comparison for tonal vs broadband excitation at OASPL = 110 dB

The same conclusions cannot be made at 130 dB, as the resistance for the broadband input is considerably lower than that obtained with the tonal source. This underprediction is maximum at the resonance frequency, i.e. at f = 1.5 kHz, where a difference of 60% is observed. This discrepancy should be expected as the broadband case is unable to predict the vortex shedding from the edge of the orifice as seen from figure 5.18. Thus, the contribution of the flow non-linearities to acoustic resistance is bound to be lower for the broadband case. Although the flow-field data is available at f = 1 kHz only, it is believed that this explanation regarding underprediction of non-linearities should hold true at other frequencies as well.

More interestingly, the resistance with tonal excitation shows a much better prediction of the experimental results, which are also computed with tonal input. Thus, it can be concluded that the discrepancies observed in section 5.5, were caused by the difference in the nature of acoustic excitation between the LB simulations and the experiment. This analysis clearly demonstrates that the nature of the acoustic

excitation must be take into account before analysing a liner. Previously, Jones et al. [32] analysed a honeycomb liner for tonal and broadband inputs at 120 dB and 140 dB, and also observed discrepancies in the resistance spectra for conditions where flow non-linearities were dominant. This result supports the conclusion made in the current section.

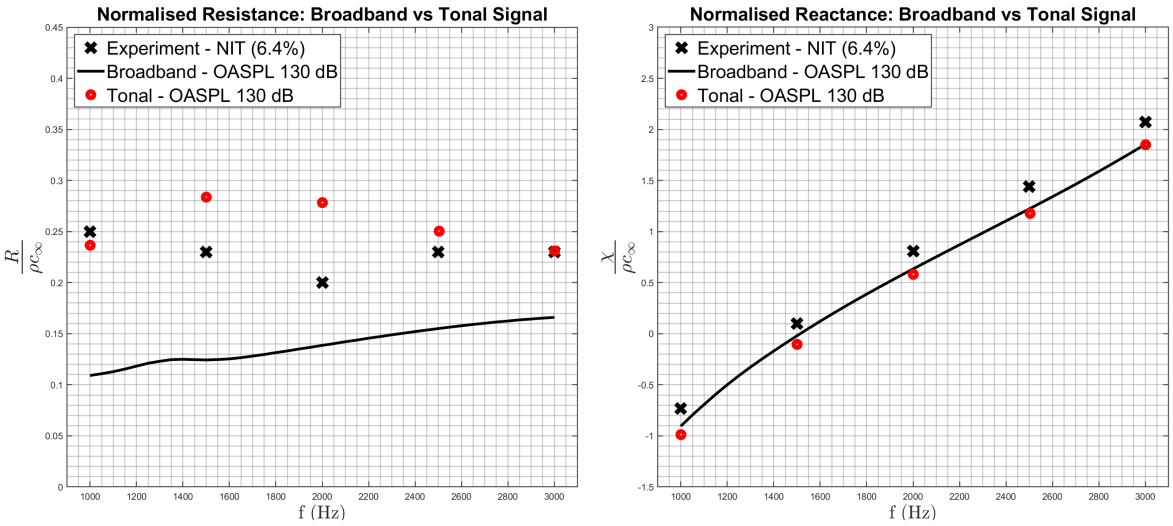

(a) Normalised Resistance

(b) Normalised Reactance

Figure 5.21: Impedance comparison for tonal vs broadband excitation at OASPL = 130 dB

6

Acoustic Porous Medium-CFD Setup Verification

In the second step of the thesis, a verification study is carried out to ascertain the use of the APM-CFD numerical setup. The general methodology of the verification process is given in figure 6.1. In this verification process, the APM is used to mimic the acoustic effects of the CT73 ceramic tubular liner (see figure 3.6). The results from the simulation are compared to the experimental study of Jones et al. [50] and the analytical model of Hersh & Walker [25]. Once the acoustic effects of the CT73 are successfully reproduced with the current numerical setup, it can be extended to model the honeycomb liner given in chapter 5.

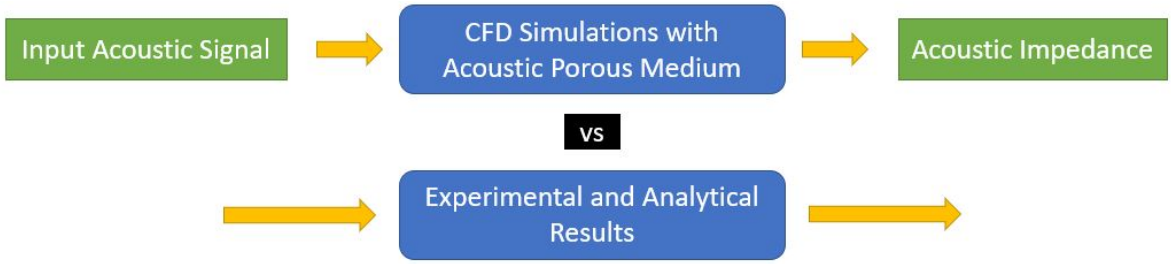

Figure 6.1: Illustration of the methodology employed in Acoustic Porous Medium-CFD verification

This chapter starts with a description of the Hersh & Walker model in section 6.1, followed by a description of the CFD setup in section 6.2. Thereafter, a grid resolution study is given in section 6.4. Finally, the grid independent simulation results are compared with experimental and analytical values in section 6.5.

6.1. Hersh & Walker Analytical Model

The current section presents a discussion on the Hersh & Walker [25] analytical model which is used for the verification process of the APM-CFD numerical setup in the current thesis. Hersh & Walker presented an analytical expression for the impedance introduced by the presence of a porous media. Assuming a non-viscous linear regime with an isothermal approximation, the 1-D mass and momentum equations in the porous medium can be written as:

$$\frac{\partial \rho}{\partial t} = -\frac{\rho}{\phi}\frac{\partial v}{\partial x} \tag{6.1}$$

$$\frac{\rho}{\phi}\frac{\partial v}{\partial t} = -\frac{\partial p}{\partial x} - \sigma\frac{u}{\phi} \tag{6.2}$$

Assuming a simple harmonic solution, ρ, v, and p can be written as:

$$\hat{\rho} = \mathrm{e}^{\mathrm{i}\omega t}\rho(x) \quad \hat{v} = \mathrm{e}^{\mathrm{i}\omega t}v(x) \tag{6.3}$$

$$\hat{p} = \mathrm{e}^{\mathrm{i}\omega t}p(x) \quad \text{and} \quad p(x) = Ae^{-(\alpha+\mathrm{i}\beta)x} \tag{6.4}$$

where the term $\hat{p}$ and $\hat{v}$ can be obtained by solving the equation 6.1 and equation 6.2 along with the equation of state. In equation 6.2, the second term on the right side represents the Darcy's force term (see chapter 4) which governs the attenuation of the acoustic energy inside the porous medium. Moreover, it should be noted that for a special case of σ = 0 and ϕ = 1, equations 6.1 and 6.2 represent the sound propagation in the air.

With $\hat{p}$ and $\hat{u}$ known, the acoustic impedance induced by the porous medium can be written as [25]:

$$Z \equiv \frac{\hat{p}}{\hat{v}} = \frac{\rho_0\omega\beta + \alpha\sigma}{\phi\,(\alpha^2+\beta^2)} + \mathrm{i}\frac{\rho_0\omega\alpha + \beta\sigma}{\phi\,(\alpha^2+\beta^2)} \tag{6.5}$$

where α and β are the attenuation constant and the phase constant respectively, and are given by:

$$\alpha = \sqrt{\frac{1}{2}[\sqrt{r^2+j^2}-r]} \quad \text{and} \quad \beta = j/\sqrt{2}[\sqrt{r^2+j^2}-r] \tag{6.6}$$

On neglecting heat transfer within the porous material, r and j can be represented as,

$$r = \frac{\omega}{c_\infty} \quad \text{and} \quad j = \left(\frac{\omega}{c_\infty}\right)^2\left(\frac{\sigma}{\rho\omega}\right) \tag{6.7}$$

where ω represents the angular frequency. Thus, the normalized acoustic impedance, i.e. $Z/\rho c_\infty$ = (R + $\iota\chi$)/ρc_∞ for a porous sample of thickness d can be written as,

$$\frac{R}{\rho_0 c_\infty} = \frac{\left(\frac{Z_R}{\rho_0 c_\infty}\right)\sinh\psi\cos h\psi + \left(\frac{Z_I}{\rho_0 c_\infty}\right)\sin\xi\cos\xi}{\cos h^2\psi - \cos^2\xi} \tag{6.8}$$

$$\frac{\chi}{\rho_0 c_\infty} = \frac{\left(\frac{Z_I}{\rho_0 c_\infty}\right)\sinh\psi\cos h\psi - \left(\frac{Z_R}{\rho_0 c_\infty}\right)\sin\xi\cos\xi}{\cos h^2\psi - \cos^2\xi} \tag{6.9}$$

where Z_R and Z_I are the real and imaginary part of the acoustic impedance derived in equation 6.5. In the above equation, the effect of the material thickness is accounted by ψ and ξ, such that ψ = αd and ξ = βd.

6.2. Description of the Numerical Setup

The computational set-up used for the APM-CFD verification study is based on the set-up discussed in chapter 5, with changes essentially in the geometry, the VR strategy and in the fluid/ solid regions. For the sake of brevity, only the modifications made with respect to the setup explained in chapter 5 are mentioned here. All the other parameters should be assumed to be same as in the Honeycomb Liner-CFD setup verification case.

Geometry

The numerical setup used in this chapter is same as that shown in figure 5.2, with the only difference being in the use of the honeycomb liner. Instead of placing a liner, an APM region is placed at the downstream extremity of the waveguide. The APM has a cylindrical geometry which is defined using the radius of the cross-section (r_c) and the thickness (d). The radius of the APM region is equal to the radius of the duct/ waveguide, while the thickness (d) of the APM region is user-defined and is case dependent. Apart from this, the PowerCASE® documentation [16] suggests that the APM should overlap any abutting solid boundary. As the backplate and the duct (see figure 5.2) have been defined as solid regions, care has been given to assure a slight overlap between the solid regions and the defined APM region.

Variable Resolution (VR) Strategy

In the current setup, five VR regions ranging from VR_0 to VR_4 as shown in figure 5.2 are used, with VR_4 being the region with the smallest voxel size and VR_0 being the region with the largest one. Moreover, to assure smooth transition from one VR region to another, an offset distance corresponding to 6 voxels has been assigned. However, it should be noted that there should be atleast two voxels in every direction inside the APM [16]. In cases the current VR strategy is unable to meet this requirement, additional VR regions can be added. Furthermore, in the current setup, the additional near-facesheet VR regions shown in figure 5.5 are not used. This is because, with the APM the need to capture the near/ in-orifice orifice flow field is avoided and thus, additional resolution is not required.

Fluid/ Solid Regions

Like in the setup defined in chapter 5, the waveguide boundary and the backplate have been defined as *solid*, while the simulation volume has been defined as a *fluid region* in the APM-CFD setup. In addition, the APM which is placed at the downstream end of the simulation setup is defined as an *Acoustic Porous Medium* region. This option enables the user to enter the APM parameters such as the APM porosity (ϕ) and the static flow resistance (σ).

6.3. Input Conditions

The input signal used in the current chapter are same as that explained in liner-CFD verification study and are thus, not repeated here for the sake of brevity. In addition to these input conditions, the characterising parameters for the APM fluid are also defined by the user. These parameters in the current chapter correspond to the CT73 Ceramic Tubular Liner [50]. The thickness d and porosity ϕ of the APM are 82.5 mm and 0.57 respectively. The flow resistance σ is calculated using the formula:

$$\sigma = \frac{32\mu}{d_c^2 \phi} \tag{6.10}$$

where μ is the dynamic viscosity and d_c is the micro-channel diameter. For the CT73 liner d_c = 0.64 mm and thus, σ = 2522 kg m^{-3}s^{-1}. The characterising parameters of the APM are summarised in table 6.1.

No.	Parameter	Value	Unit
1	Porosity (ϕ)	0.57	[-]
2	Thickness (d)	82.5	[mm]
3	Flow resistance (σ)	2522	[kg m^{-3}s^{-1}]

Table 6.1: Summary of the APM parameters used in the current chapter

6.4. Resolution Study

In this step of the APM-CFD verification study, a grid convergence study is conducted to establish the resolution for which the simulation result. Simulation results with four different grid resolutions, namely coarse, medium, fine and very fine have been analysed in the current section. These grids have a resolution N_{APM} of 0.23, 0.46, 0.91 and 1.8 voxels/mm respectively. Moreover, in terms of the FEV, the grid size is 0.17806x10^5 , 0.90529x10^5, 6.44575x10^5 and 48.63094x10^5 respectively. A summary of the different grids analysed in this study is given in table 6.2.

The quality of each grid mentioned in table 6.1 is assessed by analysing the normalised acoustic impedance in figure 6.2. The resistance and reactance values shown in the figure is educed using the impedance eduction method mentioned in section 5.2 and is averaged over each virtual probe locations shown in figure 5.7. It can be observed that with an increase in the grid resolution, the value of the resistance peak at the anti-resonance frequency (see section 6.5) increases. A difference of 30% is seen in the anti-resonance peak as the resolution is increased from coarse to medium, while that

between a medium and the fine grid is ≈ 9%. Moreover, for a coarse grid the peak is observed at ≈ 2 kHz while for all the other grids it is seen at a frequency of ≈ 2.1 kHz. Similar trends are also observed in the normalised reactance curve in figure 6.2(b). From this discussion, it is clear that the simulation results are not converged with a coarse grid.

No.	Grid-Type	Smallest Voxel [mm]	Timestep [μsec]	N_{APM} [voxels/mm]	FEV [voxels]
1	Coarse	4.40	6.62	0.23	17,806
2	Medium	2.20	3.31	0.46	90,529
3	Fine	1.15	1.65	0.91	644,575
4	Very Fine	0.55	0.83	1.80	4,863,094

Table 6.2: Summary of the grids used for the grid resolution study

On the other hand, the difference between the anti-resonance resistance and reactance peak between the medium and the fine grid is only 9% and 6% respectively, which is quite small. However, from figure 6.3, where the value of OASPL of the input signal as obtained from the simulation is given, it is seen that the medium grid predicts a value an OASPL = 127 dB which is not correct. With a fine-grid however, a correct input OASPL of 130 dB is obtained. Thus, it can be said that the resolution corresponding to the medium grid is not appropriate for discretizing the input acoustic signal. Furthermore, hardly any difference is seen between the resistance and reactance curves from the simulations conducted with fine and very-fine grid, while the FEV increases by 86% between these two grids which can lead to a considerable increases in the computational effort. Thus, the use of the resolution N_{APM}= 0.91 voxels/mm for the APM simulations is justified.

On comparing the current resolution study with that conducted in section 5.9, it can be seen that smallest voxel size corresponding to the chosen resolution in the current case is 95% bigger than that chosen for the honeycomb liner case. This is because with an APM, the need to discretize the near/ in-orifice flow field can be bypassed. This leads to a considerable reduction of the computational effort for the current case. Moreover, until the condition of two voxels per APM is satisfied (as mentioned in PowerCASE® documentation [16]), the chosen resolution of N_{APM}= 0.91 voxels/ mm can also be used for simulations with different APM geometry. Previously, Sun et al. [65] conducted a numerical study with the Acoustic Porous Medium model to mimic the acoustic properties of the CT73 liner and observed convergence with a resolution of 0.78 voxels/mm which is very close the selected resolution in the current section.

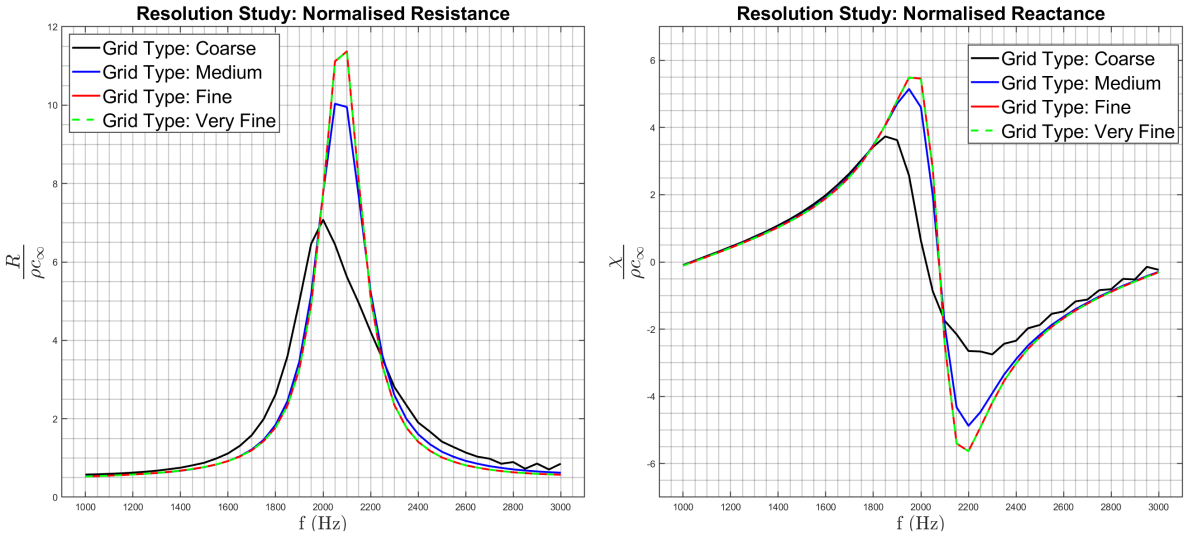

(a) Normalised Resistance

(b) Normalised Reactance

Figure 6.2: Impedance spectra from the grid resolution study in APM setup verification

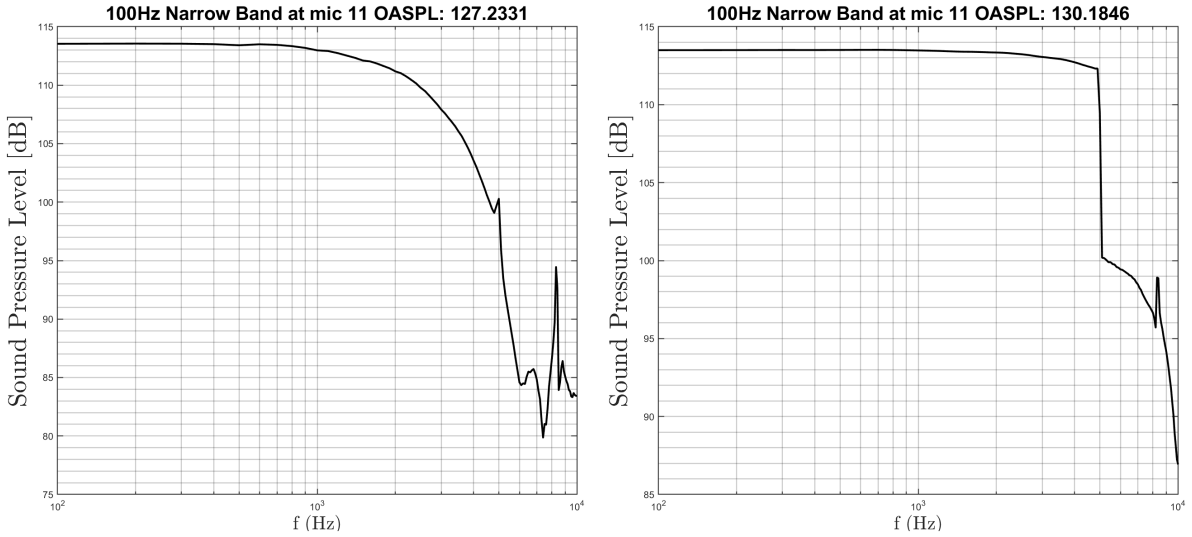

(a) Medium Grid

(b) Fine Grid SPL

Figure 6.3: OASPL of the input signal for different grid type obtained from simulations

6.5. Comparison with Experimental and Analytical results

In the next step of the verification study, the normalised resistance and normalised reactance curves from the simulations are compared with the experimental and analytical results in the figure 6.4(a) and figure 6.4(b) respectively.

The reference experimental results are taken from the study of Jones et al. [50], who tested the CT73 liner (see figure 3.6) under normal-incidence conditions with an input SPL of 130 dB. However, contrary to a broadband input used in the current thesis, a tonal input was used in [50]. On the other hand, the analytical results shown in the figure 6.4 have been obtained using the Hersh & Walker model [25]. In the figure 6.4, the solid line represents the mean value while the shaded region represents the scatter in the impedance values. From figure 6.4(a), it is seen that the simulation results agree quite well with the experimental results at f = 0.5 kHz, 1 kHz and 3 kHz. At f = 1.5 kHz, 2 kHz and 2.5 kHz however, an average difference of 25% is seen between the experimental and simulation results. Similar trends are observed in the normalised reactance plot in figure 6.4(b). For frequencies $f \leq$ 1.5 kHz, the simulation results shows a good match with the reference experimental and analytical results. Although discrepancies are observed for frequencies f > 1.5 kHz, for f > 2.5 kHz all the cases seem to converge towards the same value.

The discrepancies, especially those observed near the resistance and reactance peak, can be attributed to the phenomenon of anti-resonance. At anti-resonance, an acoustic node is formed at the backplate of the simulation setup and at the interface of the APM fluid. This causes the acoustic resistance to increases and the acoustic reactance to jump from a large positive value to a large negative value, consequently leading to a minimum absorption of the acoustic energy. The anti-resonance frequency of a liner is a function of its thickness (d), such that f_{ar} = $(n+1)c_\infty/2t$. Using this expression, the anti-resonance for the CT73 liner is predicted for f_{ar} = 2.078 kHz, which is inline with the simulation results. Sun et al. [65] have mentioned that close to the anti-resonance frequency, thermal and structural effects such as vibrations can dominate the attenuation process. The current APM model doesn't account for such effects, and thus, these discrepancies should be expected. Furthermore, some difference could arise due to the different initial conditions used within the experimental and the simulation studies.

Anyways, the discussion presented above shows that the APM is able to reproduce the acoustic effects of the CT73 liner, with discrepancies only near the anti-resonance frequency. More importantly, the current simulation results match exactly with that obtained from the numerical study conducted by

Sun et al. [65]. With such results, the use of the current simulation setup to analyse the acoustic performance of the APM corresponding to the reference honeycomb liner through different properties is justified.

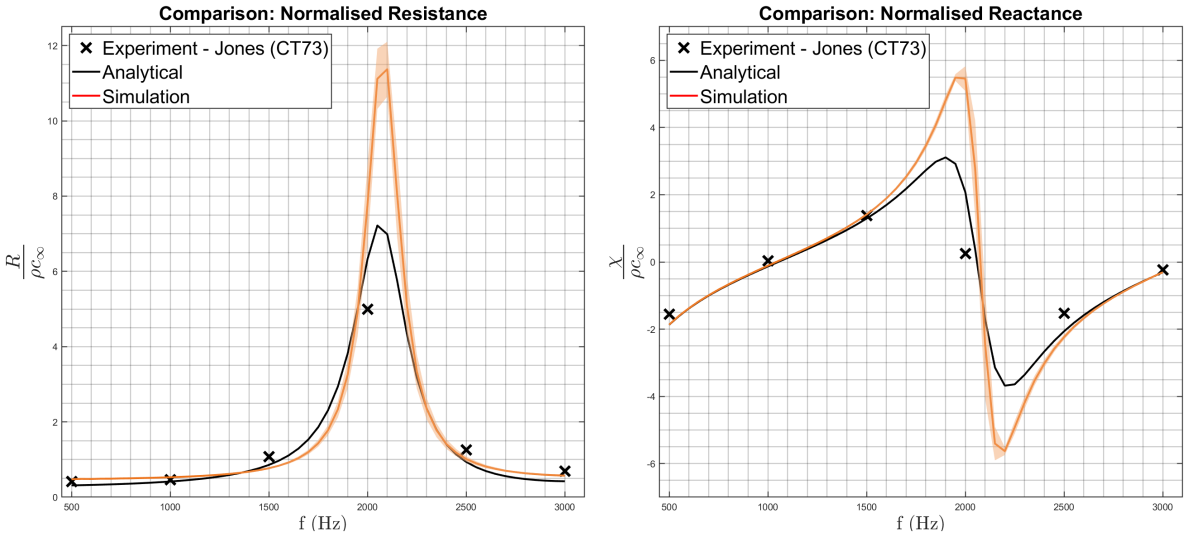

(a) Normalised Resistance

(b) Normalised Reactance

Figure 6.4: Comparison of CT73 simulations with experimental and analytical results

7

Experimental Campaign

Before extending the use of the APM model to mimic the acoustic effect of the reference honeycomb liner, it is essential to obtain model parameters that can accurately account for the liner effects. Apart from obtaining the parameters through an inverse analysis of a *priori* known impedance, a possible approach to derive the characterising parameters of the APM is through a pressure drop experiment. This approach involves calculating the pressure drop across the perforated facesheet of the reference liner, under a steady flow input. The pressure drop values can be further related to the flow resistance σ through a pressure drop model. The general idea behind the current methodology is illustrated through an overview in figure 7.1.

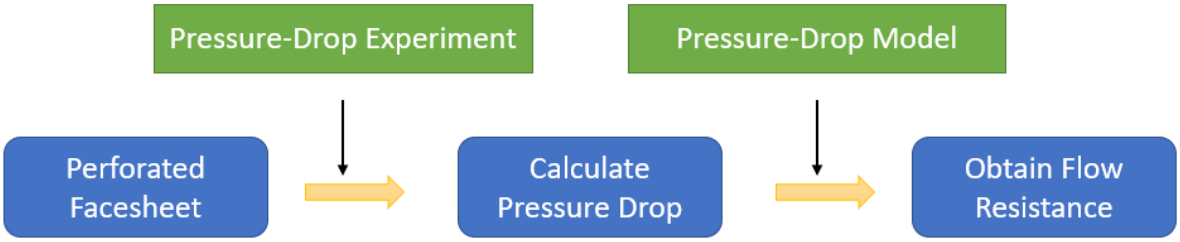

Figure 7.1: Illustration of the pressure-drop experimental procedure

The chapter starts with a description of the perforated test article and the experimental setup in section 7.1 and section 7.2 respectively. Thereafter, the test matrix of the pressure drop experiment is given in section 7.3, followed by an illustration of the pressure drop model in section 7.4. Finally, this section concludes with a brief verification study of the present experimental approach in section 7.5.

7.1. The Perforated Test Article

The perforated facesheet used in the current experimental campaign has the same geometric parameters as the facesheet of the 6.4% porosity honeycomb liner given in Jones et al. [31]. The perforated article, which is shown in figure 7.2, has a plate diameter D of 55 mm and a plate thickness t_f and hole diameter d_o of 0.64 mm and 0.99 mm respectively. Furthermore, the distribution of holes is based on the repetition of the hexagonal pattern, where the hole spacing l controls the plate porosity ϕ. The choice of the hexagonal hole arrangement is made to maintain the uniformity with the arrangement used in the numerical perforated plate (see figure 5.4). The plate porosity (ϕ) is defined as the ratio of empty to solid volume, and for a plate with holes arranged in a hexagonal pattern, can be calculated using the formula:

$$\phi = \frac{14\pi d_o^2}{36\sqrt{3}l^2} \tag{7.1}$$

With a hole diameter d of 0.99 mm and a hole spacing l of 3.29 mm the plate porosity comes out to be 6.4%. The value of the geometric parameters of the perforated plate are summarised in table

7.1. Moreover, it should be noted that the perforated plates were manufactured at the *Electronic and Mechanical Development Service* (DEMO) at the Delft University of Technology.

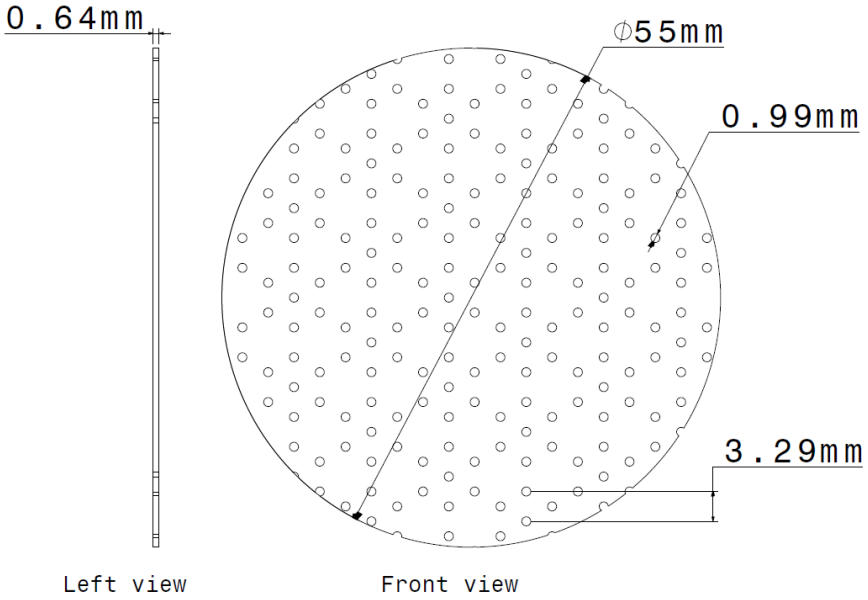

Figure 7.2: Perforated facesheet used in the current experimental campaign

Parameter	Value
Plate thickness (t_f)	0.64 mm
Plate diameter (D)	55 mm
Hole diameter (d_o)	0.99 mm
Distance between holes (l)	3.29 mm
Plate porosity (ϕ)	0.064

Table 7.1: Geometric Parameters of the perforated facesheet

7.2. Setup for the Pressure Drop Experiment

After the production of the perforated plate, the next step involves measuring the pressure drop across it. This was achieved through experiments conducted with the permeability rig which is present at the *Low Speed Wind Tunnel Laboratory* at the Delft University of Technology. An illustration of the permeability rig is given in figure 7.3.

The permeability rig configuration starts with an external air-supply which is pressurized at 10 bar. The air-supply is attached to a pressure regulator which is further connected to the mass-flow controller. The mass controller used in the present experimental setup is the Bronkhorst F-202AV-M20-DGD-55-V. The air then passes through the valve and the diffuser before subsequently entering the pipe. Next, the air flows through the test section which houses the perforated article (figure 7.2), across which the pressure drop is measured. Finally, the air reaches the exhaust where it is vented out into the atmosphere. The actual setup used in the current experiment is shown in Figure 7.4. The position of the diffuser, the test section, the pressure transducer and the mass flow controller can be viewed in this figure. A close up view of the test section is shown in figure 7.5, where the guide pins and the pressure probes are labelled. The guide pins ensure a proper alignment of the perforated plate, while the probes measure the pressure values at the upstream and downstream locations. These pressure probes are further connected to a mensor 2101 differential pressure sensor, which can measure pressure drop within a range of 1.2 kPa to 15 kPa, with an accuracy of 2 Pa.

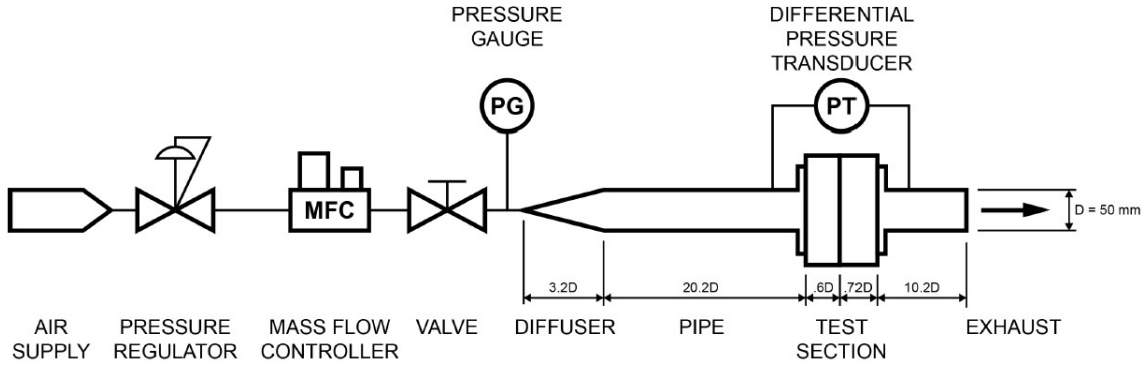

Figure 7.3: Schematic of the permeability rig used in the pressure drop experiment (not to scale)

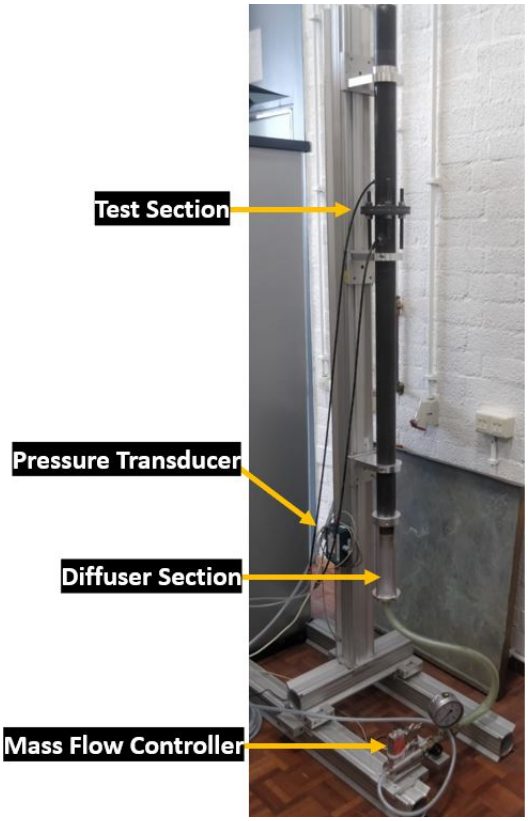

Figure 7.4: Permeability Rig used for the pressure drop measurements

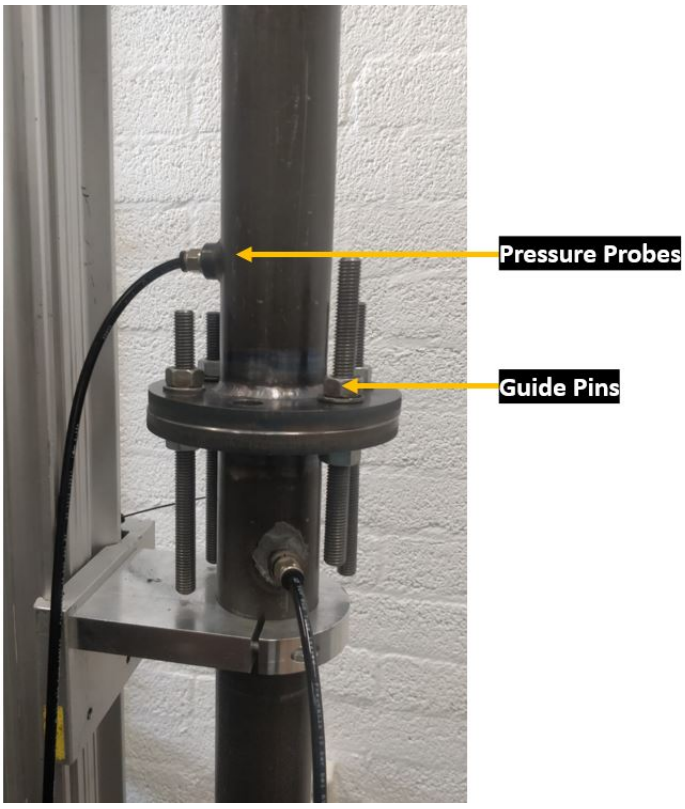

Figure 7.5: Close-up view of the test section

7.3. Test Matrix

In the current experiment, the pressure drop across the perforated facesheet has been measured for 20 velocity values between 0 m/s and 1.1 m/s. For the present experiment, two different plate configurations were analysed as summarized in table 7.2. Run-1 is corresponds to the experiment with the baseline plate, while in Run-2 the perforated plate from Run-1 is inverted such that the downstream part of the plate is now facing the flow. There might be a difference in the shape of the holes/ edges on either side of the perforated plate, which can be caused due to the techniques used in plate manufacturing. Thus, it is wise to measure the pressure drop by inverting the perforated facesheet. Moreover, calculating the pressure drop values for two different configurations will ascertain the repeatability of the measurements.

	Velocity Range (m/s)	Comment
Run - 1	0 - 1.1	Test with baseline plate
Run - 2	0 - 1.1	Test with inverted plate

Table 7.2: Test Matrix for the pressure drop experiment

7.4. Pressure Drop Model

The pressure drop model used in the current thesis is based on the Darcy's law [26], which states that the pressure drop across a material is a sum of the viscous losses within the pipe and the inertial effects, which are related to the shape/ form of the material. The viscous losses in a pipe scales linearly with the inflow velocity, while the inertial effects scales quadratically with the inflow velocity. These two effects are modelled through the Hazen-Dupuit-Darcy equation [26] as,

$$\frac{\Delta p}{t_f} = \frac{\mu}{K} v_d + \rho C v_d^2 \tag{7.2}$$

where Δp represents the pressure drop across the plate, μ is the dynamic viscosity, K is the permeability and v_d is the Darcian velocity which is defined as ratio of the volumetric flow rate at the cross sectional area of the pipe. C is the form factor which represents the inertial effect, while ρ is the fluid density. In equation 7.2, the term $\frac{\mu}{K}$ represents the viscous contribution to the pressure drop and is called the viscous resistance (σ_v), while C represents the pressure drop due to the entrance and exits effects and is called the inertial resistance (σ_I). Thus, the flow resistance (σ) of the perforated plate is defined as the sum of the viscous and the inertial component and is given as:

$$\sigma = \sigma_I + \rho \sigma_I v_d \tag{7.3}$$

In the current thesis, the values of the pressure drop (Δp) along with that of the Darcian velocity (v_d), the viscosity μ, and the density (ρ) are calculated from the experiment conducted with the permeability rig (section 7.2). The two unknown variables, i.e. the permeability K and the form coefficient C are calculated using a least-square fitting of equation 7.2 to the 20 pressure drop values. Figure 7.6(a) shows the pressure drop curve along with the corresponding least square fit in figure 7.6(b) for the configuration mentioned as Run-1.

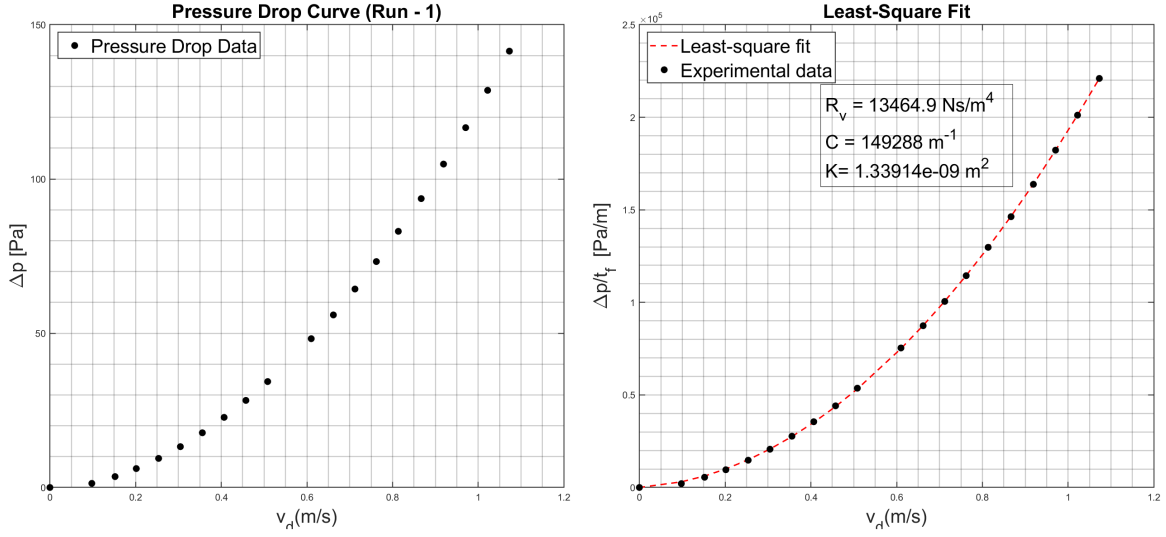

(a) Pressure drop curve

(b) Least square fit with equation 7.2

Figure 7.6: Pressure drop result for Run - 1

It is seen that the pressure drop across the perforated plate increases quadratically with the inflow velocity. This trend of the pressure drop curve is in agreement with quadratic nature of the equation

7.2. From figure 7.6(b), it can be seen that the least square fit is obtained for the values of viscous resistance σ_v = 13464.9 Ns/m^4 and inertial resistance σ_I = 149288 m^{-1}. Thus, the flow resistance of the perforated plate used in Run - 1 is given by,

$$\sigma = 13160.6 + 149556\rho v_d \tag{7.4}$$

With the knowledge of the flow resistance from equation 7.4 and the plate porosity (ϕ), the APM fluid corresponding to the perforated plate shown in figure 7.2 can be characterised. It should be noted that the flow resistance obtained above are dependent on the thickness of the perforated sheet. Thus, while characterising the APM through the parameters given in equation 7.4, the APM thickness should be the same as that of the perforated facesheet, i.e. 0.64 mm.

Anyways, this method of using Darcy's law to obtain the flow resistance and subsequently the characterising parameters of the APM is also employed by Carpio et al. [60], [11].

7.5. Verification of the Experimental Approach

In the previous section, a pressure drop model based on the Darcy's equation is introduced and is subsequently used to obtain the flow resistance for the perforated plate configuration in Run-1. In an effort to verify the experimental results, the current section presents a repeatability study where the flow resistance from Run-1 and Run-2 are compared.

Moreover, it should be noted that the Darcy's law given by the equation 7.2 is derived only for porous materials [26] such as that shown in figure 1.3. In the current case however, it is being used to obtain the flow resistance for a perforated facesheet as shown in figure 7.2. As established through the discussion presented in chapter 2 and chapter 3, the pressure drop and subsequently the acoustic absorption by the perforated plate and a porous material can be governed by different phenomenons. It is thus necessary to verify the use of Darcy's law to model the pressure drop across a perforated plate. In this section, this is achieved by comparing the flow resistance obtained from equation 7.2 with that from the method mentioned by Kraft et al [38].

7.5.1. Reproducibility Check

The results from the reproducibility study can be seen in figure 7.7. For Run-1 the value C is greater than that of Run-2 by $\approx 1\%$. On the other hand, the difference in the value of σ_v between Run-1 and Run-2 is $\approx 14\%$. Such differences can be caused due to imperfections in the perforated plate model or due to random errors within the measurement system, however these errors are not quantified in the current study. Anyways, the differences in the values of viscous and inertial flow resistance are small and the results are considered as reproducible.

7.5.2. Comparison with Kraft's Model

According to Kraft et al. [38], the pressure drop across a perforated plate is related to the "DC"/ steady flow resistance as,

$$\frac{\Delta p}{t_f} = \sigma \cdot u \tag{7.5}$$

where u is the velocity in the pipe and σ is defined as,

$$\sigma = \frac{32\mu}{\phi C_D d_o^2} + \frac{\rho(1-\phi^2)}{2\left(\phi C_D\right)^2}u \tag{7.6}$$

The first term on the right hand side is based on the Hagen-Poiseuille pipe flows [17] and signifies the losses due to viscous effects. Just like in Darcy's equation, this term also scales linearly with the inflow velocity. The second term on the other hand, represents the losses due to the formation of a non-linear turbulent jet, and it scales with the square of velocity which is similar to Darcy's law.

On comparing equation 7.2 and equation 7.6, the viscous resistance σ_v and the form coefficient C can be written as,

$$\sigma_v = \frac{32\mu}{\phi C_D d_o^2} \qquad C = \frac{1-\phi^2}{2(\phi C_D)^2} \tag{7.7}$$

In the above equation, the discharge coefficient C_D is the only remaining unknown. This variable can be calculated by fitting equation 7.6 to the pressure drop curve using the method of least-squares. The least square fit for the configuration mentioned as Run-1, and the corresponding values of σ_v and C are shown in figure 7.8. The values of the viscous resistance and form coefficient obtained using Darcy's law and Kraft's method are compared in table 7.3.

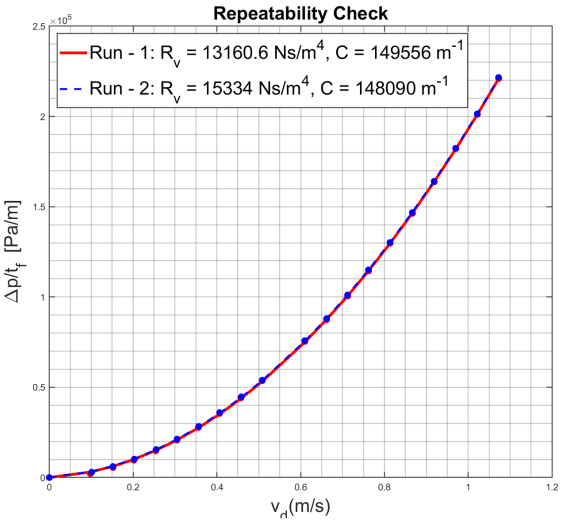

Figure 7.7: Repeatability Check

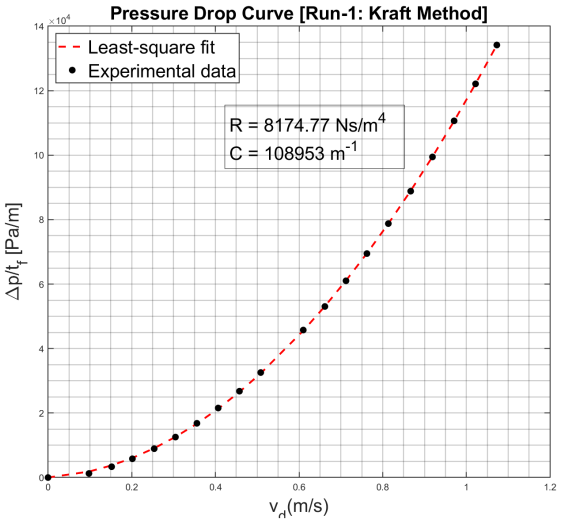

Figure 7.8: Least square fit using equation 7.6

Method	σ_v (Ns/m^4)	C (m^{-1})
Darcy	13160.6	149556
Kraft	8286.65	185314

Table 7.3: Comparison between Kraft's method and Darcy's equation

It can be seen that the value of σ_v predicted by Kraft's method is $\approx$ 35% lower than that predicted by the Darcy's law. On the other hand, the value of C for the Kraft's method is $\approx$ 19% lower than that given by the Darcy's law. The observed discrepency in the two cases is due to the difference in the definition of the viscous and inertial term between the Darcy's law and the Kraft's method. The fact that Kraft's method is derived based on the flow physics of the perforated plate should imply that the resistance values from this method have a physical meaning. However, a limitation of the current method can be seen by comparing equation 7.6 with equation 2.8. Kraft's method doesn't account for the effect of mass-inertia on the resistance offered by the perforated facesheet, which can be dominant especially for facesheets with t_f/d_o < 1 [49]. Thus, ideally one additional term which can account for the mass-inertia should be incorporated with the Kraft's method. Anyways, this method is commonly used to measure the flow resistance across the perforated plate in the state of the art [38], [49] and thus, using it in the current thesis is justified.

Furthermore, it would be ideal to compare the performance of the Acoustic Porous Medium with the parameters derived from the Darcy's law and that derived from the Kraft's method.

III

Results

8

Characterisation of APM through Inverse Formulation

Now that the use of the current computational setup with an APM is verified in chapter 6, the capability of the APM to mimic the acoustic effects of the reference honeycomb liner (see section 5) can be analysed. In the current section, the APM model parameters are derived through the inverse formulation available in PowerFLOW®. This feature uses a *priori* known impedance curve as an input, and gives the APM parameters such as ϕ, σ and t corresponding to the input *priori* impedance. In the present case, the normalised acoustic resistance and reactance values corresponding to the 'fine' grid in chapter 5 are used as the input curve for the inverse algorithm. After obtaining the model parameters, the performance of the APM can be analysed. The general methodology of this approach is summarised in figure 8.1.

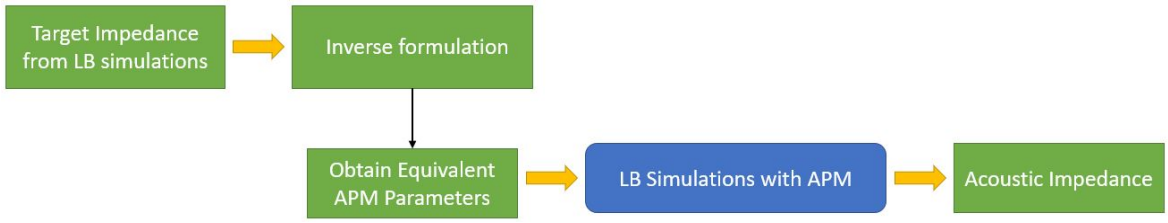

Figure 8.1: Methodology of APM simulations using the inverse algorithm

Clearly, the current approach overlooks the structural differences between the honeycomb liner and an APM fluid as seen in figure 8.2. While the honeycomb liner is comprised of a perforated facesheet and a backing cavity, the APM is a homogeneous fluid region. Moreover, the honeycomb liner is a locally-reacting liner while the APM is an extended-reacting type liner. Representing a locally-reacting type liner as an extended-reacting one is not entirely physical and this should be taken into account while assessing the results.

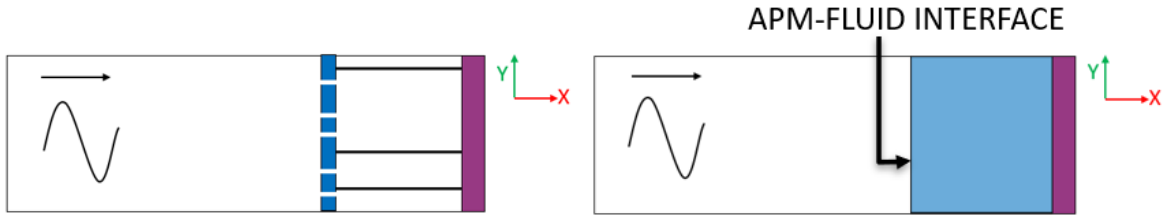

(a) 2D Impedance tube with honeycomb liner

(b) 2D Impedance tube with Acoustic Porous Medium

Figure 8.2: Comparison of the impedance tube setup with the honeycomb liner and APM geometry

8.1. Input Conditions

The input acoustic signal used in the present chapter is the same as that mentioned in table 5.1. In addition, the inverse formulation gives a viscous flow resistance (σ_v) = 828.8 1/s, an APM porosity (ϕ) = 0.575, and a thickness (d) = 38.1 mm. These characterising parameters are summarised in table 8.1.

Variable	Value	Unit
Viscous Flow Resistance (σ_v)	826.8	[1/s]
Porosity (ϕ)	0.575	[-]
Thickness (d)	38.1	[mm]

Table 8.1: APM parameters derived through the inverse algorithm

8.2. Bandpass-Filtered data

Bandpass-filter pressure fluctuations p' = p - p_∞ are shown in figure 8.3 at different frequencies, for a probe located 1-voxel length upstream and downstream of the APM-fluid interface respectively. The corresponding velocity fluctuations, normal to the APM-fluid interface are shown in figure 8.4. From figure 8.3, it is seen that the amplitude of pressure fluctuations decreases from a maximum value at f = 1 kHz to a minimum at f = 2.5 kHz. Furthermore, the pressure amplitude downstream of the interface is lower than that at the upstream location at all the frequencies. This pressure drop can be attributed to the interface resistance offered by the fluid-APM interface (see section 4.2). Moreover, the relative amplitude at the two probe locations are a function of frequency, with a maximum pressure drop of ≈40% and a minimum of ≈0.5% observed at f = 2.5 kHz and f = 1 kHz respectively. On the other hand, their relative phase is less variable to the change in frequency.

Contrary to the trends seen in figure 8.3, the amplitude of normal velocity fluctuations is maximum at f = 2.5 kHz, with similar values at f = 2 kHz, and minimum at f = 1 kHz. This behaviour can be explained by the fact that for the current APM region with d = 38.1 mm, the quarter-wavelength for f = 2.25 kHz co-incides with the APM interface. For any acoustic signal, the maximum velocity is observed at it's quarter wavelength and thus, higher velocity amplitudes are observed for frequencies closer to f = 2.25 kHz in figure 8.4. Allard & Atalla [4] have shown that for equivalent fluids backed by a solid boundary, the frequency at which the quarter wavelength intersect the fluid-interface is the resonance frequency. This suggests that for an equivalent fluid the resonance frequency is the function of its thickness d. This trend is also observed through the discussion in section 8.3. Besides this, the normal velocity at all the frequencies increases across the APM interface. This velocity jump is in accordance with equation 4.14 which dictates the mass-flux conservation across the APM interface.

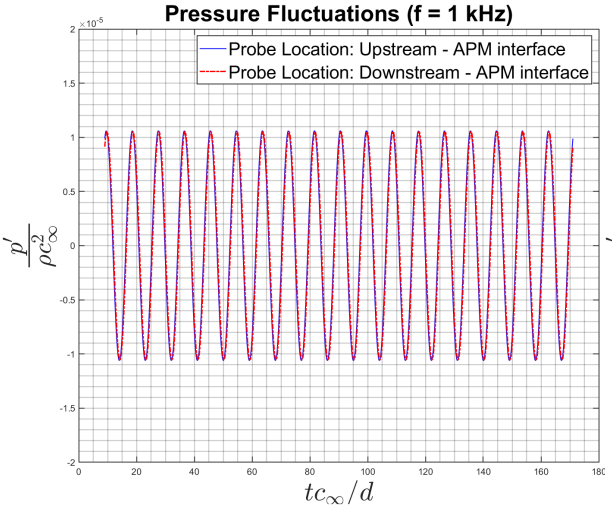

(a) f = 1 kHz

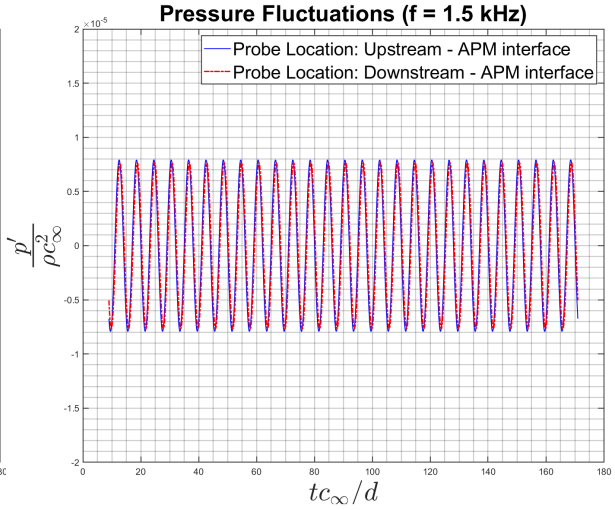

(b) f = 1.5 kHz

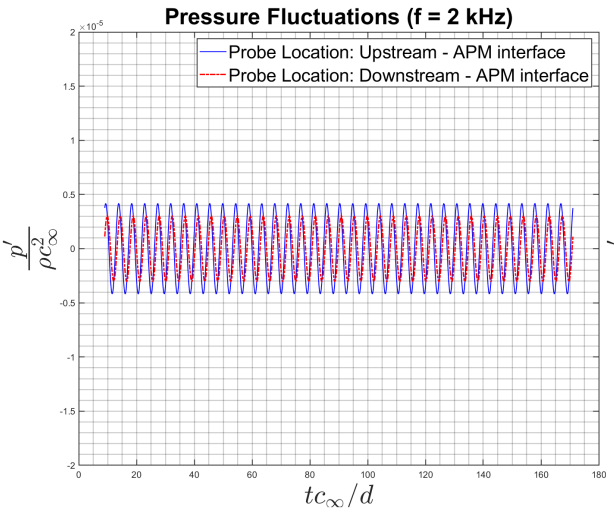

(c) f = 2 kHz

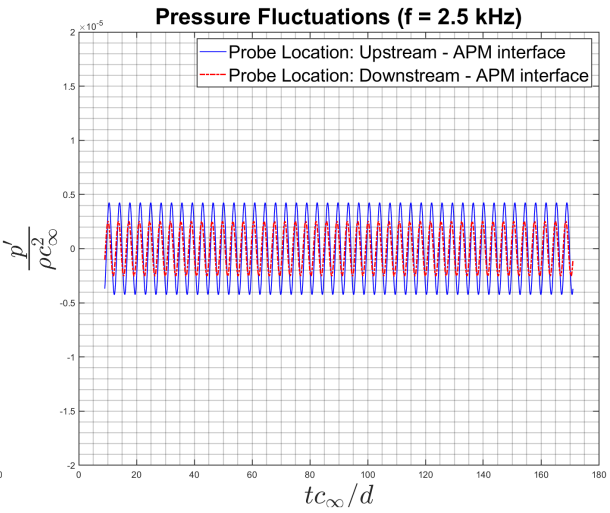

(d) f = 2.5 kHz

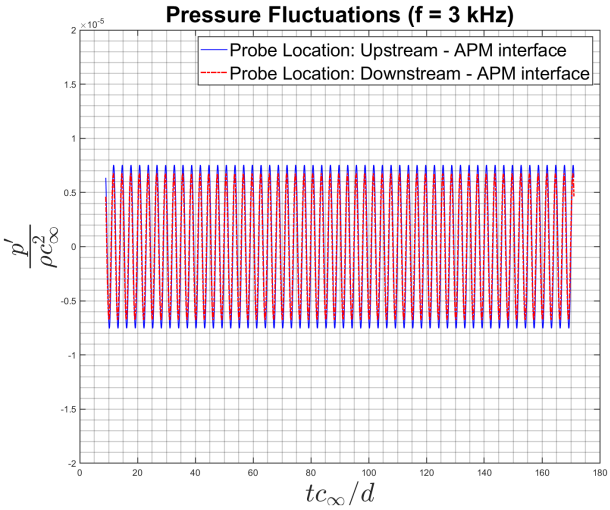

(e) f = 3 kHz

Figure 8.3: Comparison of pressure fluctuation across the APM interface at different frequencies

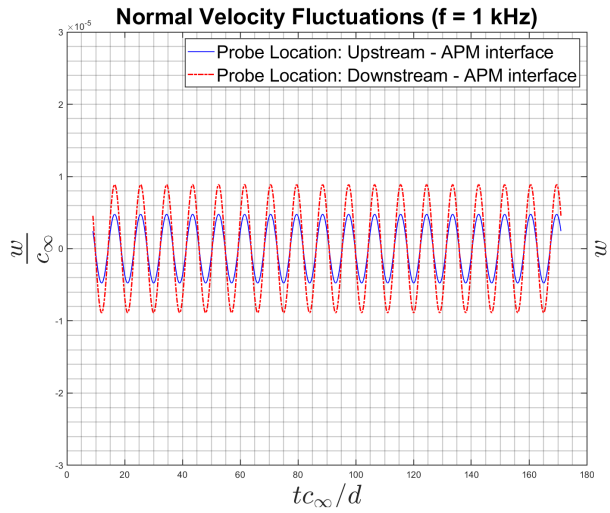

(a) f = 1 kHz

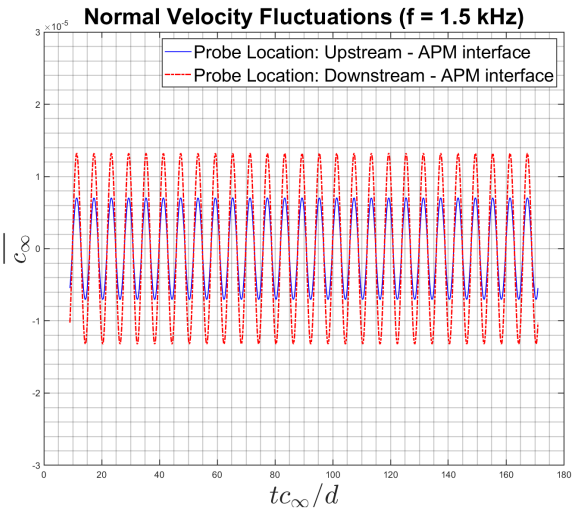

(b) f = 1.5 Hz

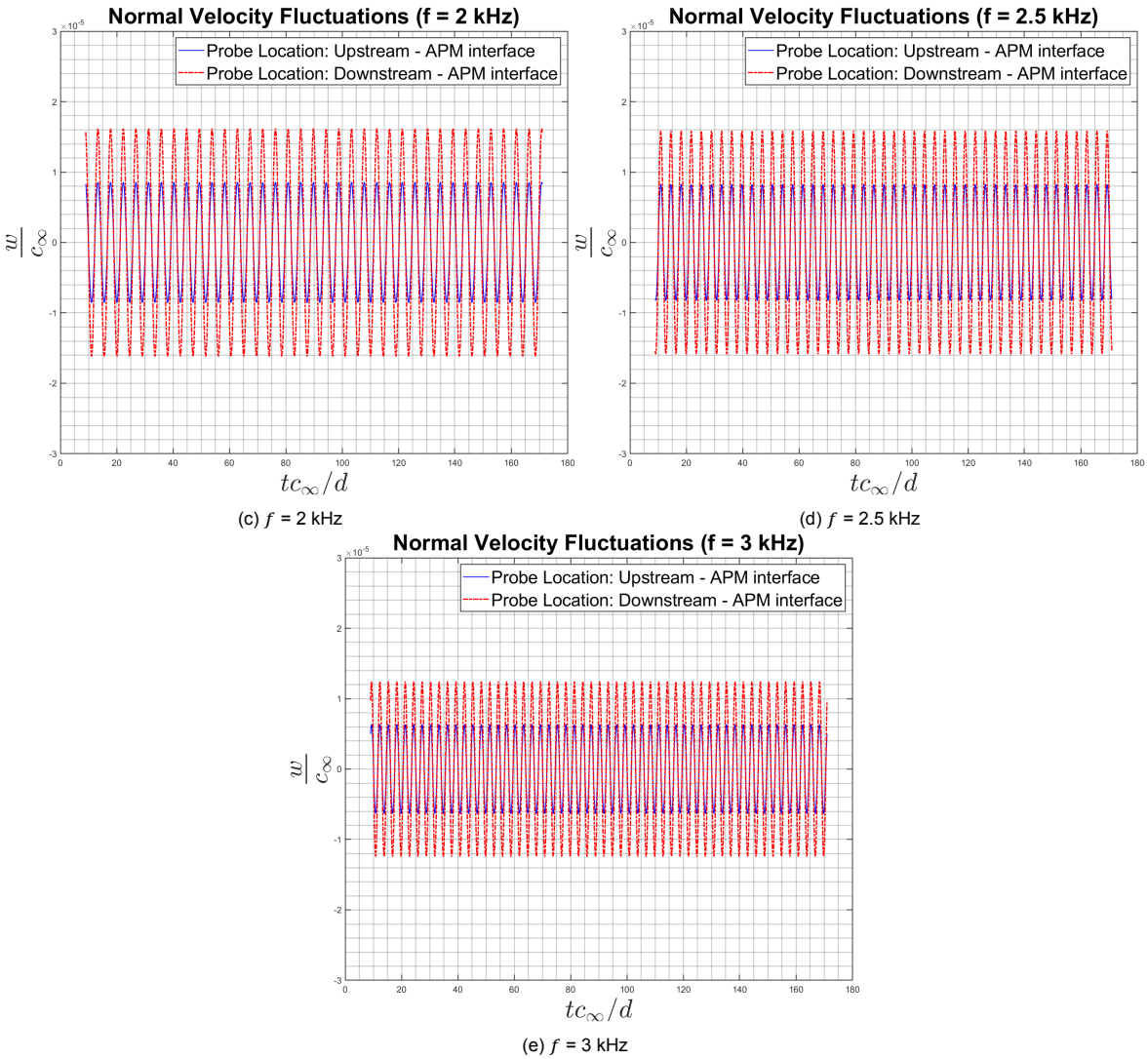

(c) f = 2 kHz

(d) f = 2.5 kHz

(e) f = 3 kHz

Figure 8.4: Comparison of normal velocity fluctuation across the APM interface at different frequencies

8.3. Comparison with honeycomb liner simulations

Figure 8.5 and figure 8.6 presents the pressure fluctuations and normal velocity fluctuations respectively, for the honeycomb liner simulations conducted in chapter 5. These recordings are taken at a probe located 3-orifice radii upstream of the liner facesheet. From the impedance curves given in figure 5.10(b), it is seen that the resonance frequency of the honeycomb liner is f_o = 1.5 kHz, and consequently, the maximum normal velocity and minimum pressure amplitude is observed at this frequency. contrary to this, the resonance for the APM is observed at f ≈2 kHz as seen from figure 8.3 and 8.4.

Despite having the same thickness (see table 8.1 and figure 5.3), the resonance frequency for the honeycomb liner and the APM is different. The reason for this trend can be understood by comparing the near-orifice streamlines for the honeycomb liner with those at the fluid-APM interface. From figure 8.7(a), it is seen that the flow converges and diverges as it enters and exits the orifice respectively, with substantial flow separation observed at the orifice edges. According to Melling [45] and Motsinger [46], this distortion of the acoustically-excited flow causes the resonance frequency to shift to lower frequencies. This effect is termed as the mass-reactance effect [46]. Clearly, the near/ in-orifice flowfield cannot be replicated in the simulations with the APM (figure 8.7(b)), as its structure is completely different than the facesheet of the liner. Thus, in addition to the thickness of the liner, the mass-reactance also influences the resonance frequency of the honeycomb liner. For the APM however, the resonance

frequency seems to be effected only by it's thickness.

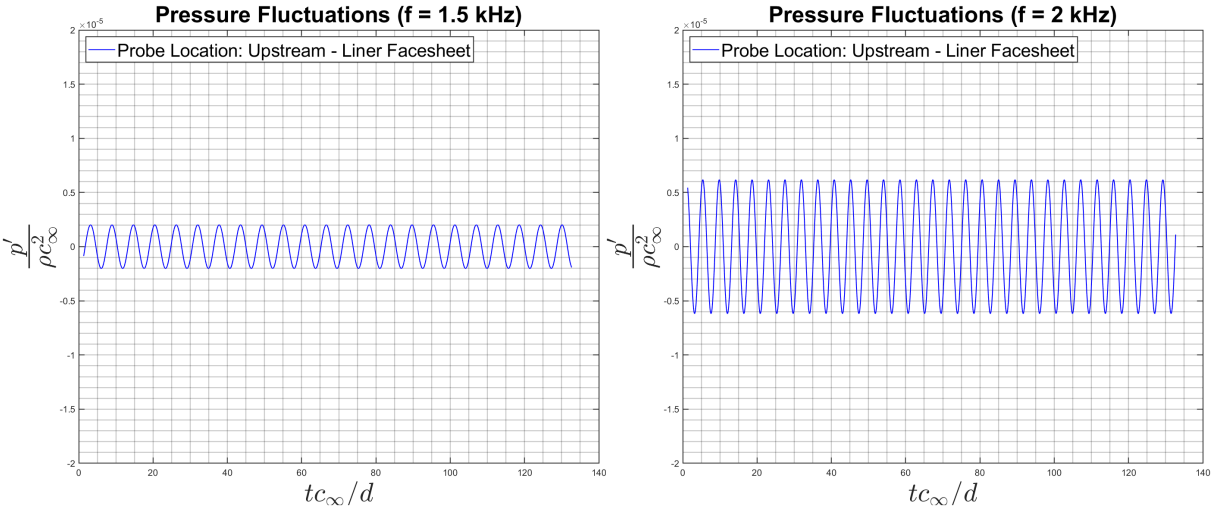

(a) f = 1.5 kHz

(b) f = 2 kHz

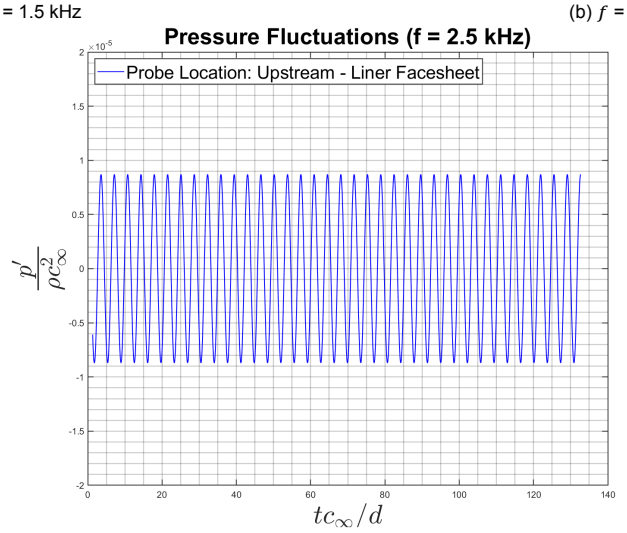

(c) f = 2.5 kHz

Figure 8.5: Pressure fluctuations upstream of the liner facesheet at different frequencies (OASPL = 130 dB)

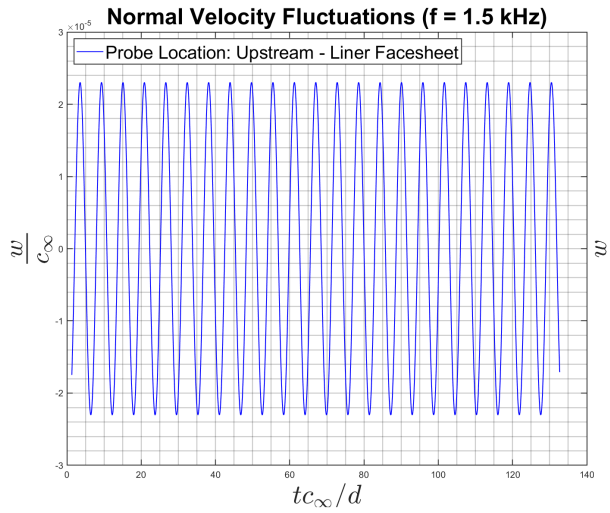

(a) f = 1.5 kHz

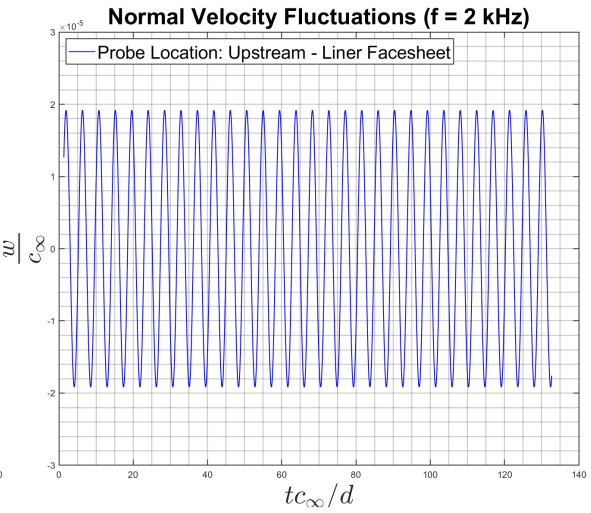

(b) f = 2 kHz

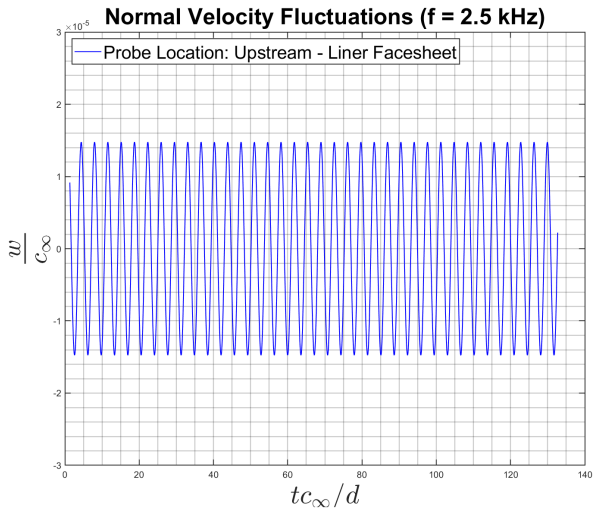

(c) f = 2.5 kHz

Figure 8.6: Normal velocity fluctuations upstream of the liner facesheet at different frequencies (OASPL = 130 dB)

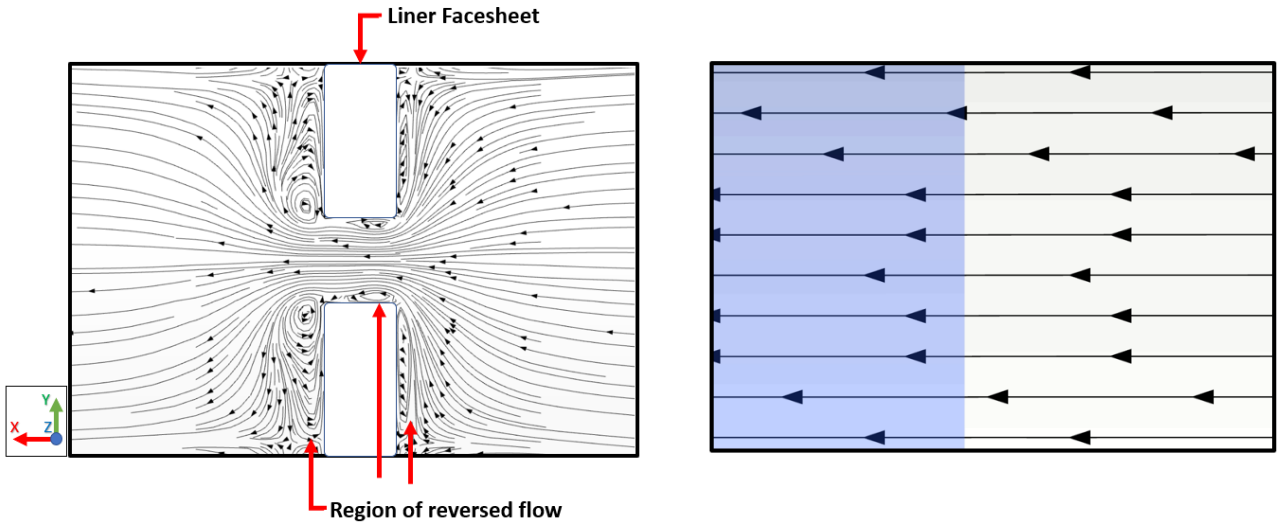

(a) Near-Orifice

(b) Fluid-APM Interface

Figure 8.7: Streamlines at $\theta = \pi/2$

Next, the normalised resistance and reactance curves from the APM simulations are compared with the reference results in figure 8.8. Ideally, the Simulation - APM result should match perfectly with the Simulation - Honeycomb Liner result, as this curve is used to derive the APM parameters through the inverse algorithm. The Simulations - APM gives a normalised acoustics resistance value of ≈ 0.34 which is almost constant over the entire frequency range. This value is higher than the honeycomb liner case by almost 55% over the entire frequency ROI. Furthermore, the resistance value from the APM simulations is considerably higher than the reference experimental result.

Besides this, a significant difference is seen between the resistance values of Hersh & Walker model and that of the APM simulations. This trend is explained by the fact that in addition to the resistance provided by the Darcy's force term (see section 4.2), the APM offers additional resistance to the incoming acoustic wave at the fluid-APM interface. Although the Hersh & Walker model uses the Darcy's force term (see equation 6.2), it doesn't include any term to model the 'interface' resistance. This explains the difference between the APM and analytical resistance in figure 8.8(a).

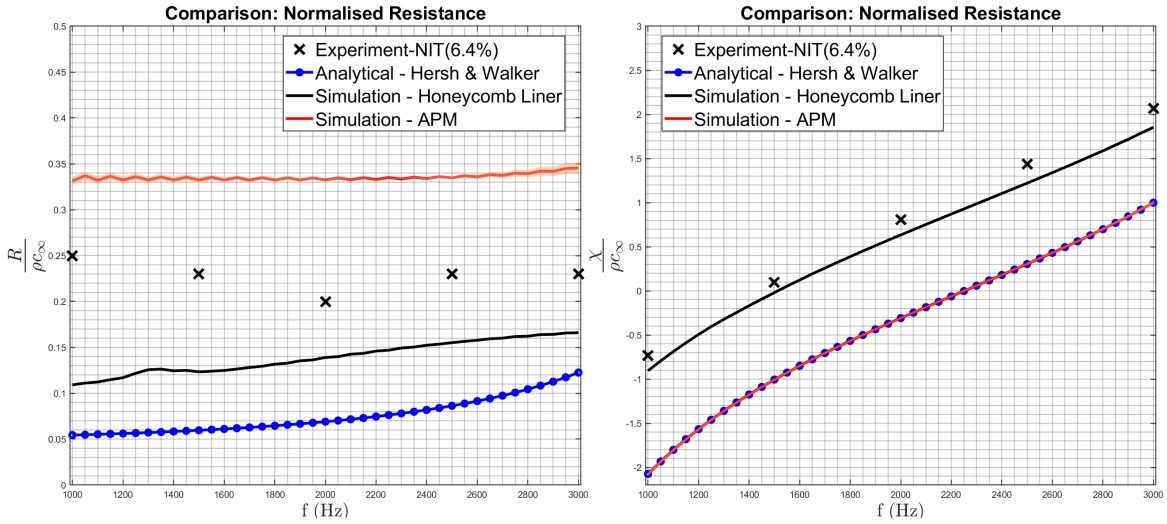

(a) Normalised Resistance (b) Normalised Reactance

Figure 8.8: Normalised Impedance corresponding to the APM parameters derived using the inverse formulations

From figure 8.8(b), it is seen that the APM simulation predicts a resonance frequency of 2.25 kHz which is higher than that predicted by the honeycomb liner simulations. Furthermore, the reactance value from the APM-simulations is ≈52% lower than that from the reference simulation with the honeycomb liner, over the entire frequency range. As explained earlier, this trend is caused because the mass-reactance effect, which is dominant in case of honeycomb liner, is not observed with the APM simulations. This claim is further supported by figure 8.9. In this figure, the normalised reactance curve from the APM *simulation* matches perfectly with the cotangent term, -ιcot(kd)/ϕ, which represents the reactance due to the APM thickness as explained in chapter 2. The fact that the Simulation-APM curve perfectly matches this cotangent term shows that the APM with the current set of parameters can only predict the cavity reactance which is essentially dependent on the input d and ϕ.

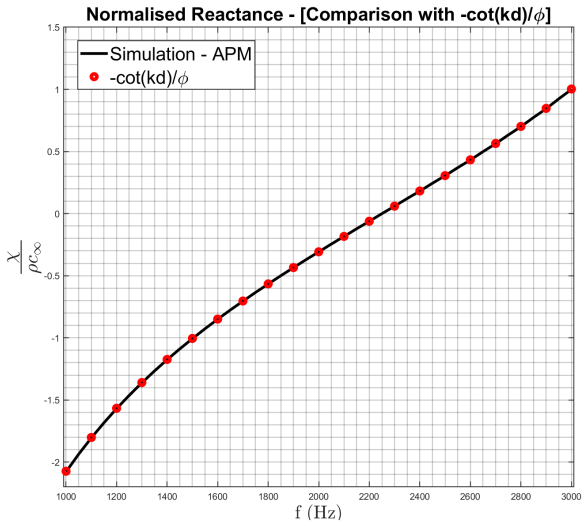

Figure 8.9: Comparison of normalised reactance curve with -ιcot(kd)/ϕ

Clearly, with the set of parameters given in table 8.1, the simulations with APM are not able to reproduce the acoustic effects of the reference honeycomb liner. The trends observed above might be explained by the fact that APM is based on Darcy's law which is derived only for porous materials. Thus, it might not be possible for the Darcy's law to account for certain honeycomb liner effects, such as the mass reactance. If this is true, then the APM parameters σ_v, ϕ and d are not adequate to give an accurate prediction of the reference impedance results and thus, additional parameters might be required to

improve the impedance prediction. The prospect of using additional parameter to characterise the APM is discussed in the next section.

8.4. Advanced Fluid-APM Interface Modeling

The current section investigates the use of the *Advance Fluid-APM Interface Modeling* option present in PowerFLOW®. This modeling option imposes an advanced velocity-pressure physical relationship at the fluid-APM interface, which might enable a more accurate modelling of thin perforated plates, such as that seen in figure 8.7(a) [16]. In addition to the parameters mentioned in table 8.1, the *Advance Fluid-APM Interface* option characterises the APM through two additional parameters, namely the *Interface Viscous Resistance* and the *Interface Reactance Coefficient*. The *Interface Viscous Resistance* introduces a pressure drop across the fluid-APM interface proportional to the incident acoustic velocity, while the *Interface Reactance Coefficient* imposes a pressure drop which is proportional to the time derivative of velocity. It is believed that the *Interface Reactance Coefficient* would help to account for the mass reactance term and thus, exploring the use of this option is justified.

Furthermore, it is worth mentioning that the results with the *Advance Fluid-APM Interface Modeling* option are dependent on the local voxel size at the fluid-APM interface. Thus to ensure high accuracy, the resolution in the vicinity of the interface has been increased by adding three VR regions in addition to those mentioned in section 6.2. The characterising parameters of the Acoustic Porous Medium used for the simulations in the current discussion are summarised in table 8.2. The parameters σ_v, ϕ and d in table 8.2 have been derived by applying the inverse algorithm while the *Interface Viscous Resistance* and the *Interface Reactance Coefficient* have been manually tuned to obtain the best possible match with the reference results.

Variable	Value	Unit
Viscous Flow Resistance (σ_v)	864.65	[1/s]
Porosity (ϕ)	0.589	[-]
Thickness (d)	38.1	[mm]
Interface Viscous Resistance	30.16	[m/s]
Interface Reactance Coefficient	1.35 x 10^{-4}	[m]

Table 8.2: APM parameters with Advanced Fluid-APM Interface Modeling

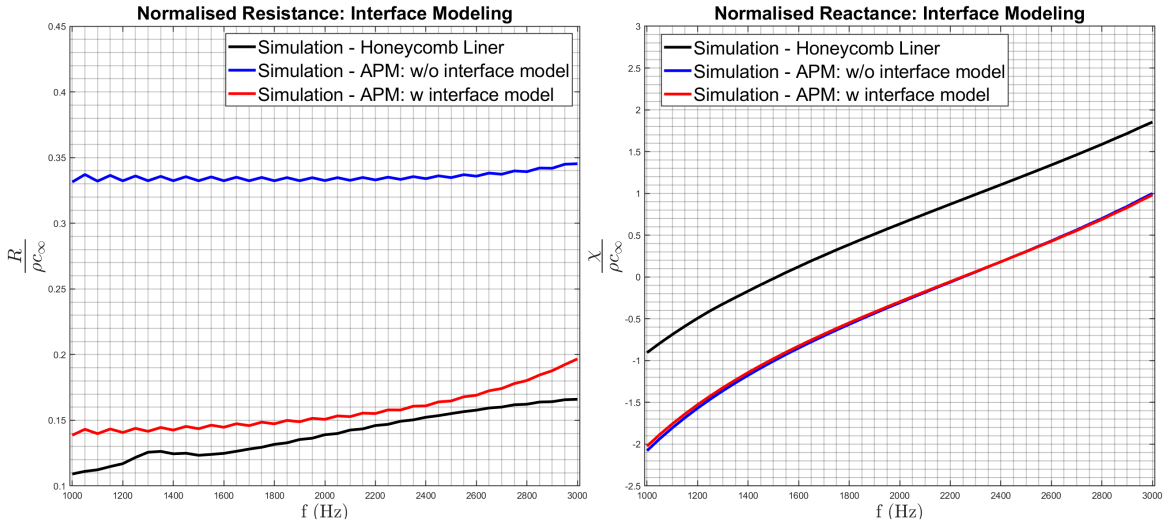

(a) Normalised Resistance

(b) Normalised Reactance

Figure 8.10: Normalised Impedance corresponding to the APM parameters derived with the Advanced Fluid-APM Interface Modeling option

Using the interface-modeling option with manually tuned *Interface Viscous Resistance* greatly improves the resistance prediction within the ROI, where the resistance value is within 5% - 10% of the honeycomb liner simulation case. On the other hand, similar to the cases discussed in previous sections, the normalised reactance is underpredicted in figure 8.10(b). In addition to this, hardly any difference is observed in comparison to the reactance obtained from simulations conducted without the interface modelling option. The fact that the interface modeling option barely influences the reactance curve suggests that the *Advance Fluid-APM Interface Modeling* is not able to account for the mass reactance term. This result is not expected as the Interface Reactance Coefficient term should be able to mimic the mass reactance effect. It could be possible that the value of Interface Reactance Coefficient mentioned in table 8.2 is too small to account for the mass reactance of the honeycomb liner used in the current study. However, the value of Interface Reactance Coefficient given in table 8.2 is its maximum allowable value in PowerFLOW® and thus, it could not be increased further.

9

Characterisation of APM through Pressure Drop Experiment

In the discussion presented in the previous chapter, the characterisation of the APM is dependent on the availability of a *priori* known impedance curve. However, in most cases the only thing known about a honeycomb liner are its geometric parameters. This poses a limitation on the use of inverse formulation. Under such conditions, it can be argued that the acoustic impedance of any liner can be obtained experimentally in an impedance tube such as that shown in figure 2.4. However, obtaining a *priori* impedance experimentally, just for the purpose of deriving the APM parameters, might be a time and a cost intensive affair. An alternative method to derive the characterising parameters of the APM is through a pressure drop experiment as explained in chapter 7. After the APM model parameters are obtained through the procedure illustrated in chapter 7, the simulations can be conducted and the impedance results can be analysed. The general methodology of the current approach is summarised in figure 9.1.

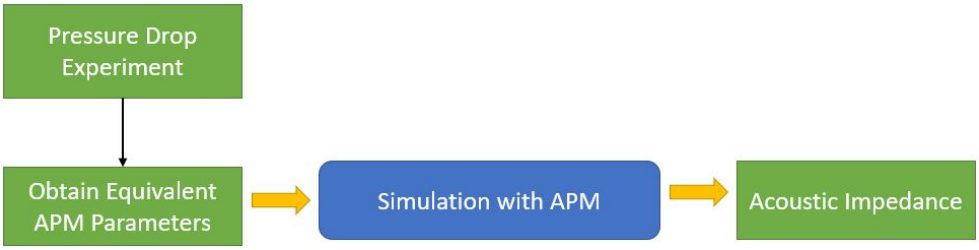

Figure 9.1: Methodology of APM simulations using the pressure drop experiments

The schematic of the impedance tube with the APM geometry used in the current chapter is shown in figure 9.2. In the present configuration, the perforated facesheet of the honeycomb liner is replaced with an APM region of the same thickness. Moreover, unlike the APM configuration employed in chapter 8, the honeycomb cavities are retained to enforce the locally-reacting assumption. In this sense, the current configuration is more 'physical' than that shown in figure 8.2(b)

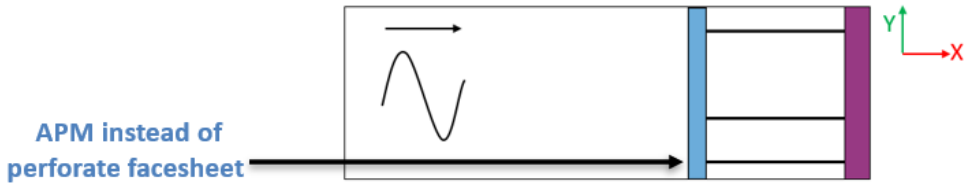

Figure 9.2: 2D Impedance tube with the APM replacing the perforated facesheet

9.1. Input Conditions

Unlike the inverse approach investigated in chapter 8, the current method uses the inertial flow resistance (σ_I) in addition to the viscous flow resistance (σ_v) to characterise the APM. These flow resistance are derived through the Darcy's method in chapter 7. The thickness (d) and the porosity (ϕ) of the APM are same as that of the perforated facesheet used in the pressure drop experiment, i.e. 0.64 mm and 0.064 respectively. Although the value of ϕ and d used in the current case is typical for perforated facesheets, it is improbable to imagine an actual porous material which has such low porosity and thickness. Thus, it could be possible that ϕ and d as low as that used in the current case is not a physical input for the APM model. This should be considered while analysing the results.

Variable	Value	Unit
Viscous Flow Resistance (σ_v)	13160.6	[1/s]
Inertial Flow Resistance (σ_I)	149556	[1/m]
Porosity (ϕ)	0.064	[-]
Thickness (d)	0.64	[mm]

Table 9.1: APM parameters derived through the pressure drop experiment

For details on the input acoustic signal, the reader is referred to table 5.1.

9.2. Bandpass-Filtered data

Figure 9.3 shows the bandpass-filter pressure fluctuations p' = p - p_∞ at different frequencies, for a probe located 1-voxel length upstream and downstream of the APM shown in figure 9.2. The corresponding normal velocity fluctuation is shown in figure 9.4. At the upstream location the maximum amplitude of pressure fluctuations are largely independent of the frequency. This is contrary to what is seen observed for the case shown in figure 8.3. Conversely, the relative amplitude at the two probe locations is frequency dependent with the amplitude downstream of the APM being lower than that at the upstream location. This drop in pressure can be attributed to the resistance offered by the APM to the incident acoustic signal. Similar to the pressure fluctuations, the normal velocity fluctuations in figure 9.4 hardly shows any variation with the change in frequency. Compared to this, the amplitude of normal velocity for the case of the honeycomb liner is more frequency dependent as seen from figure 8.6. Moreover, for the current case, the amplitude of normal velocity experiences no change across the APM as seen from the recordings at the two probe locations. This behaviour is explained by the fact the as the acoustic wave enters the APM, its velocity increases according to equation 4.14. Subsequently, it decreases as the wave exits the APM at the downstream end. Moreover, the thickness of the APM, i.e. d = 0.64 mm, might be too small for the Darcy's force term (equation 4.8) to impart any considerable effect and thus, no change is observed in the normal velocity across the APM.

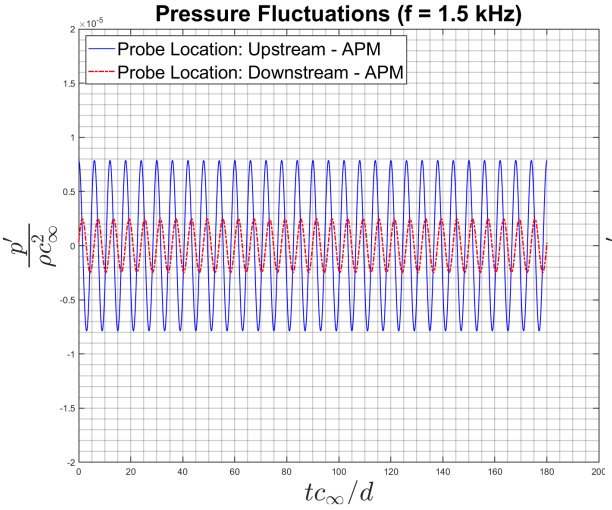

(a) f = 1.5 kHz

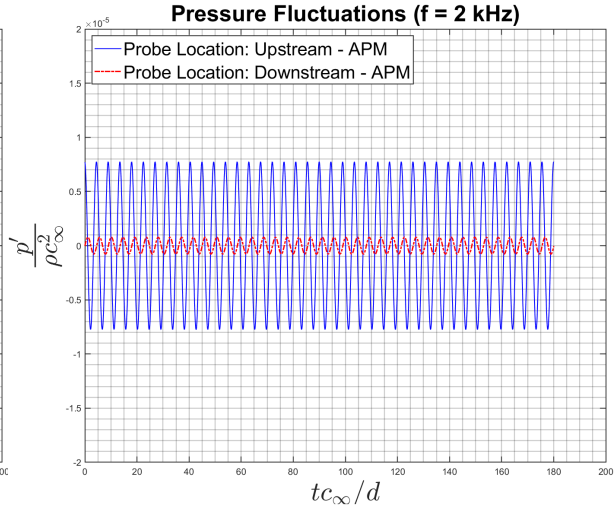

(b) f = 2 kHz

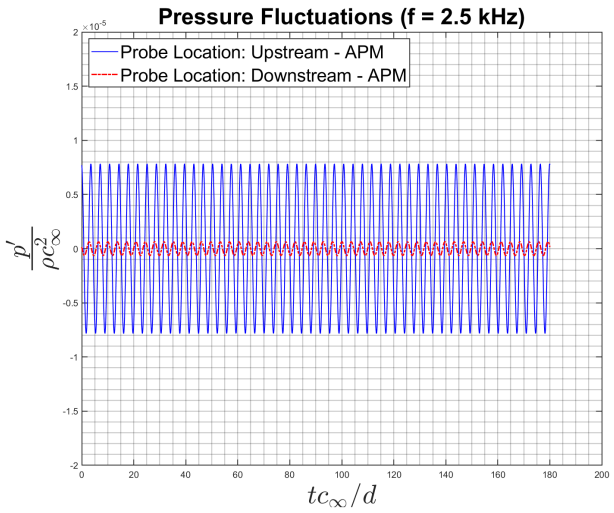

(c) f = 2.5 kHz

Figure 9.3: Pressure fluctuations upstream and downstream of the APM for different frequency

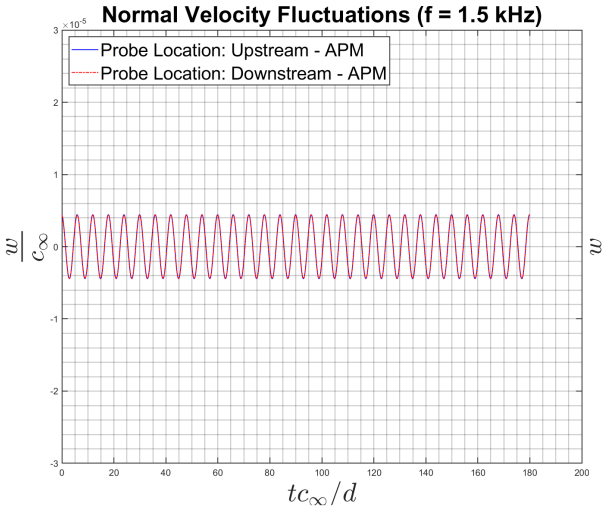

(a) f = 1.5 kHz

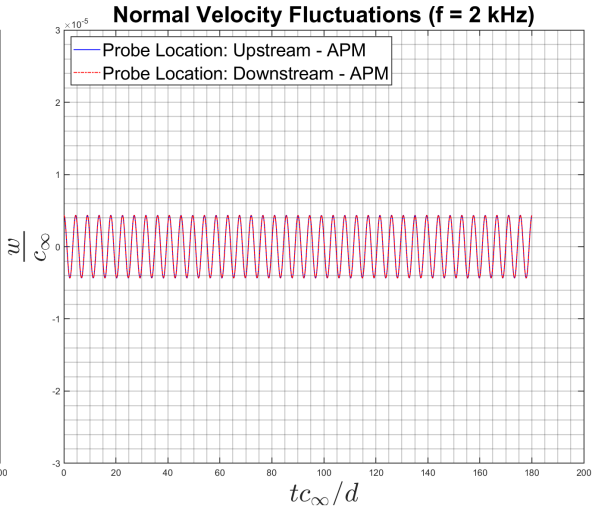

(b) f = 2 kHz

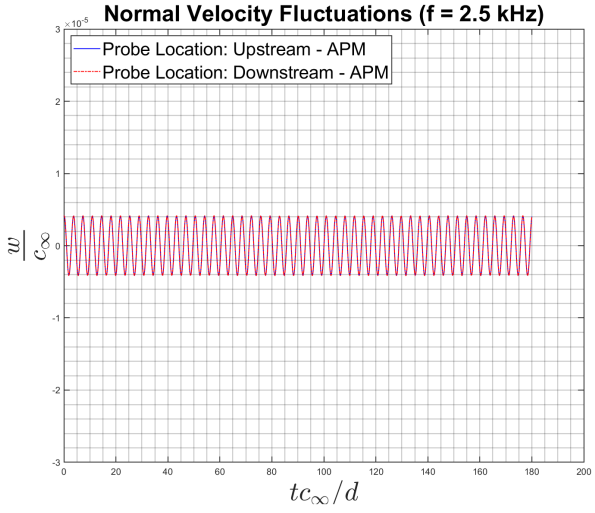

(c) f = 2.5 kHz

Figure 9.4: Normal velocity fluctuations upstream and downstream of the APM for different frequency

9.3. Comparison with experimental results

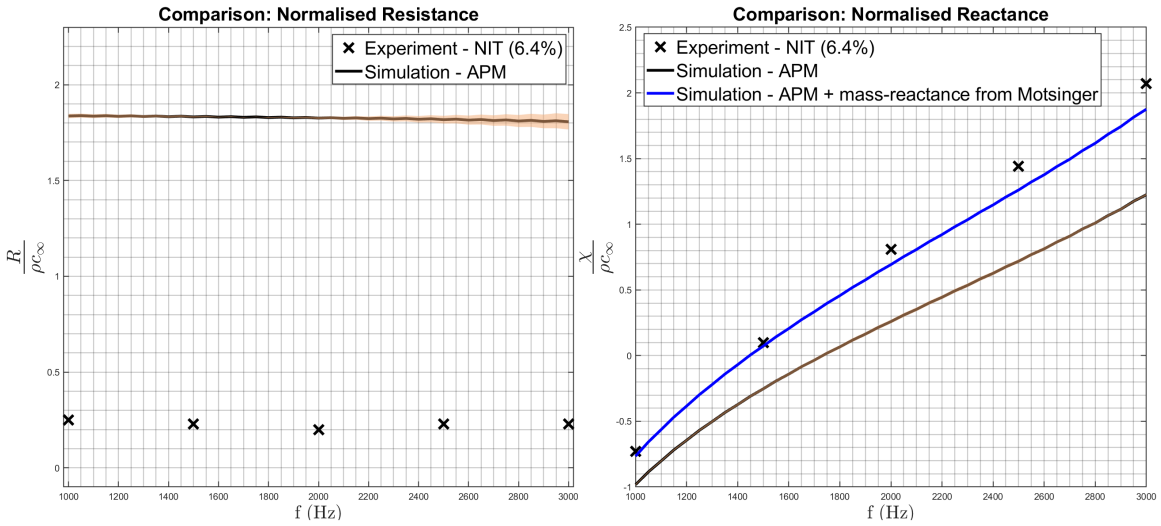

(a) Normalised Resistance (b) Normalised Reactance

Figure 9.5: Normalised Impedance corresponding to the APM parameters derived using pressure drop experiment

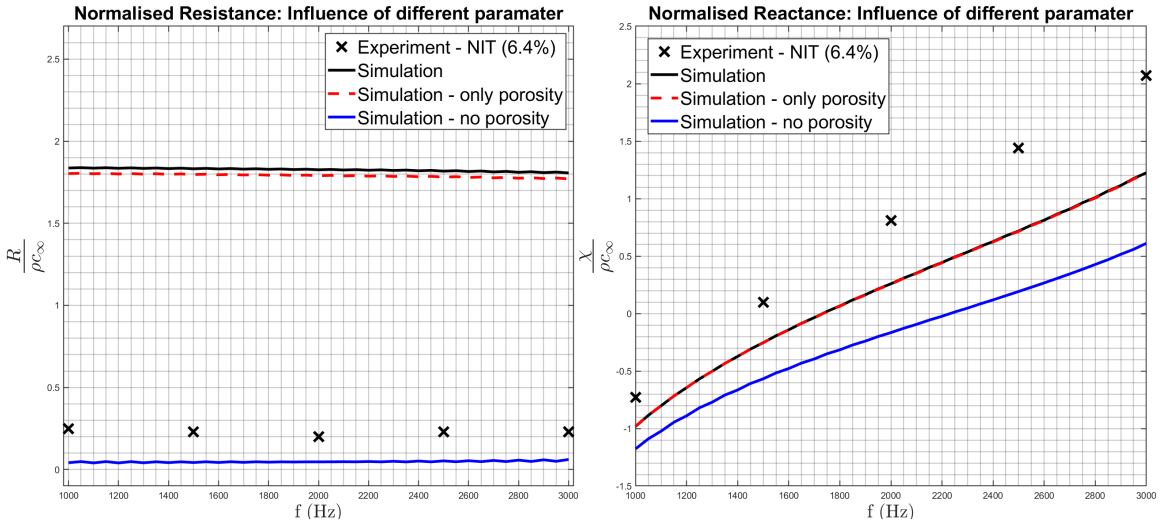

(a) Normalised Resistance (b) Normalised Reactance

Figure 9.6: Contribution of different terms to acoustic impedance

From figure 9.5(b), it can be seen that the normalised reactance values from the APM simulations underpredict the reference experimental results. The discrepency with respect to the reference curve increases from $\approx 30\%$ at f = 1 kHz to about 42% at f = 3 kHz. The reactance trend from the APM simulations can be explained by considering the configuration in figure 9.2 as a combination of an APM and an air-layer such as that discussed in Appendix C. The air-layer/ cavity of length 38.1 mm imparts a reactance in addition to that given by the APM of thickness 0.64 mm, which shifts the resonance to lower frequencies. This can be seen by comparing the simulation results from figure 9.5(b) with that from figure 8.8(b), where the APM of d = 38.1 mm backed by the solid backplate shows resonance at f = 2.25 kHz. Anyways, the reactance w.r.t the experimental results is still underpredicted. However, when the the analytical mass-reactance from equation 2.15 is added to the reactance from the APM simulations, a favourable match is achieved with the reference experimental results. This results shows the inability of the APM to account for the mass-reactance for the current liner.

Next, the normalised resistance trends are given in figure 9.5(a). It is seen that the resistance curve from the simulations predicts a value which is much higher than that given by the reference case. The *Experiment - NIT(6.4%)* resistance fluctuates between a value of 0.20 - 0.25, while the simulations predicts a value of ≈1.83, which is almost constant over the frequency ROI.

To investigate the cause of the resistance trend, two sets of simulations were conducted with the APM configuration shown in figure 9.2.

- In the first simulation, the value of σ_v and σ_I are kept equal to zero, while the value of ϕ is maintained at 0.064. This will help to understand the contribution of the APM porosity to the acoustic resistance.
- In the second simulation, the value of σ_v and σ_I are taken from table 8.3, while the value of ϕ is changed to 1.

The results from the above mentioned simulations are shown in figure 9.6. In the figure, 'Simulation' corresponds to the case presented figure 9.5 while *Simulation-only porosity* and *Simulation-no porosity* represent the cases mentioned in the aforementioned points respectively. For simulations with *no porosity*, the normalised acoustic resistance is constant over the entire frequency range at a value of 0.04. Although this value is much lower than the resistance from the reference curve, this result is expected as the effect of ϕ is completely neglected. A strange trend however, is seen for the simulations with *only porosity* input. The resistance for *only porosity* simulations is 1.79 which is almost equal to the normalised resistance of about 1.83 derived for simulations with all the parameters. This suggests that the resistance in the current case is caused entirely by ϕ and not by σ_v or σ_I.

As mentioned in chapter 6, in addition to the Darcy's force term the APM-interface imposes an interface resistance which is a function of ϕ as mentioned by Sun et al. [65]. The fact that extremely high resistance values are observed for *only porosity* inputs hints at the fact that the interface resistance dependence on porosity might not be appropriate to model the acoustic resistance in the current case. Another reason for this trend can be explained by the fact that the input of ϕ = 0.064 and d = 0.64 mm might not be 'physical' for the APM model as mentioned in section 9.1. However, this cannot be said for certain with the current set of results and further studies would be required to confirm this hypothesis.

9.4. Advanced Fluid-APM Interface Modeling

It is suggested that the overprediction of the acoustic resistance seen in figure 9.5 might caused by the interface resistance term which is the function of the APM porosity ϕ. With the *Advanced Fluid-APM Interface Modeling* option, this interface resistance can be chosen manually and its dependence on the input porosity can be bypassed.

Thus, in the current section, the *Advanced Fluid-APM Interface Modeling* is used and the *Interface Viscous Resistance* is manually tuned to 40 m/s to obtain the best possible match with the reference result. In addition to this, the maximum allowable value of 0.000135 m is chosen for the *Interface Reactance Coefficient*. The impedance curves are shown in figure 9.7 where the JCA-EF represents the results from the Jonhson-Champoux-Allard model which is an equivalent fluid introduced in section 3.2.1.

The normalised resistance curve shown in figure 9.7(a) shows that by manually tuning *Interface Viscous Resistance*, the impedance match with reference experimental result can be greatly improved. Thus, it is probable that the dependence of interface resistance on the input porosity might not be fit for mimicking the acoustic effects of the liner being analysed in the current thesis. Besides this, the JCA-EF model underpredicts the resistance w.r.t the reference result. The reason for the underprediction is attributed to the fact that the current model is unable to account for take the effect of the in-orifice velocity on the acoustic resistance (see equation 3.7), which is quite important for the present excitation level as shown in section 5.6.4.

On the other hand, the JCA-EF model gives a better prediction of the reference normalised reactance values than the APM simulations as seen from figure 9.7(b). This is probably because the mass reactance term is much better predicted in the case of by the JCA-EF model (see equation 3.7), contrary to the APM simulation.

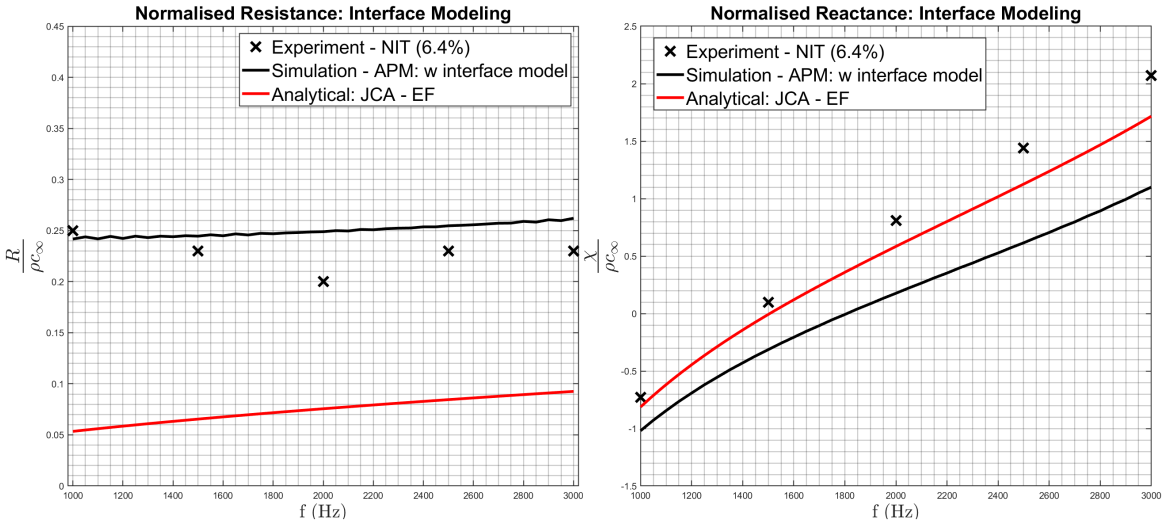

(a) Normalised Resistance

(b) Normalised Reactance

Figure 9.7: Normalised Impedance educed with Advanced Fluid-APM Interface Model

IV

Conclusions and Recommendations

10

Conclusions and Recommendations

In the current thesis, the APM model, which is an equivalent fluid fluid formulation present in the LB based solver PowerFLOW®, is used to mimic the acoustic effects of a honeycomb liner. To realise the objective of the current thesis, a sequential approach is adopted. Firstly, a verification study of the honeycomb liner-CFD setup is conducted, where the impedance spectra from the numerical simulations is compared with the experimental and numerical results present in the state of the art. This verification activity helps in commenting on the efficacy of the simulation parameters. Thereafter, implementation of the APM formulation is verified by reproducing the acoustic effects of the $CT73$ ceramic tubular liner. Following this, a detailed discussion on the pressure drop experiment, which is treated as a probable method to characterise the APM is presented. Finally, the capability of the APM formulation for mimicking the effects of the honeycomb acoustic liner is analysed by comparing its impedance spectra with that from the experimental and theoretical results.

10.1. Conclusions

The work done in the current thesis is essentially discussed in five chapters, from chapter 5 to chapter 9. Chapter 2 and chapter 3 on the other hand, provide only with the background knowledge which aids in the analysis of the work done in this thesis. Thus, in the current section, major conclusions are presented chapter wise, starting from chapter 5 - chapter 9.

1. Chapter 5 presents a verification study of the DNIT setup with the honeycomb liner geometry. It is observed that the simulation results underpredict the normalised resistance and the normalised reactance values from the results mentioned in the state of the art. The discrepancy observed in the values of normalised resistance especially can be as large as 50% in some cases. This trend is not expected and thus, a small verification activity is conducted to check the dependence of the impedance spectra on the simulation parameters. The outcomes of this study are as follows:
    - The numerical setup does not introduce any spurious phenomenons which is confirmed from numerical simulations without liner geometry. This ascertains the correct implementation of the boundary conditions.
    - The impedance trends are independent of the impedance eduction method.
    - The trends observed for the simulations with different waveguide diameter do not explain the aforementioned underprediction of the normalised impedance.
    - Contrary to a broadband signal used in the current study, the liner is simulated with a tonal input in the current step. It is observed that the flow non-linearities, which are prevalent at the OASPL of 130 dB are not predicted from simulations with the broadband excitation. With an underprediction of non-linearities, the acoustic resistance spectra is bound to be underpredicted. On the other hand, a comparatively favourable match is observed with the reference results for the case with the tonal excitation. This result demonstrates that the effect of source type, i.e. broadband or tonal, must be taken intro account while analysing the liner.

2. In chapter 6, the use of the current numerical setup with the APM is verified. Results show that the APM is able to reproduce the effects of the $CT73$ liner and that the impedance results exactly match the numerical results of Sun et al. [65]. Thus, it can be concluded the APM implementation with the current numerical setup is correct and it's use can be extended to other cases, such as reproducing the acoustic impedance trends of the honeycomb liner.

3. The procedure for obtaining the flow resistance for characterising the APM through a pressure-drop experiment is discussed chapter 7. Using Darcy's law to relate the pressure drop values with the flow resistances, a value of σ_v = $13160.6\ Ns/m_4$ and σ_l = $149556\ m^{-1}$ is obtained. A small verification activity in the chapter has raised doubts on the use of Darcy's law for relating the pressure drop values with the flow resistance of a perforated plate. This stems from the fact that Darcy's law is derived for a porous material and thus, it might not be fit for use in the current case where a perforated facesheet is being analysed. Following this, the results from Darcy's law is compared with the Kraft's model, which is based on the geometric parameters of a perforated facesheet. Comparison shows that different flow resistance values are obtained for both these models.

4. The final step in the current thesis is to use the APM formulation to mimic the honeycomb liner's acoustic effects. In chapter 8, the APM analysed with the parameters derived through the inverse algorithm present in PowerFLOW® and the main outcomes of this study are as follows:

    - The inverse approach completely overlooks the structural difference between the liner and the APM. In doing so, the locally reacting assumption is not satisfied and thus, this representation might not be entirely physical. However, it should be noted that the effect of this limitation could not be quantified in the current study.
    - Characterising APM through the flow resistance (σ), the thickness (d) and the porosity (ϕ) only might not be adequate to model the honeycomb liner effects. This is because of the inability of the APM to account for the mass reactance effects. However, it should be noted that this conclusion is specific to the current liner. The liner used in this thesis has a facesheet t_f/d_o < 1, and for such liners the mass-reactance can be quite significant [49]. For facesheets with t_f/d_o>1 and for wire-meshes, the mass reactance is comparatively lower. Thus, the APM might be able to mimic the effects of such liners with σ, d and ϕ only.
    - The addition of *Advance Fluid-APM Interface Modeling* option, which uses two extra parameters to characterise the liner, is not able to improve the prediction of the acoustic reactance spectra. This trend is not expected as the additional term *Interface Reactance Coefficient* should be able to model the mass reactance effect. It could be possible that the threshold for this term in the current APM implementation is too small to account for mass reactance for the present liner.

5. In chapter 9 the APM is characterised using the pressure drop experiment. The major conclusions from this study are as follows,

    - Like the approach discussed in chapter 8, the accurate prediction of the acoustic reactance spectra remains a bottleneck. This again stems from the fact that the mass-reactance effect of the reference liner are not predicted by the APM formulation.
    - The acoustic resistance spectra is much higher than that from the reference results. This overprediction has raised doubts over the efficacy of the APM formulation at low porosities, such as ϕ = 0.064 in the current case. It is also possible that such low porosity is not a physical input for the APM model, as it is improbable to imagine an actual porous material with such low porosity. In this case, the straightforward approach of inputting the liner porosity as the facesheet porosity might be incorrect. However, further investigation is required to ascertain the APM performance at such low porosities.

On the whole, it can be said that some modifications/ improvements are required in the current implementation of the APM formulation to replicate the performance of the honeycomb liner used in the current thesis. With the present APM implementation, it might still be possible to emulate the acoustic effects of some other liners, however further research is required to say this with certainty.

10.2. Recommendations for Future Work

Based on the work done in the current thesis and the major conclusions drawn from it, the certain recommendations for the future work are outlined in the current section:

- Through the current study, it has been seen that for non-linear liner operations, the broadband and tonal input cannot be used interchangeably. Thus, in the future studies, the effect of the input source type, on the acoustic effects of the liner must be taken into account.
- Without the *Advanced Fluid-APM Interface Modelling* option, i.e. when the APM is characterised using σ, ϕ and d only, the mass reactance for the current liner cannot be accounted for the current liner. However for other liners, such as the cavity backed wire meshes/ liners with t_f/d_o > 1, the mass reactance is comparatively subtle. Therefore, it would be interesting to implement the APM with the aforementioned parameters only, to reproduce the effects of such liners.
- Two different pressure drop models were employed in the current thesis, namely i) the method based on Darcy's law and ii) that based on Kraft's formulation. Different values of flow resistance were obtained by employing both these models on the same pressure drop data. In future simulations, the performance of APM with parameters obtained from both these models can be compared. This could give insight into which model is better for representing the pressure drop for a perforated plate.
- When using *Advanced Fluid-APM Interface Modelling*, the user is given an option to input the *Interface Reactance Coefficient* which should be able to account for the mass reactance of a traditional honeycomb liner. However, this is not observed in the current thesis and thus, future efforts should be dedicated to tackle the discrepancy associated with the this term. This would probably improve the robustness of the current formulation.
- The overprediction of the normalised resistance by the APM, at porosity of ϕ = 0.064 has raised doubts on the performance of APM at such small porosities. Therefore, there is a need to analyse the performance of APM with low input porosities, especially at ϕ < 0.2, as these are typical for honeycomb liners.
- Previous studies have shown that the APM is able to reproduce the experimental pressure drop values for a porous material. However, these materials had a porosity ϕ > 0.9. Considering that discrepancies in the impedance spectra is observed for an input APM porosity of 0.064, it make sense to check if the APM is able to reproduce the pressure drop curve seen in chapter 7.

V

Appendix

A

Derivation of Impedance for Helmholtz Resonator

In the following chapter, the expression for the acoustic impedance of a Helmholtz resonator given in equation 2.6 is derived. The derivation start from the lumped element analogy illustrated in figure 2.2. Starting from the free body diagram given in figure 2.2(b), the force balance equation can be written as,

$$-F = Ma + R_n v + sz \tag{A.1}$$

where Ma is the mass inertia from Newton's second law of motion and F is the external force exerted by the incoming signal. $R_n v$ is the damping proportional to the velocity in the neck and sz is the spring stiffness given by Hooke's law. As mentioned in section 2.1, the air inside the cavity neck oscillates when excited by an incoming acoustic signal. Thus, the displacement z of this mass M_n is given as,

$$z = z \cdot e^{i\omega t} \tag{A.2}$$

Differentiating the above equation gives the velocity in the neck.

$$v = \frac{dz}{dt} = i\omega z \tag{A.3}$$

$$z = \frac{v}{i\omega} \tag{A.4}$$

Subsequently, the acceleration of the mass M_n can be derived as,

$$a = \frac{d^2 z}{dt^2} = i\omega \frac{dz}{dt} = i\omega v \tag{A.5}$$

Substituting the above expression in equation A.1 gives the following expression for the force balance equation,

$$-F = Mi\omega v + R_n v + \frac{1}{i\omega} sv \tag{A.6}$$

$$-F = v\left(Mi\omega + R_n + \frac{1}{i\omega} s\right) \tag{A.7}$$

$$-F = v\left(Mi\omega + R_n - \frac{i}{\omega} s\right) \tag{A.8}$$

Using the definition of the acoustic pressure p, i.e. $p = F/S_n$ in equation the impedance of the Helmholtz resonator is given as,

$$Z = \frac{-F}{S_n v} = \frac{i\omega M + R_n - \frac{is}{\omega}}{S_n} \tag{A.9}$$

B

Effect of APM porosity on APM performance

Simulations are conducted with three different values of APM porosity, i.e at ϕ = 0.52, at 0.57 and at 0.62. Other APM parameters, i.e. σ_v and (d) are chosen from table 8.1. It is seen from figure B.1 that changing ϕ has no effect on the value of resonance frequency f_o. The only visible effect is that the reactance scales with ϕ, in accordance with the formula of cavity reactance, i.e. -ιcot$(kd)/\phi$.

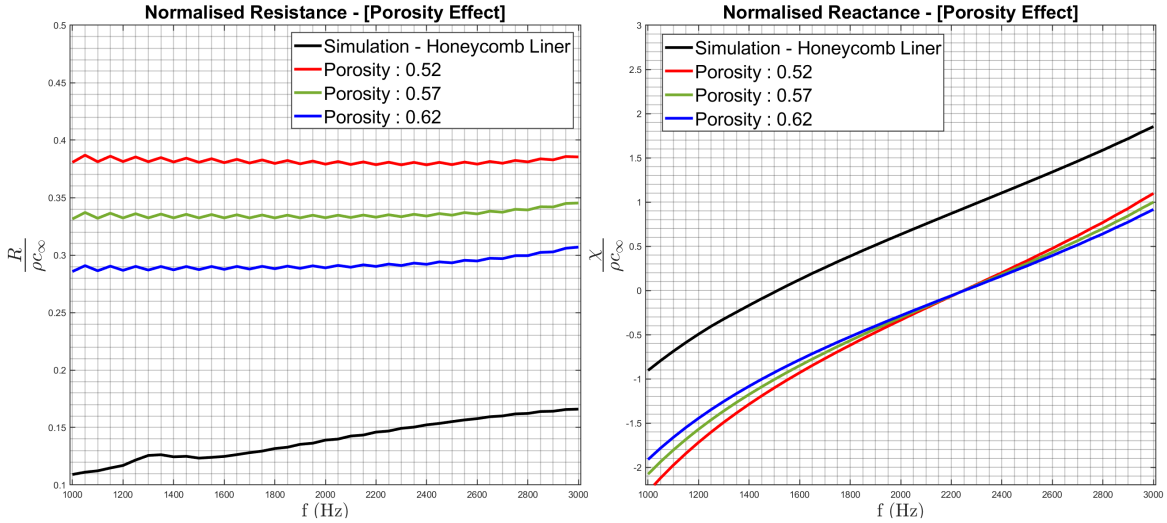

(a) Normalised Resistance

(b) Normalised Reactance

Figure B.1: Effect of APM porosity on the acoustic effects of the Acoustic Porous Medium

Furthermore, figure B.1(a) shows that the resistance value is higher for a lower value of ϕ. This effect can be explained through equation 4.14. From this equation, it can be inferred that a lower value of ϕ would cause a larger increase in the value of inside the APM for the same incident acoustic wave. This is seen from figure B.2 where a 47% increase in the amplitude of normal velocity is seen for ϕ = 0.52 compared to only a 35% increase for ϕ = 0.62. Consequently, a larger in-APM acoustic velocity would increase the Darcy's force term (from equation 4.8) and hence, a higher value of acoustic resistance will be observed. This explains the increase in acoustic resistance with the decrease in ϕ that is seen in figure B.1(a).

The discussion in the current section shows that by changing the value of ϕ, the acoustic resistance can be shifted to achieve a better match with the reference *Experiment - NIT(6.4%)* result. However, this is futile as the prediction of normalised reactance cannot be improved.

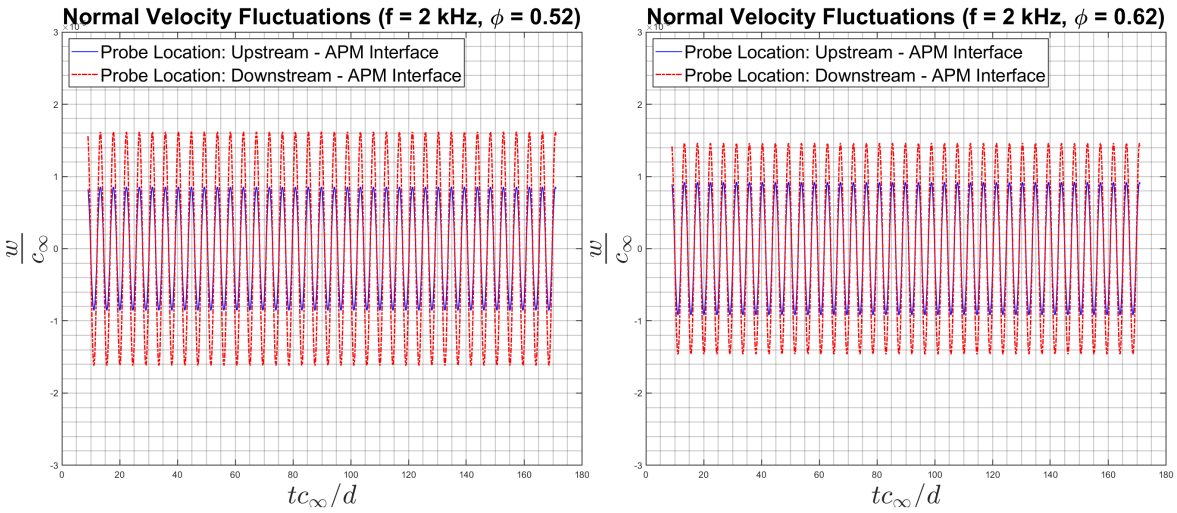

(a) ϕ = 0.52 (b) ϕ = 0.62

Figure B.2: Comparison of normal velocity jump at APM interface for different porosity at f = 2 kHz

C

Effect of Air-layer on APM performance

The current study seeks to analyse the effect of introducing an air-layer (e) between the APM and the solid backplate in the DNIT. This configuration is illustrated in the 2D schematic shown in figure C.1. With an air layer-APM combination, Perot et al. [51] were able to improve the performance of the APM for mimicking the acoustic effects of porous materials. Thus, it is interesting to see if the same can be achieved for a honeycomb liner

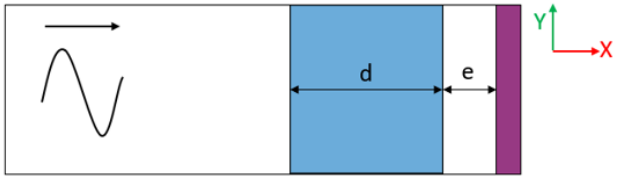

Figure C.1: Schematic of DNIT setup with an air-gap between the APM and the solid backplate

Three different cases are simulated in the current discussion, namely with an air-gap thickness e = 0 mm, 2.5 mm and 5 mm respectively. Besides this, other characterising APM parameters are taken from table 8.1. At e = 0, the acoustic reactance is almost independent of the frequency within the current ROI. As the value of e increases the resistance increases almost quadratically at higher frequency, with this effect being most prominent at a e = 5 mm. A reason for this trend can be explained through figure C.3, where the impedance have been plotted in the range of 1 kHz - 5 kHz. It is seen that, increasing the air-layer thickness shifts the anti-resonance frequency, and consequently the entire resistance curve towards lower frequencies. The fact that the anti-resonance peak moves closer to the value of 3 kHz for e = 2.5 and 5 mm explains the sudden rise in the resistance values seen at higher frequencies in figure C.2(a). Similar trends are observed for normalised reactance spectra.

This shift of the impedance spectra can be explained by comparing the configuration shown in figure C.1 to that shown in figure 8.2(a). Just as an honeycomb cavity of a length L contributes to the total liner reactance, the air-gap e in case of an APM figure C.1 imparts additional reactance to the APM of thickness d and porosity ϕ. Anyways, the only visible effect of introducing the air-layer is the shift of the resistance and reactance curve towards lower frequencies. Clearly, this doesn't improve the match with the reference results.

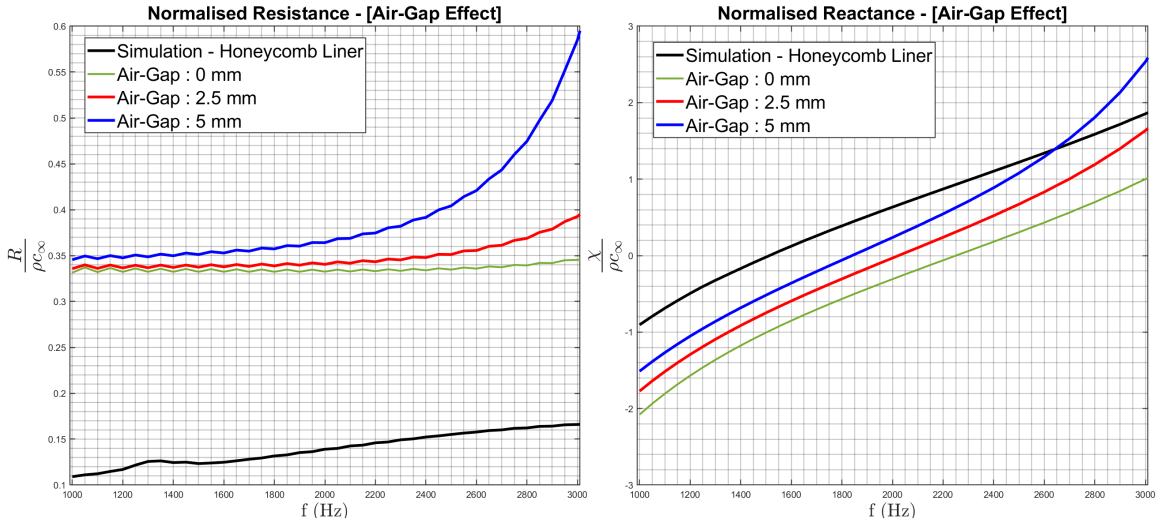

(a) Normalised Resistance (b) Normalised Reactance

Figure C.2: Effect of APM porosity on the acoustic effects of the Acoustic Porous Medium

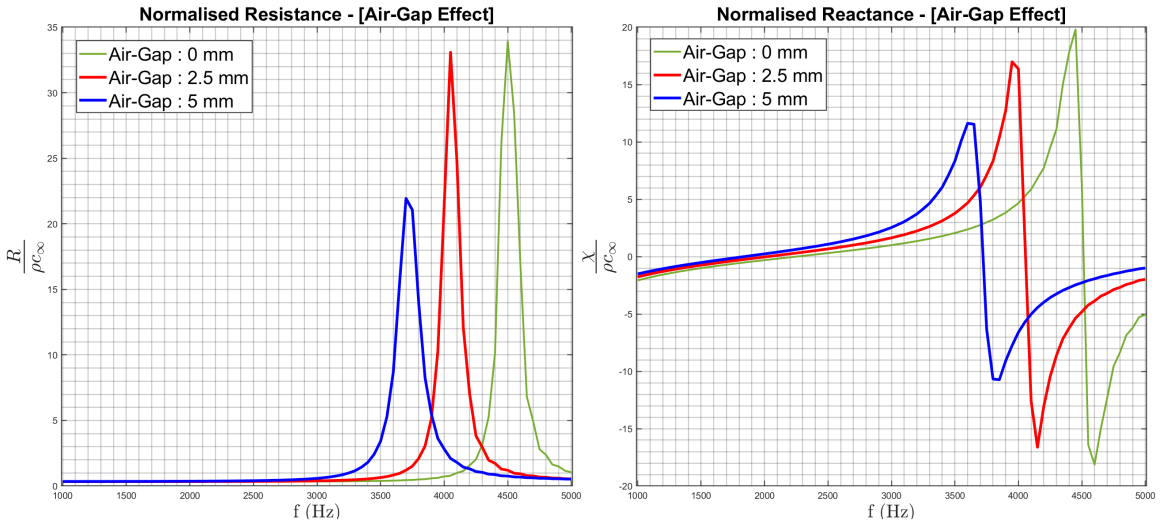

(a) Normalised Resistance (b) Normalised Reactance

Figure C.3: Impedance curves for changing air-layer thickness in frequency range of 1 kHz- 5 kHz

D

Near/ In-orifice Streamlines

Near/ In-Orifice Streamlines

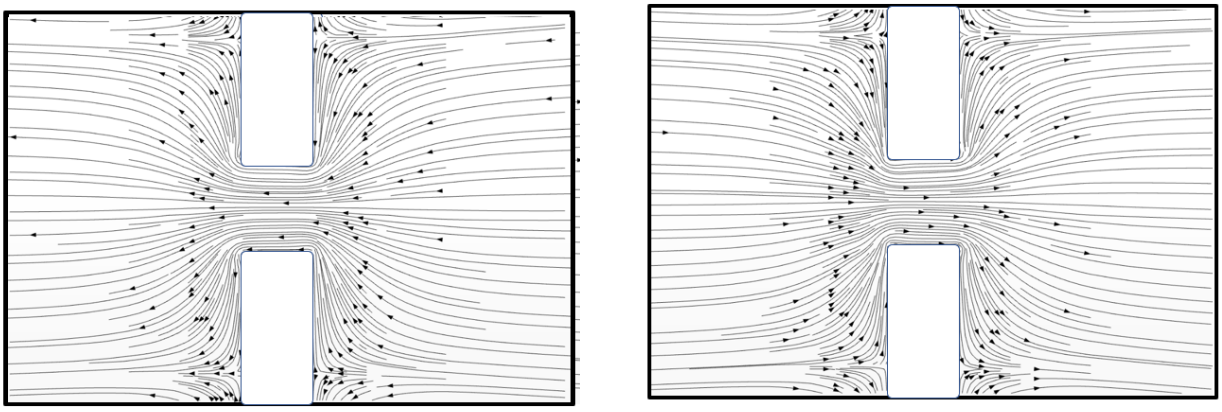

(a) $\theta = 0$

(b) $\theta = \pi$

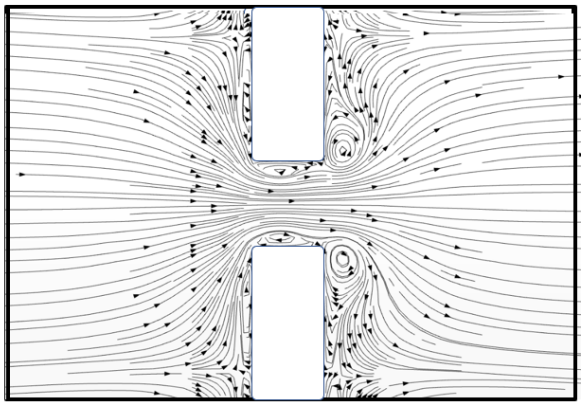

(c) $\theta = 3\pi/2$

Figure D.1: Phase averaged streamlines for input broadband signal

E

Extra Plots from APM Simulation

Pressure fluctuations across APM for different frequency (Parameters derived through pressure drop experiment)

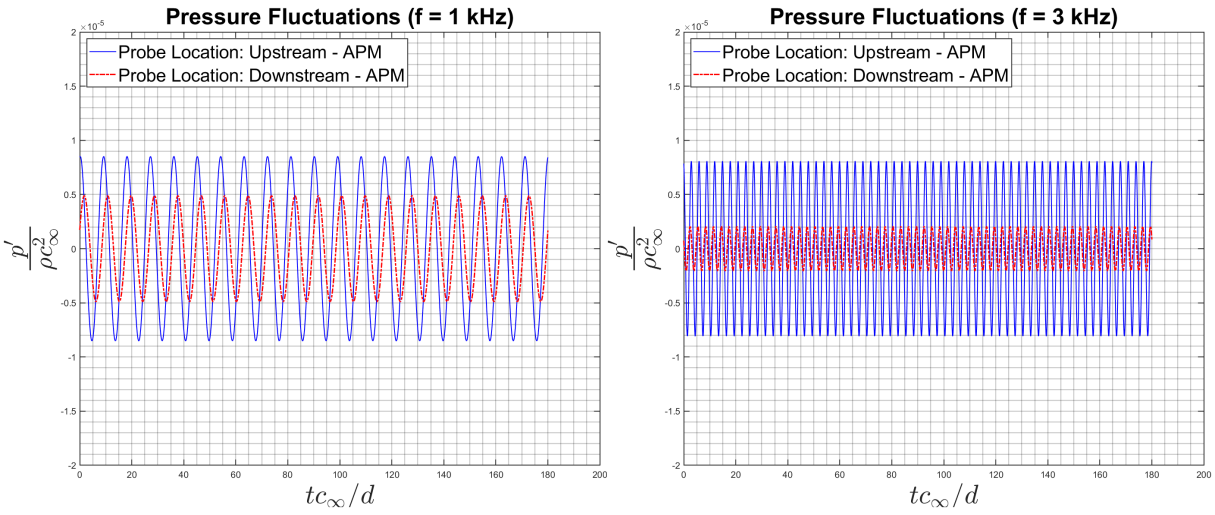

(a) f = 1 kHz (b) f = 3 kHz

Figure E.1: Pressure jump across APM for different frequency

Normal Velocity jump at APM interface for different porosity (inverse method)

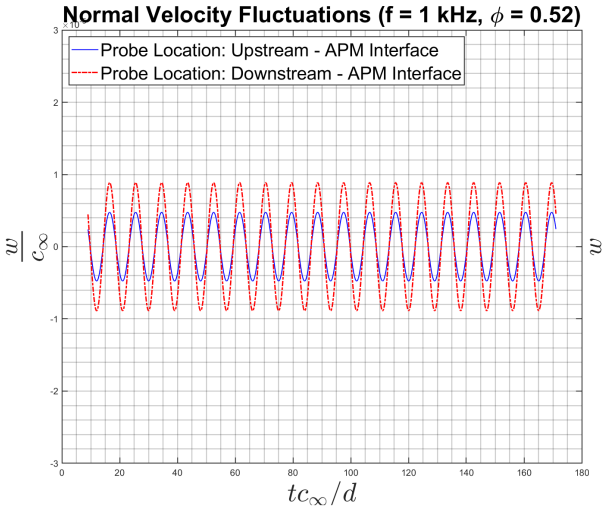

(a) ϕ = 0.52, f = 1 kHz

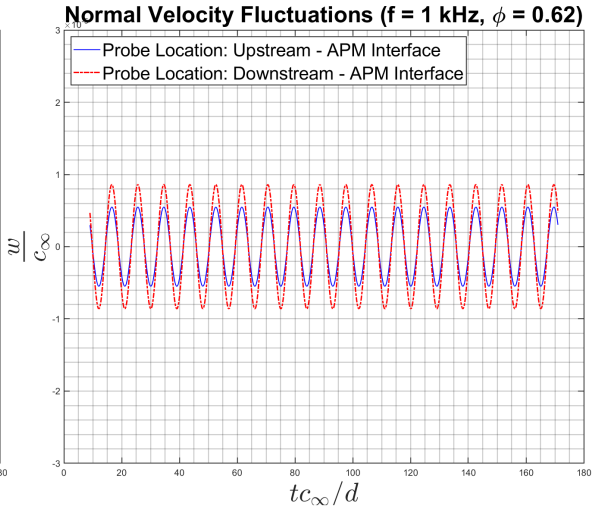

(b) ϕ = 0.62, f = 1 kHz

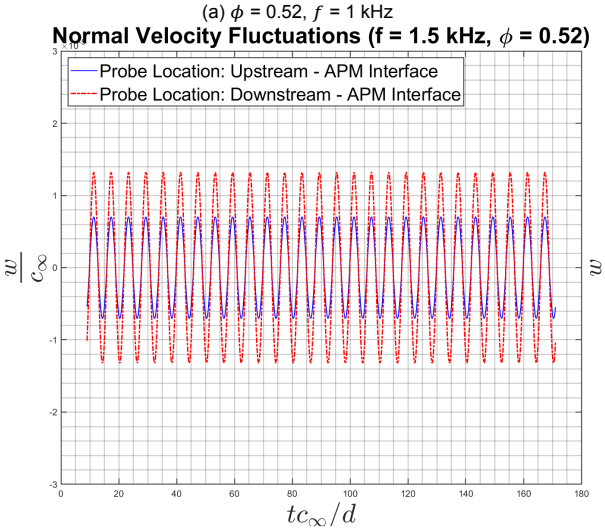

(c) ϕ = 0.52, f = 1.5 kHz

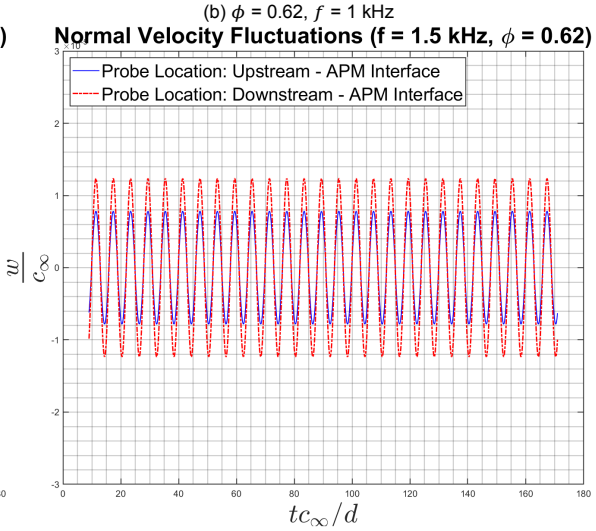

(d) ϕ = 0.62, f = 1.5 kHz

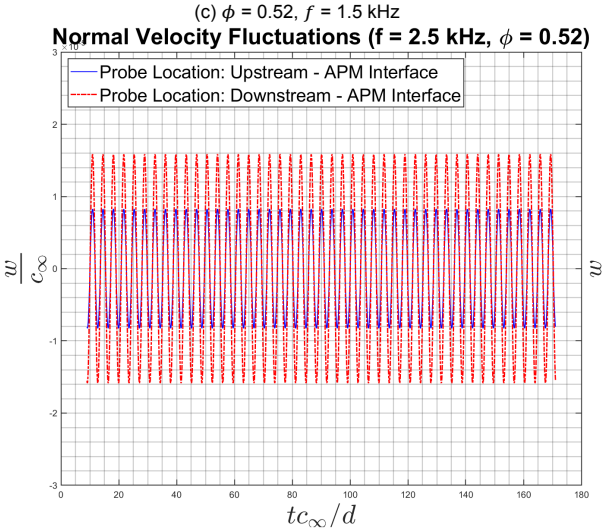

(e) ϕ = 0.52, f = 2.5 kHz

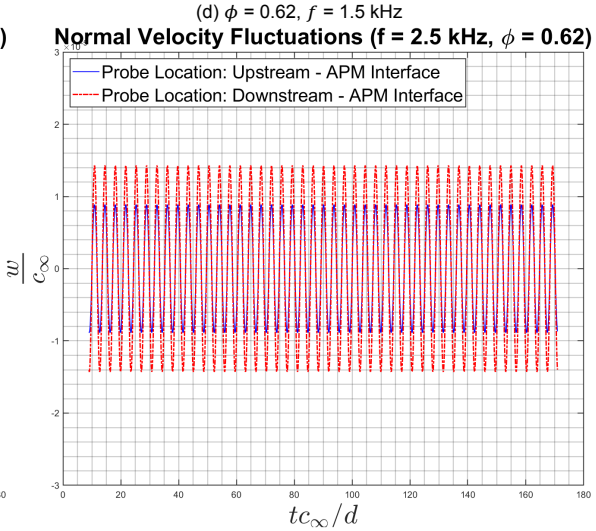

(f) ϕ = 0.62, f = 2.5 kHz

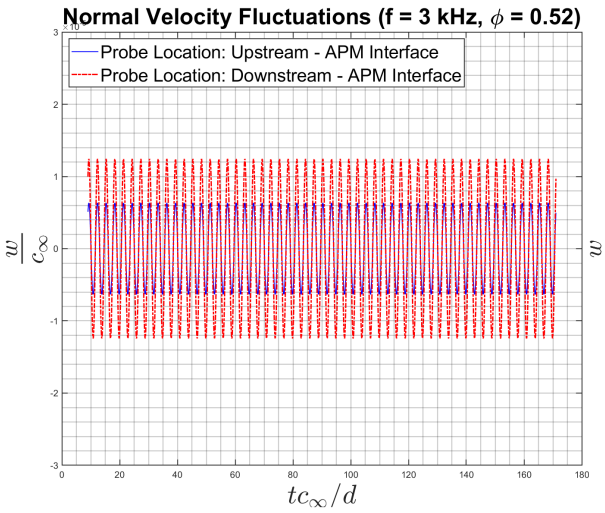

(g) ϕ = 0.52, f = 3 kHz

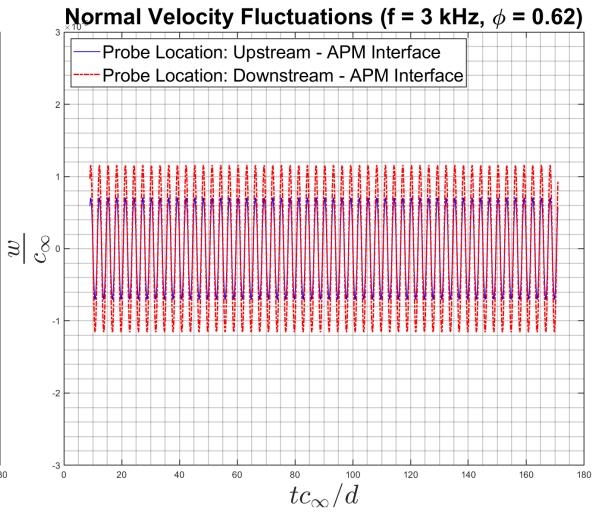

(h) ϕ = 0.62, f = 3 kHz

Figure E.2: Comparison of normal velocity jump at APM interface for different porosities at different frequencies

Bibliography

[1] Easa certification noise levels.

[2] Acoustic liners for quieter aero-engines. https://cordis.europa.eu/article/id/157727-acoustic-liners-for-quieter-aeroengines, 2017.

[3] Mohamed Ammar Abbassi and Jamel Orfi. Effects of magnetohydrodynamics on natural convection and entropy generation with nanofluids. *Journal of Thermophysics and Heat Transfer*, 32(4): 1059–1071, 2018.

[4] Jean Allard and Noureddine Atalla. *Propagation of sound in porous media: modelling sound absorbing materials 2e*. John Wiley & Sons, 2009.

[5] Kempton. Andrew. Acoustic liners for modern aero-engines, presentation slides (rolls-royce plc). 2011.

[6] Noureddine Atalla and Franck Sgard. Modeling of perforated plates and screens using rigid frame porous models. *Journal of sound and vibration*, 303(1-2):195–208, 2007.

[7] Yuanxun Bill Bao and Justin Meskas. Lattice boltzmann method for fluid simulations. *Department of Mathematics, Courant Institute of Mathematical Sciences, New York University*, page 44, 2011.

[8] Prabhu Lal Bhatnagar, Eugene P Gross, and Max Krook. A model for collision processes in gases. i. small amplitude processes in charged and neutral one-component systems. *Physical review*, 94(3):511, 1954.

[9] Edward Brambley. Review of acoustic liner models with flow. 2012.

[10] Markus O Burak, Mattias Billson, Lars-Erik Eriksson, and Stéphane Baralon. Validation of a time- and frequency-domain grazing flow acoustic liner model. *AIAA journal*, 47(8):1841–1848, 2009.

[11] A Rubio Carpio, R Merino Martinez, Francesco Avallone, Daniele Ragni, Mirjam Snellen, and Sybrand van der Zwaag. Broadband trailing edge noise reduction using permeable metal foams. In *Proceedings of the INTER-NOISE and NOISE-CON Congress and Conference Proceedings*, page 2755, 2017.

[12] Damiano Casalino. Optydb toolkit-user manual, version 2.0. *Dassault Systemes*, 2020.

[13] Yvan Champoux and Jean-F Allard. Dynamic tortuosity and bulk modulus in air-saturated porous media. *Journal of applied physics*, 70(4):1975–1979, 1991.

[14] Hudong Chen, Shiyi Chen, and William H Matthaeus. Recovery of the navier-stokes equations using a lattice-gas boltzmann method. *Physical review A*, 45(8):R5339, 1992.

[15] Lingfeng Chen, Lin Du, Xiaoyu Wang, Xiaodong Jing, and Xiaofeng Sun. A three-dimensional straightforward method for liner impedance eduction in uniform grazing flow. *Journal of Sound and Vibration*, 468:115119, 2020.

[16] Dassault Systèmes Simulia Corp. Powerflow 6-2019 powercase user's guide. 2020.

[17] I.B Crandall. *Theory of vibrating systems and sound*. 1954.

[18] Xiwen Dai and Yves Aurégan. Acoustic of a perforated liner with grazing flow: Floquet-bloch periodical approach versus impedance continuous approach. *The Journal of the Acoustical Society of America*, 140(3):2047–2055, 2016.

[19] PD Dean. An in situ method of wall acoustic impedance measurement in flow ducts. *Journal of Sound and Vibration*, 34(1):97–IN6, 1974.

[20] Aa Bart.van der. Ground buried resonators analytical and numerical modelling of their noise reducing effect for sound propagating outdoors from traffic noise sources. 2012.

[21] Tamer Elnady and Hans Boden. On semi-empirical liner impedance modeling with grazing flow. In *9th AIAA/CEAS Aeroacoustics Conference and Exhibit*, page 3304, 2003.

[22] K Gao. *Multiscale modelling of acoustic porous materials*. PhD thesis, PhD thesis, Technische Universiteit Eindhoven, 2016.

[23] Lorna J Gibson and Michael F Ashby. *Cellular solids: structure and properties*. Cambridge university press, 1999.

[24] Kaveh Habibi and Luc Mongeau. Prediction of sound absorption by a circular orifice termination in a turbulent pipe flow using the lattice-boltzmann method. *Applied Acoustics*, 87:153–161, 2015.

[25] AS Hersh and B Walker. Acoustical behavior of homogeneous bulk materials. In *AIAA 6th aeroacoustics conference, Hartford, CN*, 1980.

[26] Derek B Ingham and Ioan Pop. *Transport phenomena in porous media*. Elsevier, 1998.

[27] U. Ingård and S. Labate. Acoustic circulation effects and the nonlinear impedance of orifices. *The Journal of the Acoustical Society of America*, 22(2):211–218, 1950. doi: 10.1121/1.1906591. URL https://doi.org/10.1121/1.1906591.

[28] David Linton Johnson, Joel Koplik, and Roger Dashen. Theory of dynamic permeability and tortuosity in fluid-saturated porous media. *Journal of fluid mechanics*, 176:379–402, 1987.

[29] Michael Jones and Willie Watson. On the use of experimental methods to improve confidence in educed impedance. In *17th AIAA/CEAS Aeroacoustics Conference (32nd AIAA Aeroacoustics Conference)*, page 2865, 2011.

[30] Michael Jones, Maureen Tracy, Willie Watson, and Tony Parrott. Effects of liner geometry on acoustic impedance. In *8th AIAA/CEAS Aeroacoustics Conference & Exhibit*, page 2446, 2002.

[31] Michael Jones, Willie Watson, Tony Parrott, and Charles Smith. Design and evaluation of modifications to the nasa langley flow impedance tube. In *10th AIAA/CEAS Aeroacoustics Conference*, page 2837, 2004.

[32] Michael Jones, Willie Watson, Douglas Nark, Brian Howerton, and Martha Brown. A review of acoustic liner experimental characterization at nasa langley. April 2020. doi: 10.13140/RG.2.2.15613.10720.

[33] Michael G. Jones. Nasa langley activities on broadband fan noise reduction via novel liner technologies, presentation slides (ceas/x-noise workshop on broadband noise of rotors and airframe la rochelle, france). 2015.

[34] Michael G Jones and Tony L Parrott. Evaluation of a multi-point method for determining acoustic impedance. *Mechanical Systems and Signal Processing*, 3(1):15–35, 1989.

[35] Michael G Jones and Tony L Parrott. Evaluation of a multi-point method for determining acoustic impedance. *Mechanical Systems and Signal Processing*, 3(1):15–35, 1989.

[36] Michael G Jones and Patricia E Stiede. Comparison of methods for determining specific acoustic impedance. *The Journal of the Acoustical Society of America*, 101(5):2694–2704, 1997.

[37] Michael G Jones, Willie R Watson, Brian M Howerton, and Stefan Busse-Gerstengarbe. Comparative study of impedance eduction methods, part 2: Nasa tests and methodology. In *19th AIAA/CEAS Aeroacoustics Conference*, page 2125, 2013.

[38] RE Kraft, J Yu, and HW Kwan. Acoustic treatment design scaling methods. volume 2; advanced treatment impedance models for high frequency ranges. 1999.

[39] Heinrich Kuttruff. *Room acoustics*. Crc Press, 2016.

[40] Bert Lagrain, Laurens Boeckx, Edith Wilderjans, JA Delcour, and Walter Lauriks. Non-contact ultrasound characterization of bread crumb: application of the biot–allard model. *Food research international*, 39(10):1067–1075, 2006.

[41] J Lee and L Edmonds. Noise action plan contours for heathrow airport. *ERCD Report*, 1107, 2011.

[42] Tiara J Lu, Audrey Hess, and MF Ashby. Sound absorption in metallic foams. *Journal of applied physics*, 85(11):7528–7539, 1999.

[43] Pranav Manjunath, Francesco Avallone, Damiano Casalino, Daniele Ragni, and Mirjam Snellen. Characterization of liners using a lattice-boltzmann solver. In *2018 AIAA/CEAS Aeroacoustics Conference*, page 4192, 2018.

[44] Adrien Mann, Franck Perot, Min-Suk Kim, and Damiano Casalino. Characterization of acoustic liners absorption using a lattice-boltzmann method. In *19th AIAA/CEAS aeroacoustics conference*, page 2271, 2013.

[45] T.H. Melling. The acoustic impedance of perforates at medium and high sound pressure levels. *Journal of Sound and Vibration*, 29(1):1 – 65, 1973. ISSN 0022-460X. doi: https://doi.org/10.1016/S0022-460X(73)80125-7. URL http://www.sciencedirect.com/science/article/pii/S0022460X73801257.

[46] RE Motsinger and RE Kraft. Design and performance of duct acoustic treatment. 1991.

[47] MK Myers. On the acoustic boundary condition in the presence of flow. *Journal of Sound and Vibration*, 71(3):429–434, 1980.

[48] Simone Olivetti. *Direct Numerical Simulation of turbulent flows with an impedance boundary condition*. PhD thesis, University of Southampton, 2016.

[49] Tony Parrott and Michael Jones. Cascaded perforates as one-dimensional, bulk absorbers. In *12th AIAA/CEAS Aeroacoustics Conference (27th AIAA Aeroacoustics Conference)*, page 2402, 2006.

[50] Tony L Parrott, Willie R Watson, and Michael G Jones. Experimental validation of a two-dimensional shear-flow model for determining acoustic impedance. 1987.

[51] F Pérot, D Freed, and A Mann. Acoustic absorption of porous materials using lbm. 19 th aiaa. In *CEAS Aeroacoustics Conference, Berlin*, 2013.

[52] D Arumuga Perumal and Anoop K Dass. A review on the development of lattice boltzmann computation of macro fluid flows and heat transfer. *Alexandria Engineering Journal*, 54(4):955–971, 2015.

[53] Peter Preisendörfer, Lucie Herold, and Karin Kurz. Road traffic and aircraft noise as drivers of environmental protest. *KZfSS Kölner Zeitschrift für Soziologie und Sozialpsychologie*, 72(2):165–191, 2020.

[54] Ygaäl Renou and Yves Aurégan. Failure of the ingard–myers boundary condition for a lined duct: An experimental investigation. *The Journal of the Acoustical Society of America*, 130(1):52–60, 2011.

[55] Christoph Richter and Frank Thiele. Stability of time explicit impedance models. In *13th AIAA/CEAS Aeroacoustics Conference (28th AIAA Aeroacoustics Conference)*, page 3538, 2007.

[56] Christoph Richter, Frank H Thiele, Xiaodong D Li, and Mei Zhuang. Comparison of time-domain impedance boundary conditions for lined duct flows. *AIAA journal*, 45(6):1333–1345, 2007.

[57] Sjoerd Rienstra. Impedance models in time domain, including the extended helmholtz resonator model. In *12th AIAA/CEAS Aeroacoustics Conference (27th AIAA Aeroacoustics Conference)*, page 2686, 2006.

[58] Sjoerd Rienstra and Avraham Hirschberg. *An Introduction to Acoustics*. August 2008.

[59] SW Rienstra and DK Singh. A systematic impedance model for nonlinear extended helmholtz resonator liner. 5 2016.

[60] Alejandro Rubio Carpio, Francesco Avallone, Daniele Ragni, Mirjam Snellen, and Sybrand van der Zwaag. 3d-printed perforated trailing edges for broadband noise abatement. In *25th AIAA/CEAS Aeroacoustics Conference*, page 2458, 2019.

[61] Sutharsan Satcunanathan, Riccardo Zamponi, Matthias Meinke, Nicolas Van de Wyer, Christophe Schram, and Wolfgand Schrder. Validation of a model for acoustic absorption in porous media. In *INTER-NOISE and NOISE-CON Congress and Conference Proceedings*, volume 259, pages 4329–4344. Institute of Noise Control Engineering, 2019.

[62] D.K. Singh and S.W. Rienstra. Nonlinear asymptotic impedance model for a helmholtz resonator liner. *Journal of Sound and Vibration*, 333(15):3536–3549, 2014. ISSN 0022-460X. doi: 10.1016/j.jsv.2014.03.013.

[63] L. J. Sivian. Acoustic impedance of small orifices. *The Journal of the Acoustical Society of America*, 7(2):94–101, 1935. doi: 10.1121/1.1915795. URL https://doi.org/10.1121/1.1915795.

[64] Andre Spillere, Danillo Reis, and Julio Cordioli. A systematic review of semi-empirical acoustic liner models under grazing flow and high spl. September 2016.

[65] Chenghai Sun, Franck Pérot, Raoyang Zhang, Phoi-Tack Lew, Adrien Mann, Vinit Gupta, David M Freed, Ilya Staroselsky, and Hudong Chen. Lattice boltzmann formulation for flows with acoustic porous media. *Comptes Rendus Mécanique*, 343(10-11):533–544, 2015.

[66] Christopher KW Tam and Laurent Auriault. Time-domain impedance boundary conditions for computational aeroacoustics. *AIAA journal*, 34(5):917–923, 1996.

[67] Christopher KW Tam, Konstantin A Kurbatskii, KK Ahuja, and RJ Gaeta Jr. A numerical and experimental investigation of the dissipation mechanisms of resonant acoustic liners. *Journal of Sound and Vibration*, 245(3):545–557, 2001.

[68] Christopher M Teixeira. Incorporating turbulence models into the lattice-boltzmann method. *International Journal of Modern Physics C*, 9(08):1159–1175, 1998.

[69] BJ Tester. The propagation and attenuation of sound in lined ducts containing uniform or “plug” flow. *Journal of Sound and Vibration*, 28(2):151–203, 1973.

[70] Willie Watson and Michael Jones. Evaluation of wall boundary conditions for impedance eduction using a dual-source method. In *18th AIAA/CEAS Aeroacoustics Conference (33rd AIAA Aeroacoustics Conference)*, page 2199, 2012.

[71] Willie R Watson and Michael G Jones. Impedance eduction in a duct using linearized euler equations. In *2018 AIAA/CEAS Aeroacoustics Conference*, page 3442, 2018.

[72] Chenyang Weng, Anita Schulz, Dirk Ronneberger, Lars Enghardt, and Friedrich Bake. Flow and viscous effects on impedance eduction. *AIAA Journal*, 56(3):1118–1132, 2018.

[73] Qi Zhang and Daniel J Bodony. Numerical simulation of two-dimensional acoustic liners with high-speed grazing flow. *AIAA journal*, 49(2):365–382, 2011.

[74] Qi Zhang and Daniel J Bodony. Numerical investigation and modelling of acoustically excited flow through a circular orifice backed by a hexagonal cavity. *Journal of Fluid Mechanics*, 693:367–401, 2012.